THE RED DEAD REDEMPTION SURVEY OF CIRCUMGALACTIC GAS ABOUT MASSIVE GALAXIES. I. MASS AND METALLICITY OF THE COOL PHASE

Michelle A. Berg,[1] J. Christopher Howk,[1] Nicolas Lehner,[1] Christopher B. Wotta,[1] John M. O'Meara,[2,3]
David V. Bowen,[4] Joseph N. Burchett,[5] Molly S. Peeples,[6,7] and Nicolas Tejos[8]

[1]Department of Physics, University of Notre Dame, Notre Dame, IN 46556
[2]Department of Chemistry and Physics, Saint Michael's College, Colchester, VT, 05439
[3]W. M. Keck Observatory 65-1120 Mamalahoa Hwy. Kamuela, HI 96743
[4]Princeton University Observatory, Princeton, NJ 08544
[5]Department of Astronomy and Astrophysics, UCO/Lick Observatory, University of California, Santa Cruz, Santa Cruz, CA 95064
[6]Space Telescope Science Institute, Baltimore, MD, 21218
[7]Department of Physics and Astronomy, Johns Hopkins University, Baltimore, MD 21218
[8]Instituto de Física, Pontificia Universidad Católica de Valparaíso, Casilla 4059, Valparaíso, Chile

ABSTRACT

We present a search for H I in the circumgalactic medium (CGM) of 21 massive ($\langle \log M_\star \rangle \sim 11.4$), luminous red galaxies (LRGs) at $z \sim 0.5$. Using UV spectroscopy of QSO sightlines projected within 500 kpc ($\sim R_{\rm vir}$) of these galaxies, we detect H I absorption in 11/21 sightlines, including two partial Lyman limit systems and two Lyman limit systems. The covering factor of $\log N(\text{H I}) \geq 16.0$ gas within the virial radius of these LRGs is $f_c(\rho \leq R_{\rm vir}) = 0.27^{+0.11}_{-0.10}$, while for optically-thick gas ($\log N(\text{H I}) \geq 17.2$) it is $f_c(\rho \leq R_{\rm vir}) = 0.15^{+0.10}_{-0.07}$. Combining this sample of massive galaxies with previous galaxy-selected CGM studies, we find no strong dependence of the H I covering factor on galaxy mass, although star-forming galaxies show marginally higher covering factors. There is no evidence for a critical mass above which dense, cold ($T \sim 10^4$ K) gas is suppressed in the CGM of galaxies (spanning stellar masses $9.5 \lesssim \log M_\star \lesssim 11.8$). The metallicity distribution in LRGs is indistinguishable from those found about lower-mass star-forming galaxies, and we find low-metallicity gas with [X/H] ≈ -1.8 (1.5% solar) and below about massive galaxies. About half the cases show super-solar [Fe II/Mg II] abundances as seen previously in cool gas near massive galaxies. While the high-metallicity cold gas seen in LRGs could plausibly result from condensation from a corona, the low-metallicity gas is inconsistent with this interpretation.

Keywords: galaxies: abundances — galaxies: evolution — galaxies: halos — intergalactic medium — quasars: absorption lines

1. INTRODUCTION

Many galaxies have experienced some process(es) that "quenched" their ability to transform gas into stars. For more massive "red-and-dead" galaxies, this does not mean that they lack a supply of gas: massive and/or elliptical galaxies contain significant reservoirs of hot gas (e.g., Anderson et al. 2013; Singh et al. 2018) and even some cool gas in both their interstellar medium (Serra et al. 2012; O'Sullivan et al. 2018) and the surrounding circumgalactic medium (CGM, Thom et al. 2012), albeit at a lower mass fraction than typical star-forming galaxies. Indeed, as these galaxies continue to accrete mass from their surroundings, they will accrete new gas as well (e.g., Fakhouri et al. 2010; Oser et al. 2010; Hausam-

mann et al. 2019). Massive galaxies thus contain significant gas mass, but they are not able to efficiently access that gas to form new stars at a high rate. This is in large part due to the physical conditions of their gas: it is predominantly hot, with long cooling times.

Simulations and theoretical work have suggested that the transition to quiescence is perhaps associated with different modes for gas accretion with galaxy mass (see the general CGM review by Tumlinson, Peeples, & Werk 2017 and additional reviews on accretion in Fox & Davé 2017). Low-mass galaxies ($M_\star \lesssim 10^{10.5}$ M$_\odot$) may be able to accrete cold matter directly from the intergalactic medium (IGM, Cattaneo et al. 2006); if that gas can stay cool as it falls to the center of the halo, it may fuel star formation relatively directly (e.g., Birnboim & Dekel 2003; Kereš et al. 2005; Dekel & Birnboim 2006; Stewart et al. 2011). (In this context "cold" or "cool" is used to describe gas at $T < T_{\rm vir}$, although we will

Corresponding author: Michelle A. Berg
mberg3@nd.edu

typically use it to describe dense, photoionized gas of order $T \sim 10^4$ K.) However, cool material accreting onto higher-mass galaxies is thought to encounter strong accretion shocks, heating the gas to $\sim T_{\rm vir}$ (Dekel & Birnboim 2006; Ocvirk et al. 2008; Crain et al. 2010; Correa et al. 2018). Fueling star formation with matter accreted in this way requires the gas be able to cool again (likely through a cooling instability) and survive a fall into the central regions of a galaxy to form stars (Maller & Bullock 2004; McCourt et al. 2012; Voit et al. 2015). The prevailing picture is that this "hot-mode accretion" involving cooling from the hot CGM is relatively inefficient, especially when confronted by processes that suppress the cooling such as feedback from supermassive blackholes in these galaxies and ionization by the ultraviolet background (Oppenheimer & Schaye 2013; Nelson et al. 2015). It is this inefficiency that ultimately keeps the star formation rate in massive galaxies low.

Measuring the properties of cold gas in the CGM about massive galaxies offers a way to directly assess several of the assumptions inherent in this picture. Cold gas in massive halos has been traditionally expected to be relatively rare (i.e., low volume filling factors, low covering factors). Such gas could arise from expulsion or stripping of gas from satellites or from cooling instabilities in the hot CGM itself. Both scenarios would produce relatively metal-rich cold gas and be found preferentially in the inner CGM, where the gas is denser and metallicities are higher (the latter important for the cooling process). Generally, any pristine gas accreted onto massive halos should be shock-heated and unable to cool until it is mixed with more metal-rich material (Wiersma et al. 2009). Thus, we expect very little in the way of cold, metal-poor gas in the CGM of massive galaxies, in contrast to what is found more generally (e.g., Lehner et al. 2013, 2016; Wotta et al. 2016, 2019).

There are hints that this picture is not so simple (see Chen 2017 for a recent review of cold gas in the CGM of massive galaxies). For example, Thom et al. (2012) found no discernible difference between the cold H I content in the CGM of quiescent galaxies (log sSFR ≤ -11 [yr^{-1}] and $10^{10.5} \leq M_\star \leq 10^{11.5}$ M$_\odot$) and star-forming galaxies (log sSFR > -11 [yr^{-1}] and $10^{9.5} \leq M_\star \leq 10^{11.1}$ M$_\odot$) at $z \sim 0.2$ in the COS-Halos survey (for a recent update, see Prochaska et al. 2017, hereafter P17). Thus, it appears that the CGM of these quiescent, high-mass galaxies has a significant component of cold H I that is not being used to fuel star formation (Tumlinson et al. 2013). We still lack a thorough understanding of why these quiescent systems are not using this gas to form stars nor of what the origins of this gas are. Thus,

further study of the mass-dependence of the cold H I content of galaxies is warranted.

Several recent studies have probed the cold gas content of massive luminous red galaxies (LRGs) at $z \lesssim 1$ (e.g., Gauthier et al. 2009; Lundgren et al. 2009; Chen et al. 2010a; Bowen & Chelouche 2011; Zhu et al. 2014; Pérez-Ràfols et al. 2015; Huang et al. 2016; Chen et al. 2018; Smailagić et al. 2018; Zahedy et al. 2019). LRGs are high-mass ($M_\star \gtrsim 10^{11}$ M$_\odot$) quiescent galaxies with old stellar populations that have been selected via color (to select quiescent, high redshift galaxies) and magnitude (to select massive, $\gtrsim$3L* systems) cuts (Eisenstein et al. 2001). They have been passively evolving since $z \sim 1$ (Banerji et al. 2010). These characteristics make LRGs particularly interesting to study the physics of the baryon cycle because they extend the mass scale to >L* (the COS-Halos survey is $\sim$L*), and their passivity ensures we are characterizing the CGM around galaxies that are at the end of their star-forming life cycle. Given their importance for cosmological studies (e.g., Eisenstein et al. 2005; Xu et al. 2013; Slepian et al. 2017), there are large samples of LRGs with both SDSS photometry and spectroscopy (Dawson et al. 2013, 2016; Prakash et al. 2016; Albareti et al. 2017). Due to these SDSS surveys, the general characteristics of LRGs are well-understood. (Luminous blue galaxies and blue cluster galaxies would also be good objects to test accretion predictions, but there currently is not a large, uniformly-selected sample to draw from.)

Significant metal-line absorption from the CGM of LRGs has been found in several studies, hinting at a prevalence of metal-enriched cool gas. Bouché et al. (2004) found a high cross-correlation amplitude between Mg II absorbers seen against QSOs and LRGs, implying LRG halos house cold, metal-enriched gas. This result was confirmed by Gauthier et al. (2009) and Lundgren et al. (2009) with larger samples. Using stacked QSO absorption lines to study weaker Mg II absorption, Zhu et al. (2014) and Pérez-Ràfols et al. (2015) again found Mg II absorbers are correlated with LRGs out to 10 Mpc (a result confirmed recently by Lan & Mo 2018). Thus, there is a clear statistical correlation of metal-enriched cold gas with LRG halos.

Searches for individual strong Mg II absorbers associated with individual LRGs have yielded high covering factor estimates of cold, metal-enriched gas around LRGs using absorption lines toward background QSOs (Chen et al. 2010b; Bowen & Chelouche 2011; Gauthier & Chen 2011a; Huang et al. 2016). For example, Huang et al. (2016) found a covering factor (f_c) for impact parameters $\rho \leq 120$ kpc of $f_c(\rho \leq 120\,{\rm kpc}) > 0.15$, a value that falls to ~ 0.05 for $\rho \leq 500$ kpc. All of these surveys

indicate an abundance of cool, metal-enriched gas in the CGM of LRGs. However, they have limited diagnostic power. In order to obtain larger samples of galaxies with QSOs projected at small impact parameters, these works utilize low-resolution spectroscopy of Mg II, giving sensitivity only to the strongest absorbers (typically at the level of W_r(Mg II 2796) $\gtrsim 0.3$ Å). While the presence of strong Mg II tells us there is metal-enriched gas about LRGs, it gives us no information on whether metal-poor gas that may trace new accretion can survive deep in the halos of these massive galaxies.

In order to address these shortcomings, we study the H I content within $\rho \lesssim 500$ kpc ($\sim R_{\rm vir}$) of a sample of massive LRGs using archival ultraviolet (UV) spectroscopy from the *Hubble Space Telescope* (*HST*). The galaxies targeted by our Red Dead Redemption (RDR) survey all have masses in excess of the predicted critical masses marking the transition between galaxies thought to obtain their gas via "cold-mode" accretion and those acquiring their gas via "hot-mode" accretion (e.g., $M_h = 10^{12}$ M$_\odot$, Birnboim & Dekel 2003; Dekel & Birnboim 2006; Ocvirk et al. 2008; Nelson et al. 2018). Here we aim to test whether LRGs and other massive galaxies show a deficit of cold, dense H I compared with lower-mass, star-forming galaxies and to assess the frequency of gas that may represent recent accretion (assessed through its metallicity) in these halos. During the preparation of our survey, a complementary work by Chen et al. (2018, hereafter C18) became available. Their work focused on cool gas in the inner regions of a sample of massive galaxy halos (their sightlines probe $\rho \lesssim 160$ kpc while ours extend to the full impact parameter range within LRG halos $\rho \lesssim 500$ kpc). Their findings of a significant covering factor of optically-thick H I are in agreement with ours, and we combine the samples in later sections of this paper.

Our paper is organized as follows. We describe our selection of the RDR sample of LRGs with *HST* UV spectroscopy in § 2 and summarize our data reduction and spectral analysis in § 3. We consider the column density and covering factors of H I absorbers with impact parameters about the RDR LRGs in § 4. We measure the metallicity of the cool absorbers to constrain their origins in § 5. We explore the implications of our results in § 6. Our main results are summarized in § 7. A companion paper, Howk et al. (2019, hereafter Paper II) focuses on the highly-ionized phase of the CGM about the RDR LRGs as traced by O VI.

Throughout this paper we adopt the cosmology from Planck Collaboration et al. (2016), notably $H_0 = 67.7$ km s^{-1} Mpc^{-1}, $\Omega_m(z = 0) = 0.309$, and $\Omega_\Lambda(z = 0) = 0.691$. We adopt a naming scheme for objects as fol-

lows: target galaxies are labelled as "LRG" followed by their SDSS (J2000) coordinate designation; QSO targets are listed by their SDSS coordinate name. We will be studying absorption from partial Lyman limit systems (pLLSs) and Lyman limit systems (LLSs) in this work. We adopt definitions of pLLSs as absorbers with H I column densities $16.0 \leq \log N(\mathrm{H\,I}) < 17.2$; LLSs are defined by $17.2 \leq \log N(\mathrm{H\,I}) < 19.0$. We generally refer to absorption systems with $\log N(\mathrm{H\,I}) \geq 16.0$ as "strong H I absorbers."

2. SAMPLE SELECTION AND GALAXY PROPERTIES

2.1. *Sample Selection*

In this work we compile a sample of QSO-LRG pairs for which the QSOs have been observed in the UV by *HST*. We selected the LRGs from the SDSS DR13 (Albareti et al. 2017) LOWZ and CMASS samples of the BOSS and eBOSS surveys (Dawson et al. 2013, 2016, with additional information on the eBOSS target selection in Prakash et al. 2016). The LOWZ sample targets massive galaxies in the range $0.15 \lesssim z \lesssim 0.43$, whereas the CMASS sample focuses on $0.43 \lesssim z \lesssim 0.7$ (Dawson et al. 2013). The CMASS sample includes massive blue galaxies, while the LOWZ sample does not. Hereafter, we refer to the galaxies as "LRGs," even if the CMASS sample is broader than the traditional LRG definition of Eisenstein et al. (2001). This includes the late-type galaxies that may make up $\sim 25\%$ of the sample (Masters et al. 2011) and may also be in our final RDR sample. The most important characteristic of these SDSS samples is that they select high-mass galaxies, with a mean stellar mass of $\log M_\star \approx 11.3 \pm 0.5$ (e.g., Maraston et al. 2013).[1]

The LRGs from which we draw our sample all have spectroscopic redshifts available. We further restrict our LRG selection to the redshift range $0.26 \leq z_{\rm LRG} \leq 1.25$. The minimum redshift is adopted to place the Lyman break in the UV spectral range accessible to *HST*; the Lyman break is usually key to accurately assessing the total H I column density, $N(\mathrm{H\,I})$, in high column density systems that are not damped. The maximum redshift is chosen so that a UV selection of QSOs can be made based on GALEX FUV magnitudes (see below). The typical redshift errors from the SDSS pipeline in this sample are $\sigma(z_{\rm LRG})/(1 + z_{\rm LRG}) \approx 10^{-4}$, which corresponds to ~ 30 km s^{-1}.

---

[1] Unless otherwise stated, all masses in this work are given in physical solar masses, M$_\odot$, with all cosmological corrections included. We adopt $h \equiv H_0/(100\,\mathrm{km\,s^{-1}\,Mpc^{-1}}) = 0.677$ throughout.

We drew QSOs from the DR7 QSO catalog of SDSS (Schneider et al. 2010) cross-matched with GALEX UV sources (Martin et al. 2005). We selected QSOs projected within 500 kpc of the LRGs, requiring $0.3 \leq z_{em} \leq 1.5$ and $0.1 \leq z_{em} - z_{LRG} \leq 0.5$. The low-redshift cut-off simply ensures the QSOs are at redshifts higher than our target LRGs. The high-redshift cut is made in order to avoid the confusing influence of the dense Lyman-α forest at higher redshifts. The redshift separation constraint minimizes the contamination from unrelated absorption that might contaminate the signature of the LRGs' CGM. We also apply a constraint to the GALEX photometry of the QSOs, $FUV \leq 21.0$ in order to ensure the objects are bright enough to produce good S/N in even the low-resolution observations (typical S/N for our observations are 8 for COS/G130M,G160M, 5 for COS/G140L, and 14 for FOS/G190H).[2] These constraints yield ~500 QSO-LRG pairs projected within $\rho \leq 500$ kpc.

We used this sample as the basis of a search of the Mikulski Archive for Space Telescopes (MAST) for *HST* UV spectra of the background QSOs, searching for data from the Goddard High Resolution Spectrograph, the Faint Object Spectrograph, the Space Telescope Imaging Spectrograph, and the Cosmic Origins Spectrograph. Because we are interested in an unbiased search for H I (in particular) associated with LRGs, we excluded any data from program 14171 (PI: Zhu) that targeted (some) LRGs on the basis of previously-identified Mg II absorption. This search yielded 24 sight lines with UV spectral coverage of the Lyman series lines at the redshift of the LRGs. Three of these LRGs were later removed from our sample. In one case, the QSO was initially targeted on the basis of a strong foreground absorber that resides at the redshift of the LRG. In the second, the galaxy was an outlier in stellar mass from the rest of the sample (with $\log M_\star < 11$), and the data for the third sightline were low enough resolution that we could not definitively determine if the absorption feature is associated with the LRG.

The remaining 21 QSO-LRG pairs listed in Table 1 form the basis of our study. The 21 LRGs along these sightlines lie in the range $0.28 \leq z_{LRG} \leq 0.61$. The median sample redshift is $z_{LRG} = 0.46$. To the best of our knowledge, based on a reading of the publicly-available program abstracts in MAST, none of the background QSOs were targeted due to the presence of the foreground LRGs in our sample. (Several of the QSOs were targeted to study other foreground galaxies, but

this does not affect our results.) Even with this selection, three sightlines do not have coverage of the Lyman break due to the choice of grating. These LRGs are all probed by Lyman series lines that give us the ability to place strong constraints on the absorption, so we have included them in our sample.

Compared to C18, our LRG selection is more restrictive. They have used all of SDSS to search for their spectroscopically confirmed LRGs, while we have stayed within the CMASS and LOWZ samples. Their sample has comparable redshift and stellar mass distributions to ours (see § 2.2), but our LRGs have a higher median color $(u - g) = 2.03$ and $(g - i) = 1.20$. We note the u-band magnitudes have large uncertainties.

2.2. *Galaxy Properties*

Table 2 summarizes the properties of the LRGs in the RDR sample. While there are galaxies in our final sample potentially hosting star formation (~20% show detectable [O II] emission), the defining characteristics of the galaxies are their redshift range and large masses. The redshifts in Table 2 are adopted from the SDSS pipeline for each LRG. The median redshift of our sample is $z_{LRG} = 0.46$, while the median impact parameter is $\rho = 261$ kpc. The distributions of redshifts and several other properties of our sample (described below) are shown in Figures 1 and 2.

For each target galaxy we estimate absolute r-band magnitudes and stellar masses using the kcorrect code (v4_3)[3] of Blanton & Roweis (2007). These SED fits make use of spectral templates from Bruzual & Charlot (2003) and assume the initial mass function of Chabrier (2003). We used Galactic extinction-corrected (Schlegel et al. 1998) MODEL magnitudes with the pipeline redshifts as inputs to kcorrect to assess the k-corrections and mass-to-light ratios of the galaxies. The results are given in Table 2. The output masses from the code are given in $M_\odot h^{-1}$, which we convert to masses with units $M_\odot$ in Table 2 and all that follows. These masses likely have an uncertainty of at least ± 0.3 dex, if not somewhat larger (Conroy 2013). Although we have not specifically fit the full spectra for all of these galaxies, the redshifts are fixed and the galaxy templates are well determined for these systems. We show the distribution of stellar masses for our sample in Figure 1 (bottom right panel). The galaxies in our sample have a median stellar mass $\log M_\star = 11.4$ (in $M_\odot$) with a standard deviation of 0.2 dex, both consistent with the sample studied by Huang et al. (2016).

---

[2] These S/N values are per pixel and describe the spectrum as a whole (Stoehr et al. 2008).

[3] Available through http://kcorrect.org or http://github.com/blanton144/kcorrect.

We estimate the halo mass, M_h, of each LRG using the stellar mass–halo mass (SMHM) relationship of Rodríguez-Puebla et al. (2017), who combine a large number of observational studies of the SMHM scalings. In particular, they provide a prescription (their Equation 66) for assessing the mean halo mass at a given stellar mass, $\langle \log M_h(M_\star) \rangle$ (which is different than the inverse of the stellar mass-to-halo mass ratios given the asymmetries in the scatter about the mean relationship; Behroozi et al. 2010). Recently Tinker et al. (2017) have assessed the SMHM relationship in a sample of CMASS galaxies drawn in much the same way as our sample, focusing on $\log M_\star \gtrsim 11.4$, though they extend their fits to somewhat lower masses. Their predictions for $\langle \log M_h(M_\star) \rangle$ yield halo masses lower by roughly 0.3 dex (i.e., a factor of ~ 2) at a given stellar mass than those of Rodríguez-Puebla et al. (2017). There are a number of other recent studies on the SMHM relation at high stellar masses (e.g., Velander et al. 2014; Shan et al. 2017). We adopt the Rodríguez-Puebla et al. (2017) results both because they account for the asymmetric scatter in the $M_\star - M_h$ relationship in order to properly calculate $\langle \log M_h(M_\star) \rangle$ and because their analysis allows us to calculate the masses of the RDR LRGs and lower-mass galaxies against which we will compare the LRGs with a consistent treatment. Our final halo mass estimates are given in Table 2; the median halo mass derived for our sample is $\log M_h = 13.4$ (in $M_\odot$).

For comparison with other galaxy absorber studies, it can be useful to consider the impact parameters relative to the virial radii of each galaxy. We define the "virial radius" as $R_{vir} = R_{200}$, the radius enclosing the halo mass for a mean density $200\times$ that of the critical density at the redshift of each LRG. That is, $R_{vir} = R_{200} \equiv (3M_h/4\pi \Delta \rho_c)^{1/3}$, where $\Delta = 200$ and ρ_c is the critical density. We refer to this scale simply as R_{vir} throughout this paper. Our estimates of R_{vir} are given in Table 2. Given the $M_h^{1/3}$ dependence of these values, they are not strongly affected by our choice of SMHM relation. Our calculations give a median virial radius $R_{vir} = 516$ kpc; the median normalized impact parameter of our sightlines is $\rho/R_{vir} = 0.44$.

To limit the star formation rates (SFRs) of the RDR sample, we use [O II] 3727+3729 emission as an indicator of star formation in these galaxies. These results should be considered upper limits given the potential for non-star formation contributions to these lines (Huang et al. 2016). We adopt the calibration of the [O II]-SFR relationship from Moustakas et al. (2006) for the highest-luminosity galaxies (which are appropriate given the range in absolute magnitudes of our sample; see Table 2). Thus we assume $\log \mathrm{SFR} \, (\mathrm{M_\odot \, yr^{-1}}) = -40.24 +$ $\log L_{[\mathrm{O\,II}]}$ (ergs s^{-1}). We adopt the SDSS pipeline fits to [O II] emission from the LRGs, correcting for Milky Way foreground extinction assuming Schlegel et al. (1998) extinction with $R_V = 3.1$ and an extinction curve following Cardelli et al. (1989). We do not correct for internal extinction, as neither do Moustakas et al. (2006) in their calibration, which partly causes the luminosity dependence in their [O II]-SFR relationship. Where galaxies do not have detectable [O II] emission, we adopt the 2σ upper limits on the flux.

In two cases the SDSS fits gave uncertainties well above ($\gtrsim 10\times$ higher) those typical of the sample. In one case, it was not clear why the fits yielded such high uncertainties; in the other, the [O II] doublet was coincident with a poorly-subtracted sky emission line. In these two cases, we used the pPXF spectral fitting code of Cappellari (2017) to refit the SDSS spectra. Our fit for LRG SDSSJ125859.98+413128.3 yielded tighter limits on the [O II] emission. For LRG SDSSJ075217.92+273835.6, where the [O II] line is contaminated, we had good measurements for the fluxes of Hβ and Hα. The limit on Hβ is stronger (as Hα is in the forest of sky lines in the far red). For only this galaxy we use the Hβ line as an indicator of the galaxy's SFR, adopting the Hβ-SFR calibration of $\log \mathrm{SFR} \, (\mathrm{M_\odot \, yr^{-1}}) = -40.11 + \log L_{\mathrm{H}\beta}$ (ergs s^{-1}) from Moustakas et al. (2006).

The specific star formation rates, $\mathrm{sSFR} \equiv \mathrm{SFR}/M_\star$, for the RDR galaxies are given in Table 2. Because the SDSS fibers used to limit the SFR do not encompass all of the stellar light from the galaxy, we compare our derived star formation rates to the stellar masses contained within the fiber. We use the ratio of the SDSS FIBER2FLUX to the MODELFLUX in the r-band to scale down our derived stellar masses for this comparison. In most cases, non-detections of [O II] do not set stringent constraints on the sSFR. In Figure 1 we show the sSFRs calculated using the SFR derived from a luminosity-weighted median stack of the LRG spectra showing no detectable [O II] emission, $\mathrm{SFR} = 0.49 \pm 0.23 \, \mathrm{M_\odot \, yr^{-1}}$. Thus even the stacked spectrum of these galaxies gives only a marginal detection of [O II] emission.

Even amongst the galaxies with detectable [O II] emission, it is not necessarily connected to star formation. The [O II] and [O III] emission of LRGs generally resembles that of low-ionization nuclear emission-line region (LINER)-like galaxies (Huang et al. 2016), where the emission is suspected to come from either activity from active galactic nuclei (AGN) or ionization from post-asymptotic giant branch stars (e.g., Ho 2008; Yan & Blanton 2012). Belfiore et al. (2016) have shown more generally that LINER emission does not necessarily originate from the nucleus, but from spatially extended re-

gions in both star-forming and passive galaxies. Furthermore, stacking of FIRST radio images suggests nearly all LRGs house an AGN (Hodge et al. 2008, 2009). In light of these considerations, all sSFRs should be considered upper limits.

For the most part we do not have extensive data on the environments of these specific galaxies. We expect all will be surrounded by an extensive suite of lower-mass satellites. At lower redshift ($0.16 < z < 0.33$), $\sim70\%$ of LRGs are central galaxies in clusters with richness parameter $\lambda > 20$ in the redMaPPer cluster catalog (Rykoff et al. 2014, 2016; Hoshino et al. 2015). We cross-matched our RDR sample of galaxies with the redMaPPer cluster catalog version 6.3[4] and found five matches. The LRGs SDSSJ124307.36+353926.3, SDSSJ141307.39+091956.7, SDSSJ171651.46+302649.0, SDSSJ075217.92+273835.6, and SDSSJ132457.98+271742.6 are all within < 0.2" of the cluster center, indicating that they are either the central galaxy or the brightest cluster galaxy. LRGs SDSSJ124307.36+353926.3, SDSSJ141307.39+091956.7, and SDSSJ075217.92+273835.6 are found in rich clusters ($\lambda > 20$), while the other two are found in clusters with a smaller number of member galaxies ($\lambda \sim 10$). The fact that the other galaxies are not specifically identified with overdensities like those in the redMaPPer catalog does not mean they lack satellites. A detailed search and characterization of the LRG environment is beyond the scope of this paper. However, Chen et al. (2019) characterized the environment around one of the C18 LRGs. Using integral field spectroscopy, they determined the LRG is located within a group of galaxies with a range of $10^7 \leq M_\star \leq 10^{11}$ $M_\odot$. We expect this is the typical environment for our sample as well.

It has also been shown that brightest cluster galaxies have extended stellar halos (Huang et al. 2018). If the RDR LRGs exhibit such extended stellar halos, our derived stellar masses – as well as halo masses and virial radii – will be underestimated due to light being missed by the apertures. This does not effect our goal to observe the CGM about high-mass galaxies, but it affects the context of our sightlines, as we discuss their normalized impact parameter, $\rho/R_{\rm vir}$, throughout this paper. Huang et al. (2018) determined the stellar mass could be underestimated by at most 0.2 dex when using the SDSS `CMODEL` magnitudes to fit galaxy SEDs. In our analysis we utilized the `MODEL` magnitudes, and the stellar mass estimates we derived using `kcorrect` carry a ±0.3 dex uncertainty. The error in the mass estimate

due to missed stellar light in the aperture is within the uncertainty of our mass estimates. If our virial radii are underestimated, the pLLSs/LLSs we detect would be located at even lower normalized impact parameters. These issues neither change fundamentally our results nor our discussion of the origin and fate of the gas we detect.

3. OBSERVATIONS AND DATA ANALYSIS

Our RDR sample comprises 21 QSOs with *HST* UV spectroscopy that pierce the CGM of 21 LRGs within $\rho \lesssim 500$ kpc. The use of UV spectroscopy allows us to identify the prevalence of H I and associated metal ions in the CGM of these galaxies. We supplement these UV data with optical spectroscopy to measure Mg II associated with the LRGs. Below we describe the datasets we have used and our approach to measuring absorption from the LRG CGM.
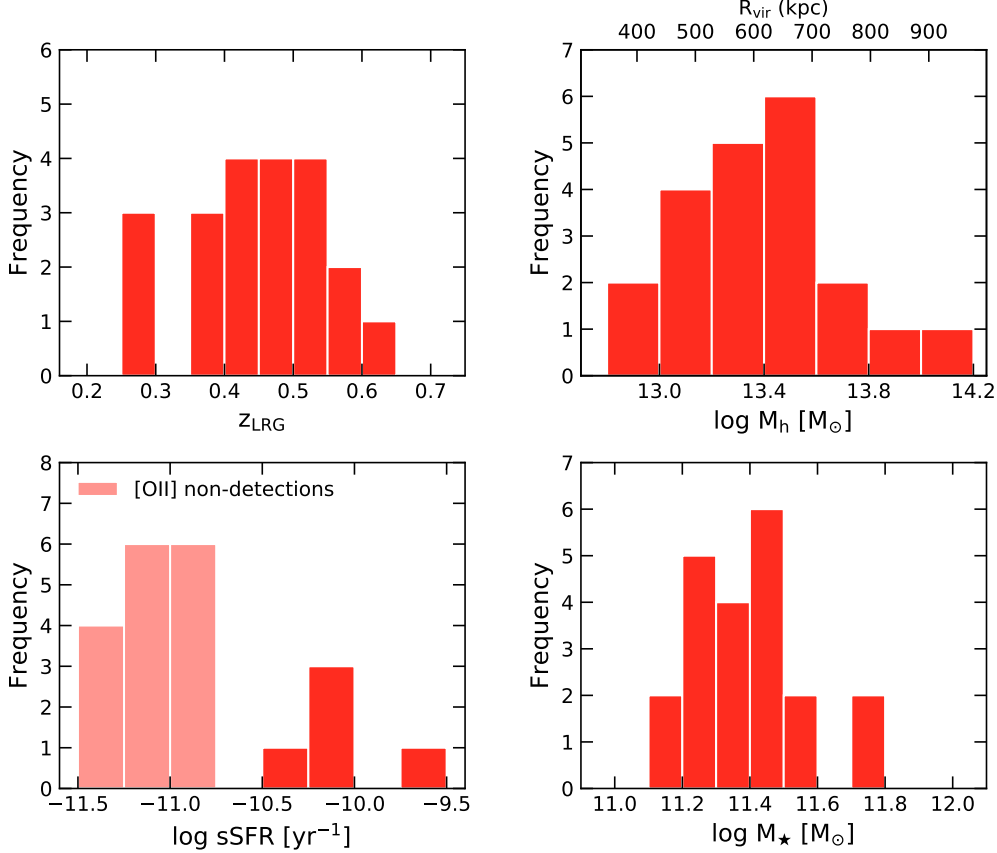
3.1. *Ultraviolet Spectroscopy from HST*

A summary of the QSO observations is provided in Table 3. Seventeen of the QSOs were observed with the medium resolution mode ($R \sim 18,000$) of COS using the G130M and/or G160M gratings. The other five observations were obtained with low resolution ($R \simeq 1,300 - 2,000$) UV spectra from COS and FOS. All of the COS spectra were retrieved from the *HST* Spectroscopic Legacy Archive (HSLA, Peeples et al. 2017) except for SDSSJ112756.76+115427.1, SDSSJ124307.57+353907.1, and SDSSJ150527.60+294718.3, which were not available in the April 2017 data release. For these spectra, we use the routines in COS Tools (Danforth et al. 2010, 2016) to coadd the data. Differences exist between the two data reduction processes, but they do not impact our column density measurements (Lehner et al. 2018). For the objects observed with FOS, we use the reduced spectra from Ribaudo et al. (2011).[5] One object, SDSSJ125224.99+291321.1, was observed with both COS and FOS, with a gap of ~140 Å between the two spectral regions. The spectrum and analysis of SDSSJ171654.20+302701.4 is described in Wotta et al. (2016). We make use of their data and column densities for this sightline.

3.2. *Supporting Ground-based Observations*

Previous surveys have used Mg II to understand the presence of metal-enriched gas in LRG halos (e.g., Bowen & Chelouche 2011; Zhu et al. 2014; Huang et al. 2016). We also measure Mg II for several of

---

[4] Available through http://risa.stanford.edu/redmapper/.

[5] Available through Vizier.

Figure 1. Distributions of z_{LRG}, $\log M_h$, $\log$ sSFR, and $\log M_\star$ for the RDR sample of LRGs. The redshifts come from the eBOSS and BOSS SDSS spectroscopic surveys. We primarily use [O II] to calculate the SFR, `kcorrect` to derive $M_\star$ (Blanton & Roweis 2007), and the SMHM relation from Rodríguez-Puebla et al. (2017) to calculate M_h. For [O II] non-detections, we adopt the SFR from the median stack of the LRG spectra showing no detectable [O II] emission in calculating the sSFRs. The sSFRs should be considered upper limits (see discussion in the text).
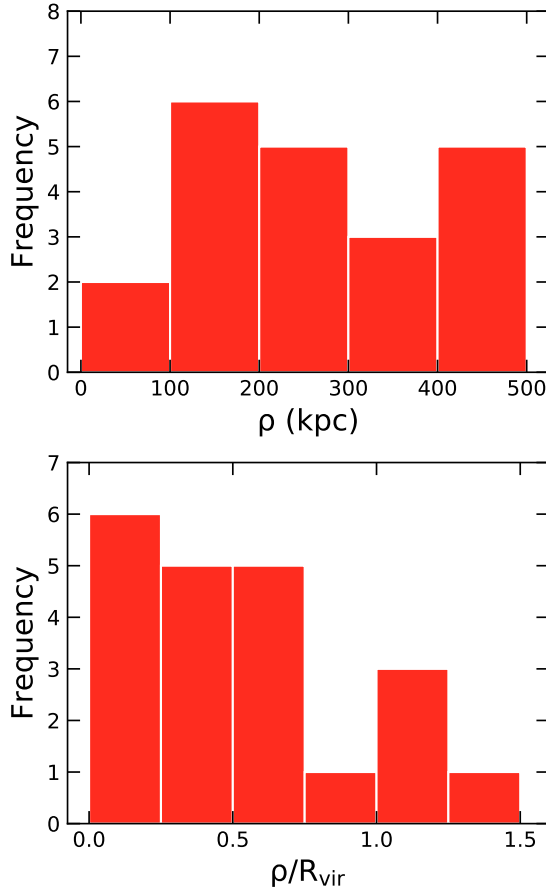
our sightlines through LRG halos because Mg II often provides the best metallicity constraints for pLLSs and LLSs (Wotta et al. 2016, 2019). High resolution spectroscopy yields the best constraints on the column density; two QSOs have spectroscopy from the High Resolution Echelle Spectrometer (HIRES) on Keck I in the Keck Observatory Archive. The spectra are reduced following Lehner et al. (2016), and one of these sightlines is reported in Wotta et al. (2016). We also analyze the SDSS spectra of the QSOs when available (four sightlines do not have Mg II coverage, Abolfathi et al. 2018). Due to the limited sensitivity and resolution of SDSS (and the low H I column densities along most of the sightlines), these columns are almost all upper limits.

3.3. *Absorption Line Search Methodology*

To find absorbing gas associated with the RDR LRGs, we conduct a search for hydrogen and metal-ion absorption in the QSO spectrum at the redshift of the LRG using a search window of ± 1000 km s^{-1}. Our choice of this large velocity search window follows from the es-

cape velocity of the median LRG halo from our survey ($\sim$930 km s^{-1} assuming a Navarro-Frank-White potential, Navarro et al. 1996, 1997). In the absence of an AGN, winds from a galaxy with $M_h \geq 10^{13}$ M$_\odot$ will not be able to escape the potential well (Sharma & Nath 2013). We also consider the Mg II survey in the CGM of LRGs by Huang et al. (2016, see their Figure 4). They found only 12% of their absorbers lie at a velocity offset greater than ± 500 km s^{-1} when considering impact parameters < 500 kpc. However, they also found a few systems at ± 1000 km s^{-1}, so we adopt the same window to ensure we consider all the gas that could be associated with each LRG.

When H I absorption is detected within ± 1000 km s^{-1} of the redshift of the LRG, we set the redshift of the absorbing gas using the Lyman series transitions. If a break in the QSO spectrum is observed, the redshift of the pLLS/LLS is determined from the centroids of the higher Lyman series lines. If a break is not present (due to spectral coverage or lower H I column), we use Lyα or Lyβ. In cases where no absorption is detected, we

Figure 2. Distributions of impact parameter, ρ (top), and normalized impact parameters, $\rho/R_{\rm vir}$ (bottom), for the QSO-LRG pairs in the RDR sample.

use the redshift of the LRG to set the center of the velocity integration window to estimate upper limits on the column densities.

3.4. *Column Density Measurements*

Our measurements of H I and ion column densities are made with different techniques or assumptions depending on the column density of the system and the quality of the data. Due to the heterogeneous mix of resolution and signal-to-noise (S/N), our limits on H I or metal absorption are not uniform across the sample. However, our focus in this work is on understanding the amount of high H I column density gas present about LRGs. For this purpose, the mixture of data properties is not an issue because the Lyman break is covered in almost every sightline. Two of the three sightlines that do not have Lyman break coverage do not exhibit high H I column absorbers; the final sightline can only be given a lower limit for the H I column density.

Four of the LRGs show strong H I systems ($\log N(\text{H I}) \geq 16.0$). Of these four systems, three have observable

breaks in the QSO spectrum at the Lyman limit. The H I column density can be determined from the break using $N(\text{H I}) = \tau_{LL}/\sigma_{LL}$, where τ_{LL} is the optical depth at the Lyman limit, and σ_{LL} is the absorption cross section of the hydrogen atom at the Lyman limit (Spitzer 1978). A composite QSO model is scaled to fit the continuum of the spectrum (Telfer et al. 2002)[6]; a break is then added to match the level of the absorbed continuum giving a measure of the optical depth and hence $N(\text{H I})$. To estimate the errors on $N(\text{H I})$ we follow the methodology described in Wotta et al. (2016). In short, the errors are estimated by offsetting the model to a point in which the model and data are inconsistent. This column density value is taken to be the 2σ value. We have included an example error fit to illustrate this inconsistency in Appendix A.

We determine the H I column density for the absorbers associated with LRGs SDSSJ111132.33+554712.8 and SDSSJ171651.46+302649.0 (reported in Wotta et al. 2016) from the optical depth at the break, but we can only estimate a lower limit for the absorber associated with LRG SDSSJ111508.24+023752.7 from this method due to the low level of flux recovery blueward of the Lyman limit. Lehner et al. (2018) modeled the H I profiles of this absorber with a Voigt profile fit using two components. However, revisiting this fit using the information from the velocity profiles of the metal lines (and in particular newly acquired Keck/HIRES spectra of Mg II and Fe II), it is apparent that at least three components are needed at -113, -19 (strongest component), and $+28$ km s^{-1}, the latter being the additional component observed in the metal lines. With now a lack of information on both the positive and negative wings of Lyβ in the strongest component at -19 km s^{-1}, there is a degeneracy in the solutions owing to poorly constrained individual b and N values. Thus, the strongest component cannot be constrained to better than $\log N(\text{H I}) = [18.00, 19.60]$. The lowest value is from the break at the Lyman limit. The highest value is from a Voigt profile fit with three components to the H I Lyman series using an updated version of the profile fitting code from Fitzpatrick & Spitzer (1997) and

---

[6] While the Telfer et al. (2002) model does not match all the specific features in a given QSO spectrum, the features in the EUV (the regime in which we are most interested) are not very prominent. This means the selection of the template does not have a large influence in the resultant fit. We also mitigate the differences in spectral index between templates by allowing our model to have a tip/tilt that accounts for these variances and possible calibration/dust effects.

the tabulated model of the line-spread COS function.[7] Any value above $\log N(\text{H I}) \simeq 19.6$ would produce too strong damping wings in Lyβ and too strong absorption in other weaker transitions. Though the allowed range of $\log N(\text{H I})$ overlaps with the canonical super-LLSs regime (SLLSs, $19.0 \leq \log N(\text{H I}) < 20.3$), we will refer to this absorber as an LLS throughout the rest of the paper for simplicity.

No strong break in the QSO spectrum is observed for the other high H I column density system. The pLLS associated with LRG SDSSJ141540.01+163336.4 is on the low end of the pLLS column density range, exhibiting a small partial break in the QSO spectrum. We measure the H I column density from the higher Lyman series lines using the apparent optical depth method (AODM, Savage & Sembach 1991). The AODM converts an absorption line to apparent column density per unit velocity interval. The total apparent column density is then determined by direct integration of the apparent column density per unit velocity interval: $N_a = \int_{v_1}^{v_2} N_a(v)dv$. The column density N is assumed to be N_a as long as there is no evidence of saturation (see below for our treatment of saturation). We also measure $N(\text{H I})$ from the break in the QSO spectrum at the Lyman limit for this absorber and find the column densities from the two methods are consistent. The $N(\text{H I})$ value measured from the break exhibits larger errors, so we adopt the value measured from the Lyman series lines.

An absorber is detected in the spectrum of QSO SDSSJ125224.99+291321.1, which has been observed with COS and FOS. Unfortunately, these data do not cover the Lyman limit and higher Lyman series lines associated with this absorber. With only Lyα and Lyβ, a curve-of-growth analysis did not provide any robust results. Using the AODM on Lyβ observed with FOS, we could place only a lower limit on $N(\text{H I})$ ($\log N(\text{H I}) > 15.2$).

For the remaining absorbers, the absorption is much weaker, and we use only the AODM to estimate the column densities or limits on the column densities of the H I and metal lines. The metal ion absorption line integration limits are set by the width of the associated hydrogen lines unless the metal ion profile is broader, contaminated, or shifted. If a line is contaminated, we shorten the integration limits. When no absorption is detected (for hydrogen or metals) we measure 2σ upper limits using the AODM by integrating over the section of the spectrum where the line would be located. As stated above, the redshift of the LRG is used as the center of

our integration window in these cases, and the velocity integration limits are set by the smallest line width (Δv) that can still be detected in the respective grating. For the low-resolution observations, this equates to nine pixels for FOS/G190H and 12 pixels for COS/G140L.

To check for saturation in lines that do not reach zero flux but have significant peak optical depth, we employ two procedures. If the transition is part of a doublet, we compare the column density values of the stronger line to the weaker line. When the weaker line has a higher column density, the Savage & Sembach (1991) saturation correction is applied. For other transitions where there are no other lines in the same ionization state of a species to use for comparison, other species in the same state are considered (e.g., C III and Si III). If one of these lines is saturated, we also mark the other transitions as saturated if the peak optical depth is similar or larger. For COS/G130M,G160M observations, transitions that reach a normalized residual flux of 0.25 and lower are definitely saturated. We assume transitions in the COS/G140L and FOS/G190H observations are saturated unless there are other transitions that can be used to check this assumption.

We include in Appendix A plots of the H I and ionic absorption profiles for each sightline to show the velocity range over which the transitions are integrated. Table A1 details the apparent column densities measured for each sightline. If an absorber shows more than one component in the profiles, we determine the column densities for each component, in an effort to compare the component metallicities. Since we will show there is no significant difference between the component metallicities in these cases (see Appendix C), we quote total column densities throughout the paper. The three spectra in which we observe a break at the Lyman limit of the pLLS/LLS are also provided in Appendix A.

4. CHARACTERISTICS OF STRONG H I ABSORPTION IN THE CGM ABOUT LRGS

4.1. *Hydrogen and Metal-Line Absorption*

Out of 21 sightlines, we find 11 detections of absorbing gas within $\pm 1000\,\text{km}\,\text{s}^{-1}$ of the LRG central redshift. The hydrogen column densities of the detected absorption lines span a broad range from $\log N(\text{H I}) < 13.0$ to > 18.0, but the distribution is not continuous. The absorber properties are summarized in Figures 3 and 4. We show in Figure 3 the H I column density as a function of impact parameter for the RDR sample. We find four strong H I absorbers (two pLLSs and two LLSs) in our sample with $\log N(\text{H I}) \geq 16.0$; four of the other seven H I detections are mostly at $\log N(\text{H I}) \leq 14.0$ (likely Lyα forest interlopers; see below). It seems the

LRGs exhibit either high H I column density gas or not much at all. Most of the strong absorbers lie at small impact parameters, $\rho \lesssim 0.5\,R_{\rm vir}$, consistent with results for other samples of galaxies (e.g., Tumlinson et al. 2013; Heckman et al. 2017; Keeney et al. 2017; P17).

The low H I column density absorbers in Figure 3 are likely dominated by Lyα forest contamination. As shown in Figure 4, a higher proportion of the weak absorbers exhibit large velocity offsets from the redshift of the LRGs ($|\Delta v| = |v_{\rm Ly\alpha} - v_{\rm LRG}|$) compared with the strong absorbers. The expected velocity dispersion for virialized gas in the halos of LRGs is $\sigma \approx 260$ km s^{-1} (Zahedy et al. 2019), suggesting the low H I column density absorbers found at high velocity offsets are not directly associated with the LRGs. We estimate the expected number of Lyα forest interlopers in our sample, $\mathcal{N}$, by integrating the differential column density distribution, $f(N, z)$, for each sightline i that has sensitivity to $\log N({\rm H\,I}) \leq 14.5$ absorption (this includes sightlines with non-detections). We use the fit to $f(N, z)$ from Lehner et al. (2007, their equation 6), extrapolating below their sensitivity limit of $\log N({\rm H\,I}) \sim 13.2$ and using the corrected parameter values from their erratum for the column density range $\log N({\rm H\,I}) = [13.2, 14.4]$ with $b \leq 40$ km s^{-1}. We perform the integration for each sightline from $N({\rm H\,I})_{\rm min}$ to $N({\rm H\,I})_{\rm max} = 10^{14.5}$ cm^{-2}, where $N({\rm H\,I})_{\rm min}$ is the sensitivity to H I column for each spectrum. Once $\mathcal{N}_i$ has been calculated for each sightline, we total the values to determine $\mathcal{N}$ for our survey. We expect $\mathcal{N} \sim 5$ Lyα forest interlopers in the RDR survey, equal to the number of $\log N({\rm H\,I}) \leq 14.5$ systems we detect (Figures 3 and 4 show only four as SDSSJ125901.67+413055.8 exhibits two systems that we sum for display in the figures; see Appendix A). Thus, it is very likely that all of the low H I column density systems are Lyα forest interlopers unrelated to the RDR galaxies themselves. Following a similar procedure, we expect to find zero random interlopers for $\log N({\rm H\,I}) > 14.5$ assuming the parameterization from Shull et al. (2017). Thus, the high column density systems are likely associated with the LRGs.
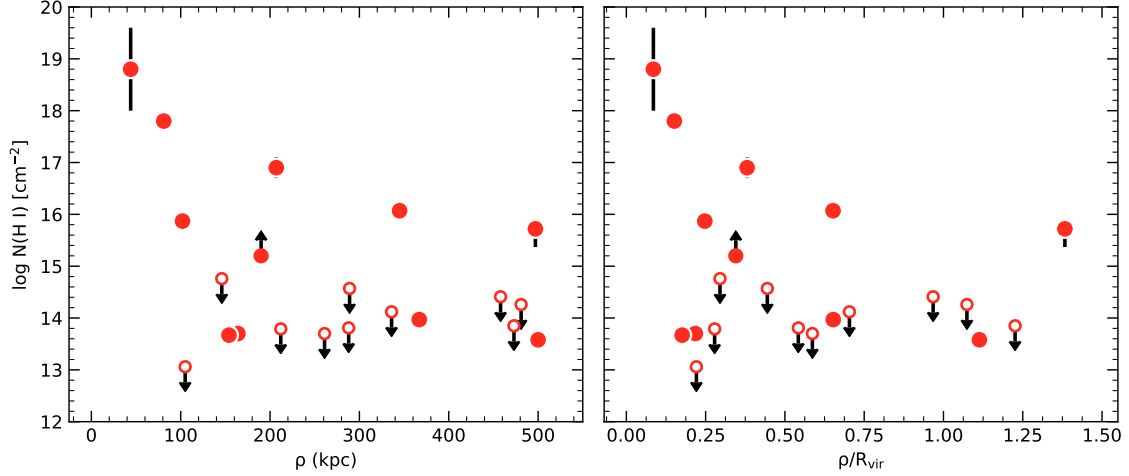
For the absorbers with $\log N({\rm H\,I}) > 14.5$, the mean velocity offset from the LRG is -70 km s^{-1}. The C18 LRG sample exhibits a mean of $+17$ km s^{-1} and a dispersion of 147 km s^{-1} (kinematics for this sample are discussed in Zahedy et al. 2019). Our low number of absorbers prevents us from fitting the velocity distribution to determine the dispersion and how it compares to the expected value for virialized motion in the LRG halo. The integration range (i.e., the full width at zero absorption) of the metal ions we observe are ~ 200 km s^{-1} in the COS/G130M,G160M gratings, with larger spans

seen in the lower resolution observations. These small velocity spans indicate the gas is cool and there is an absence of winds. In no cases do we (or C18) find metal-line absorption having the strength or velocity breadth of those seen around the two LRGs studied by Smailagić et al. (2018). It is unclear why they have detected such velocity spans (>750 km s^{-1}) at $\rho = 29$ kpc and 343 kpc. While we do not have a sightline at such a low impact parameter, we do have several sightlines at large impact parameters. So far, these two sightlines are the only instances with absorbers this large in the CGM of LRGs. A larger sample of sightlines through the halos of LRGs will be able to inform us how often these broad absorbers occur.
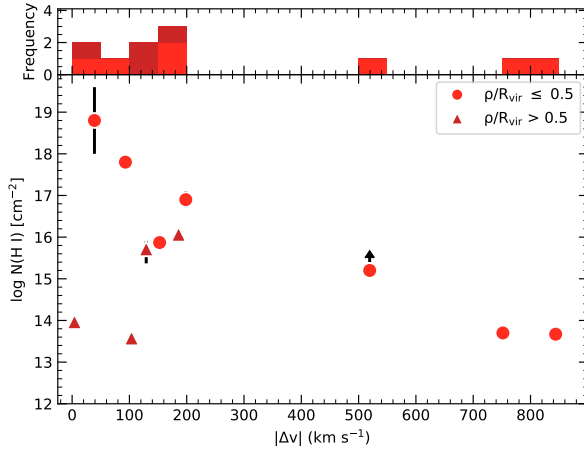
The RDR LRGs exhibiting high H I column densities ($\log N({\rm H\,I}) > 16.0$) have associated metal-line absorption. We do not have uniform spectral coverage for each sightline, so the ions we probe vary (see Appendix A). For several of our sightlines (16/21) we cover O VI and can estimate its column density, which is the focus of Paper II. For pLLSs/LLSs, C III is often one of the most prominent ions. We find absorption limits or detections of C III spanning the range $12.58 \leq \log N({\rm C\,III}) \leq 14.27$, with detections in four RDR LRGs. We calculate the covering factor (see below) for C III to be $f_c(\rho \leq 0.5\,R_{\rm vir}) = 0.50 \pm 0.18$ and $f_c(\rho \leq R_{\rm vir}) = 0.41^{+0.15}_{-0.14}$ (68% confidence interval). We find no inconsistencies between our Mg II equivalent width distribution and that presented by Huang et al. (2016), although we have a limited sample.

4.2. Covering Factor of Strong H I About LRGs

Covering factors can be used to characterize the CGM about different classes of galaxies allowing for quantitative comparisons. In addition, simulations often report covering factors of different ions, and their treatment of the CGM can be assessed by comparing to observational results. We split the sightlines into bins of impact parameter and determine the ratio of absorbers detected, for a limiting $\log N({\rm H\,I})$, to the total number of sightlines in each bin. An absorber that meets this $\log N({\rm H\,I})$ criterion is referred to as a "hit," while those below this limit are "misses." We calculate the covering factor, f_c, of strong H I assuming a binomial distribution for the covering factor where the posterior distribution is described by a beta function. This follows from the discussion in Cameron (2011) who describes the posterior distribution of values in a Bayesian treatment of binomial-distributed data. The beta function also provides estimates of the Bayesian confidence intervals, which we utilize throughout this paper.

Figure 3. Distribution of $\log N(\mathrm{H\,I})$ versus impact parameter (left) and normalized impact parameter (right) for the LRGs in the RDR sample. The strong H I detections ($\log N(\mathrm{H\,I}) \gtrsim 16.0$) are preferentially found at low impact parameters, notably within $\rho \lesssim R_{\mathrm{vir}}$. The detections of absorption with $\log N(\mathrm{H\,I}) \leq 14.5$ are consistent with interloping Lyα forest absorbers. We expected ~ 5 such interlopers and observe five (only four data points are seen here, as one sightline has two such interlopers, and we have plotted the combined columns).

Figure 4. Distribution of $\log N(\mathrm{H\,I})$ versus the absolute value of the absorber velocity offset relative to the LRG. We split the sample by normalized impact parameter and include a histogram of the absorber velocity offsets. Only four low $\log N(\mathrm{H\,I})$ data points are seen here, as one sightline has two such absorbers, and we have plotted the combined columns.

We summarize our covering factor estimates in Table 4, giving results for three limiting column densities: $\log N(\mathrm{H\,I}) \geq 15.0$, 16.0, and 17.2. When imposing these limits we consider only the central value of our H I measurements. Except for the covering factor calculation with $\log N(\mathrm{H\,I}) \geq 15.0$, we do not include the absorber for which we could only derive a lower limit for $\log N(\mathrm{H\,I})$ in all other covering factor calculations throughout this paper. Table 4 lists the im-

pact parameter range for each bin, the mean impact parameter of sightlines within the bin, the covering factor with 68% and 95% confidence intervals, the number of sightlines probed, and the number of detected absorbers for all three H I column density limits. We plot the covering factors as a function of impact parameter and normalized impact parameter for $\log N(\mathrm{H\,I}) \geq 16.0$ in Figure 5. The horizontal error bars show the width of the bins, while the vertical error bars show the 68% confidence interval for the distribution. The covering factor within the inner 250 kpc of our sample of RDR LRGs is substantial at $f_c(\rho < 250\,\mathrm{kpc}) = 0.35^{+0.15}_{-0.13}$. The covering factor for $\log N(\mathrm{H\,I}) \geq 16.0$ within the virial radius for our sample is $f_c(\rho \leq R_{\mathrm{vir}}) = 0.27^{+0.11}_{-0.10}$. For LLS absorption with $\log N(\mathrm{H\,I}) \geq 17.2$, we find $f_c(\rho \leq R_{\mathrm{vir}}) = 0.15^{+0.10}_{-0.07}$.

The covering factor of high column density gas around LRGs is non-negligible, with 35% of LRGs showing strong H I at these columns within ~ 0.5 R_{vir} (the median $R_{\mathrm{vir}} = 516$ kpc for our sample). A similar result is found around the quiescent COS-Halos galaxies (Thom et al. 2012, see also P17). We calculate a covering factor within 160 kpc (~ 0.75 R_{vir}) for the quiescent COS-Halos galaxies of $f_c(\rho \leq 160\,\mathrm{kpc}) = 0.50 \pm 0.12$ at the same $\log N(\mathrm{H\,I})$ cutoff. C18 recently reported a covering factor $f_c(\rho \leq 165\,\mathrm{kpc}) = 0.44^{+0.12}_{-0.11}$ within 165 kpc (~ 0.33 R_{vir}) of their sample of massive galaxies for $\log N(\mathrm{H\,I}) \geq 17.2$, consistent with our results in Figure 5. While no direct simulation analogs of LRGs exist in the literature, we can extrapolate the results from Rahmati et al. (2015) to lower z. They use the EA-

GLE simulation suite to characterize the H I distribution around galaxies from $z = 4$–1. Though they do not extend the analysis to $z \sim 0.5$, they simulate galaxies up to $\log M_{200} = 13.7$. In their Figure 5 they show a covering factor for $\log N(\text{H I}) > 17.2$ of $f_c(\rho < R_{\rm vir}) \sim 0.1$ for the LRG halo mass range. Our covering factor $f_c(\rho \le R_{\rm vir}) = 0.15^{+0.10}_{-0.07}$ at the same H I cutoff is consistent with their result. Rahmati et al. (2015) report a differential $f_c \sim 0.3$ centered at $\rho/R_{\rm vir} = 0.3$ for all galaxies with $\log M_{200} > 12$ (their Figure 7); over a similar normalized impact parameter ($0 \le \rho/R_{\rm vir} \le 0.25$) we find $f_c(\rho) = 0.36^{+0.18}_{-0.16}$ for the LRGs. For optically-thick gas, the LRG observations match those from the simulations at $z = 1$. Future simulation work should consider the pLLS column density range at lower redshifts for covering factor calculations to aid in comparing with observations.

On the whole, LRGs do not make a strong contribution to the total population of pLLSs/LLSs. To assess their contribution to $d\mathcal{N}/dz$ we start with the absorber number per path for uniformly-distributed galaxies of cross section $\sigma = \pi R_{\rm vir}^2$ and number density n_0:

$$d\mathcal{N}/dX = \frac{c}{H_0} f_c(\rho \le R_{\rm vir}) \pi R_{\rm vir}^2 n_0, \qquad (1)$$

where we assume covering factors from our measurements. Connecting absorber distance to redshift path,

$$dX = \frac{H_0}{H(z)}(1+z)^2 dz, \qquad (2)$$

we find

$$
\begin{aligned}
d\mathcal{N}/dz = &\frac{c}{H_0} f_c(\rho \le R_{\rm vir}) \pi R_{\rm vir}^2 \\
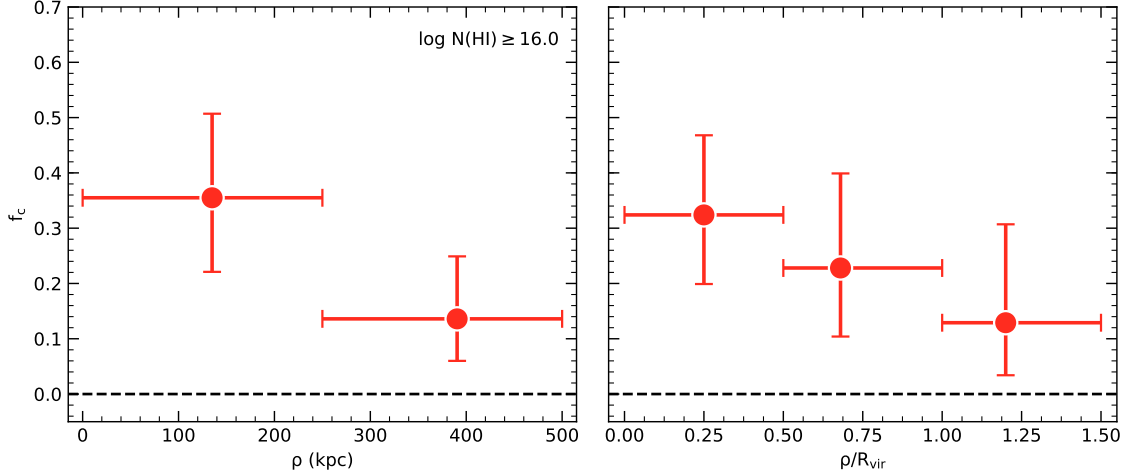&\times n_0 (1+z)^2 [\Omega_\Lambda + (1+z)^3 \Omega_m]^{-1/2}
\end{aligned} \qquad (3)
$$

(Padmanabhan 2002; Prochaska et al. 2010; Ribaudo et al. 2011). In these equations c is the speed of light, $f_c(\rho \le R_{\rm vir})$ is the covering factor, $R_{\rm vir}$ is the median virial radius for our sample, n_0 is the number density of LRGs, $H(z)$ is the Hubble parameter, and z is the median redshift of our sample. All other variables are defined in § 1. The physical number density of LRGs at $z = 0.5$ is listed in Table 1 of Almeida et al. (2008), and we adopt the fiducial value $n_0 \approx 10^{-4} h^3$ Mpc^{-3}. The contribution of LRGs to the combined pLLS and LLS population ($\log N(\text{H I}) \ge 16.0$) is $d\mathcal{N}/dz = 0.05 \pm 0.02$. The distribution calculated in Shull et al. (2017) that includes pLLSs has a value of $d\mathcal{N}/dz = 2.24$ at $z \sim 0.5$. For LLS absorption ($\log N(\text{H I}) \ge 17.2$), we find $d\mathcal{N}/dz = 0.03^{+0.02}_{-0.01}$ for the LRG contribution. The line density of LLSs calculated by Ribaudo et al. (2011) has

a value of $d\mathcal{N}/dz = 0.5$ at $z \sim 0.5$. Thus, LRGs contribute only a few percent of the population of strong H I absorbers.

4.3. An Extended Sample of Galaxy-Selected CGM Measurements

To understand the nature of strong CGM absorption systems, we compare and combine the RDR sample with the galaxy-selected COS-Halos survey (Tumlinson et al. 2013; P17) and the recent C18 LRG study. We show in Figure 6 the distributions of stellar mass as a function of normalized impact parameter at which each of the galaxies is probed in this combined sample, and the galaxy color versus stellar mass. We make use of the New York University Value Added Galaxy Catalog (NYU-VAGC) for the contours (Blanton et al. 2005). The NYU-VAGC is a catalog of the photometric and spectroscopic properties (and additional derived quantities) of the galaxies in SDSS DR7. We have recalculated the virial radii and normalized impact parameters for the COS-Halos and C18 samples using the same assumptions as for our sample, starting with the stellar masses given in those works. For these calculations the COS-Halos galaxies are assumed to be centrals. As such, we estimate the satellite fraction for the survey to be 0.24 using the satellite fraction distribution from Wechsler & Tinker (2018, their Figure 4). This value does not include scatter between the stellar mass and halo properties.

The COS-Halos sample comprises 44 star-forming and quiescent galaxies, with $\log M_\star = 9.5$–11.5, and a median galaxy redshift of $z \sim 0.2$ (Werk et al. 2012). As this sample is galaxy-selected, it has well-constrained host galaxy properties, and the sightlines extend to an impact parameter of 160 kpc (0.75 $R_{\rm vir}$ for their mean galaxy). The COS-Halos galaxies were selected to be relatively isolated, but this did not always turn out to be the case (Werk et al. 2012). The COS-Halos sample does not lie in the same redshift range as the RDR LRGs, so temporal evolution may affect our comparison. We also note that the stellar population of the RDR LRGs is intrinsically different than that of the COS-Halos sample, as are their evolutionary histories (Eisenstein et al. 2001). The C18 sample is another galaxy-selected survey comprised of 16 galaxies with $\log M_\star \ge 11$, a median redshift $z \sim 0.4$, and impact parameters $\rho \le 165$ kpc. Our sample includes five galaxies in common with the C18 sample, and the COS-Halos sample has five galaxies in common with C18. This leaves a total of six unique galaxies from C18 to include in the extended sample. In this section we focus on the COS-Halos sample, and in § 4.4 we include the C18 results.

Figure 5. H I covering factor about the RDR sample of LRGs for gas with $\log N(\mathrm{H\,I}) \geq 16.0$ as a function of impact parameter (left) and normalized impact parameter (right). The vertical error bars show the 68% confidence interval in f_c. The points are located at the mean impact parameter for each bin, while the horizontal error bars show the total extent of the bin. Note that unity covering factor is not shown.

The $N(\mathrm{H\,I})$ measurements for much of the COS-Halos sample are well constrained; however, several sightlines have H I absorption that can only be constrained by upper and lower bounds (P17). In what follows we remove three absorbers in the COS-Halos sample that have upper limits of $\log N(\mathrm{H\,I}) \leq 16.24$, 16.65, and 17.01. These upper limits are not constraining for our covering factor calculations for absorbers having $\log N(\mathrm{H\,I}) \geq 16.0$. (Removing these sightlines gives a marginal difference in the covering factor calculations. The values decrease slightly, but they are still consistent with those reported here.) Following Tumlinson et al. 2011, we cut the COS-Halos galaxies into two subsamples, defining quiescent and star forming galaxies as those with $\log \mathrm{sSFR} \leq -11$ and > -11, respectively.

The way in which we assess covering factors for the COS-Halos sample is a bit different than the approach in § 4.2. For sightlines with only H I bounds, the probability distribution function (PDF) of $\log N(\mathrm{H\,I})$ is described by a top-hat distribution between the two limits. This occurs for sightlines where the break at the Lyman limit is saturated (taking the QSO spectrum to zero flux and giving only a lower limit) and there are no detectable damping wings on Lyα (giving an upper limit). There is also one sightline where the lower limit on $N(\mathrm{H\,I})$ comes from saturated Lyα and Lyβ; in this case, we impose an upper bound of $\log N(\mathrm{H\,I}) < 18.0$ due to the lack of damping wings (J.X. Prochaska 2018, priv. comm.). When determining if these absorbers are hits or misses, we must consider the entire range of allowed values for these bounded systems. If the $\log N(\mathrm{H\,I})$ value at the low end of the interval is above

16.0, we count this absorber as a hit. However, the column density interval for several of these systems includes $\log N(\mathrm{H\,I}) = 16.0$. In these cases, if less than 50% of the interval is above $\log N(\mathrm{H\,I}) = 16.0$, we count the absorber as a miss; if it is $\geq 50\%$, we count it as a hit. All other absorbers are treated as discussed in § 4.2. We note that Howk et al. (2017) performed a similar covering factor analysis of the COS-Halos results using a Monte Carlo approach; our approach does not produce significantly different results from theirs.

We compare the covering factors of our RDR sample with the quiescent and star-forming COS-Halos samples in Figure 7, and Table 5 summarizes our derivation of covering factors for the COS-Halos galaxies as in Table 4 (we include a complementary figure and table in Appendix B for results using optically-thick absorption). We use normalized impact parameter, ρ/R_{vir}, in all comparisons. We note that the sample of star-forming galaxies is almost twice as large as the RDR sample for the inner bin. Within 0.5 R_{vir}, the star-forming galaxies have a significantly higher covering factor of high H I column gas than the LRGs with $f_c^{\mathrm{SF}} \simeq 2 f_c^{\mathrm{RDR}}$. However, both the COS-Halos quiescent galaxies and RDR LRGs have non-negligible covering factors. All three samples are consistent at larger impact parameters, $0.5 < \rho/R_{\mathrm{vir}} \leq 1.0$.

Figure 8 shows $f_c(\rho \leq R_{\mathrm{vir}})$ as a function of limiting H I column for our RDR sample compared with the COS-Halos samples. We calculate the covering factors as discussed above, using the limiting H I column density given along the horizontal axis. The RDR LRGs do not have many detections of gas within $\log N(\mathrm{H\,I}) \leq 16.0$,

and the covering factor distribution is relatively flat for lower limiting columns. The COS-Halos quiescent galaxies have several detections at lower columns and a few detections of LLSs with column densities ≥ 18.5. Among these three samples, the LRGs are unique in the lack of gas with $\log N(\text{H I}) \lesssim 16.0$ (a result that can also be seen in the C18 sample), while the passive galaxies in COS-Halos do show intermediate H I column density gas ($14.5 \leq \log N(\text{H I}) \leq 16.0$). This difference may be in part due to the differing mass distributions between the two samples or the difference in redshift. It could also be the environment of these galaxies plays a role: most of the COS-Halos galaxies are selected (imperfectly) to be isolated, while the RDR LRGs are either in clusters or dense groups (see § 2.2).

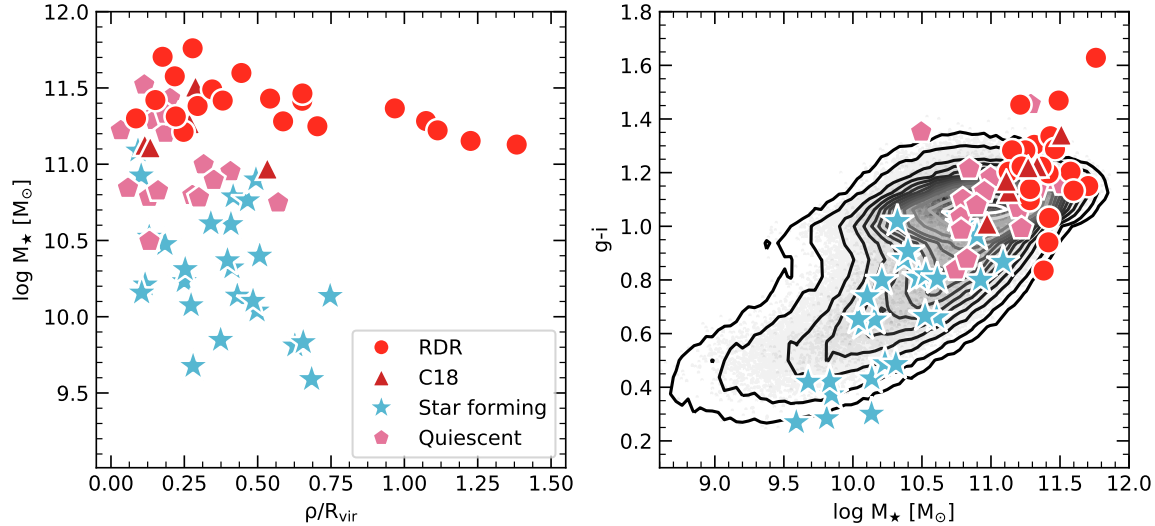### 4.4. The Mass Dependence of Strong H I Absorption

In this section we combine the RDR sample with the COS-Halos and C18 samples to assess the CGM properties across this combined sample of 71 galaxies. All of the sightlines probed were selected based on galaxy properties. We break the entire sample into bins of stellar mass and halo mass to investigate whether the properties of CGM H I absorption depend on galaxy mass. We first consider the covering factors for the combined sample in three bins of stellar mass: $\log M_\star = [9.0\text{–}10.5)$, $[10.5\text{–}11.3)$, $[11.3\text{–}12.0]$. We choose one of the boundaries at $\log M_\star = 10.5$ because this is the stellar mass at which early theoretical arguments suggested galaxies transition from cold-mode accretion to hot-mode accretion (Cattaneo et al. 2006; Dekel & Birnboim 2006, but see Nelson et al. 2015). We split the sample at $\log M_\star = 11.3$ in an effort to have a similar number of galaxies in the two higher mass bins. Figure 9 displays the covering factors for these mass bins, and Table 6 summarizes these results (we include a complementary figure and table in Appendix B for optically-thick absorption). There is no clear difference in the covering factors across the predicted critical value of stellar mass at $R_{\text{vir}} \leq 0.5$ (even comparing all masses above $\log M_\star = 10.5$ with those below). Figure 10 shows the covering factors $f_c(\rho \leq R_{\text{vir}})$ as a function of limiting $\log N(\text{H I})$ for each mass bin, as we showed in Figure 8. This figure shows that the lack of lower H I column absorption is limited to the highest-mass galaxies. The good agreement in the curves for the two lower-mass bins suggests that any transition in CGM H I properties occurs at masses above $\log M_\star \geq 11$. Indeed, galaxies with $10.5 \leq \log M_\star \leq 11.3$ show higher covering factors at $\log N(\text{H I}) \geq 18$ than the lower-mass galaxies.

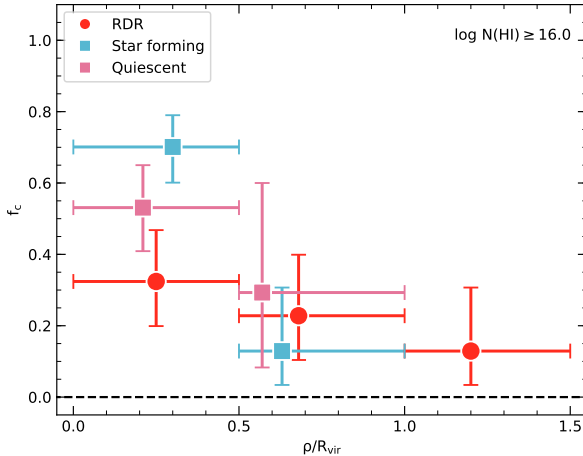Figure 11 shows the covering factors in bins of halo mass (using the scalings from stellar mass in Rodríguez-

Puebla et al. 2017). Figures 9 and 11 display the same information (with different bin boundaries), but we include both for the readers that are more familiar with galaxy properties in terms of halo mass. We bin the combined RDR, COS-Halos, and C18 sample by $\log M_{\text{h}} = [11.0\text{–}12.0]$, $[12.0\text{–}13.0]$, $[13.0\text{–}14.0]$. Table 7 gives a summary of the information from the figure (we include a complementary figure and table in Appendix B for optically-thick absorption). All three halo mass subsamples show consistent covering factors for $\log N(\text{H I}) \geq 16.0$. The lowest halo mass sample almost exclusively comprises star-forming galaxies, so this high covering factor result is consistent with Figure 7. There are several galaxies in the $[12.0\text{–}13.0]$ halo mass range that are still forming a modest amount of stars, while those in the $[13.0\text{–}14.0]$ halo mass range are all considered quiescent. These covering factors show there is a significant amount of cool gas in galaxy halos of all masses probed in this combined sample.

We can extend to even higher halo masses using galaxy clusters, the largest (often) virialized structures in the universe. These structures are roughly a factor of 10 higher in mass than the LRGs and extend to Mpc scales for R_{vir}. The baryon budget of clusters is expected to be dominated by hot X-ray emitting gas called the intra-cluster medium (ICM, the same phase that should dominate in the LRG CGM), and many satellite galaxies are undergoing gas stripping in these clusters (Gonzalez et al. 2007, 2013). Yoon et al. (2012) and Yoon & Putman (2017) studied the distribution of Lyα absorbers in the Virgo and Coma clusters. They found no detections of strong or optically-thick H I within R_{vir} when considering absorption within $\pm 1\sigma$ of the cluster velocity; most of their detections lie below $\log N(\text{H I}) \leq 14.5$. Their detections at $\rho > R_{\text{vir}}$ are more numerous, yet still below what we consider strong H I gas.[8] The covering factors within R_{vir} for the Virgo and Coma clusters at our adopted limit of $\log N(\text{H I}) \geq 16.0$ are $f_c^{\text{Virgo}}(\rho \leq R_{\text{vir}}) = 0.05^{+0.08}_{-0.04}$ and $f_c^{\text{Coma}}(\rho \leq R_{\text{vir}}) = 0.13^{+0.18}_{-0.10}$ (68% confidence interval). Burchett et al. (2018) also conducted a survey of absorption from cool gas within the ICM of five X-ray detected clusters. As with the two other cluster surveys, no strong H I was detected. We calculate the covering factor of $\log N(\text{H I}) \geq 16.0$ within R_{vir} for the X-ray clusters to be $f_c^{\text{X–ray}}(\rho \leq R_{\text{vir}}) = 0.16^{+0.21}_{-0.12}$. These results, coupled with that of Figure 11, suggest that the

---

[8] There are two detections of strong H I gas outside of the Virgo cluster virial radius and within $\pm 2\sigma$ of the cluster velocity. Both detections are in areas of un-virialized substructure that may represent a recent merger event (Yoon & Putman 2017).
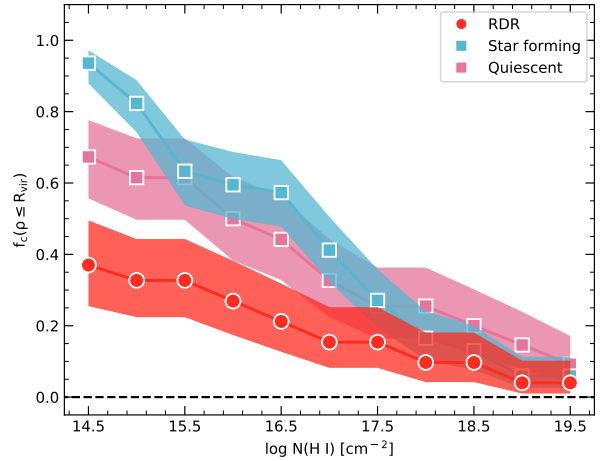
Figure 6. Distributions of stellar mass versus normalized impact parameter (left) and color versus stellar mass (right) for the combined sample: the RDR LRGs studied here, the COS-Halos sample, and the C18 sample of massive galaxies. The COS-Halos sample is split by sSFR (those with $\log \mathrm{sSFR} > -11$ are marked as "star forming"). We use our results and the COS-Halos results where they overlap the C18 sample. The contours are made using the NYU-VAGC (Blanton et al. 2005).
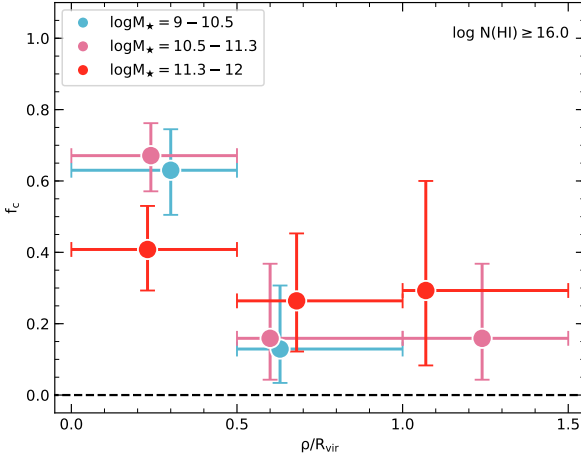

Figure 7. H I covering factor distributed by sample for gas with $\log N(\mathrm{H\,I}) \geq 16.0$ as a function of normalized impact parameter. The vertical error bars show the 68% confidence interval for the covering factor. The horizontal error bars show the extent of each bin, while the location of the data points represents the mean normalized impact parameter. Galaxies from the COS-Halos sample make up the star-forming and quiescent samples (P17). We adopt their characterization of galaxies with $\log \mathrm{sSFR} > -11$ as "star forming."

increase in mass between LRGs and clusters creates conditions that disfavor strong H I. A similar result is found in the COS-Clusters survey (Tejos et al. in prep.).

Figure 8. H I covering factor for $\rho \leq R_{\mathrm{vir}}$ as a function of limiting $\log N(\mathrm{H\,I})$ for the RDR LRGs and COS-Halos galaxies. The shaded region shows the 68% confidence interval for the distribution. The COS-Halos sample is split by sSFR ($\log \mathrm{sSFR} > -11$ is "star forming"). The RDR LRGs show a relative paucity of gas with $14.5 \leq \log N(\mathrm{H\,I}) \leq 16.0$.

In these low-redshift clusters, sightlines passing through the ICM do not exhibit strong H I absorption (but see Muzahid et al. 2017). It may be that the physical properties of the ICM are preventing the formation of cool, dense gas that would give rise to pLLSs and LLSs (e.g., as discussed in Yoon & Putman 2013 and Burchett et al. 2018), perhaps in an analogous manner to
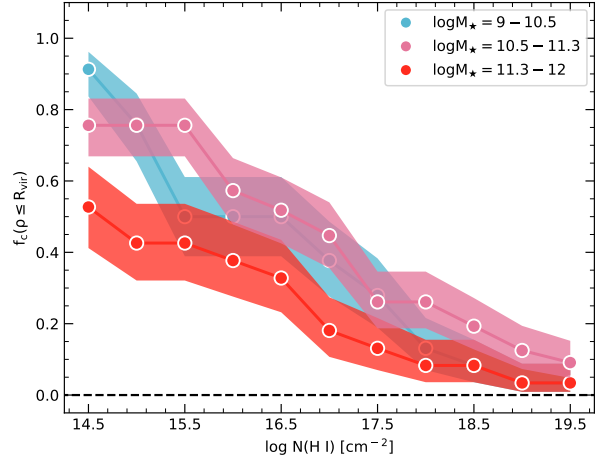
Figure 9. Stellar mass dependence of the H I covering factor ($\log N$(H I) ≥ 16.0) as a function of normalized impact parameter in our combined sample of galaxies incorporating our results with those from P17 and C18. The vertical error bars show the 68% confidence interval in f_c. The horizontal error bars show the extent of each bin, while the location of the data points represents the mean normalized impact parameter. We do not find a statistically significant difference in covering factors between host galaxy masses for these column densities.

the suppression of $\log N$(H I) $\lesssim 16$ gas in LRGs. Having said that, we note that one of the pLLSs in our sample (associated with LRG SDSSJ171651.46+302649.0) is in a redMaPPer cluster with $\lambda < 20$ (see § 2.2), so the suppression of such gas is not complete.
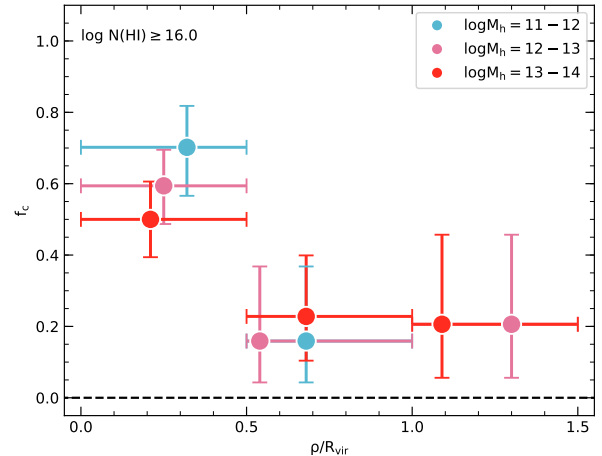
5. METALLICITIES OF STRONG H I ABSORBERS ABOUT LRGS

5.1. *Metallicity Methodology*

In the previous section, we demonstrated that the massive RDR galaxies have substantial H I gas in their CGM. By determining the metal-enrichment levels of this gas, we can start to differentiate between its plausible origins. The gas probed by pLLSs and LLSs is predominantly ionized, and large ionization corrections are required to derive the metallicity since we compare metal-ions with H I (e.g., Lehner et al. 2013; Fumagalli et al. 2016; Lehner et al. 2018; Wotta et al. 2019). To derive the metallicity, we follow the methodology of the COS CGM Compendium (CCC) where Wotta et al. (2019) derived the metallicities of 82 pLLSs and 29 LLSs using Bayesian techniques and Markov-chain Monte Carlo (MCMC) sampling of a grid of photoionization models (see Fumagalli et al. 2016). Using the MCMC sampler, we determine the posterior distribution function (PDF) of the metallicity of an absorber

Figure 10. H I covering factor for $\rho \leq R_{\rm vir}$ as a function of limiting $\log N$(H I) for our combined sample of galaxies, including our results with data from P17 and C18. The shaded region shows the 68% confidence interval for the distribution. The highest-mass galaxies (dominated by the RDR LRGs) show a relative paucity of gas with $14.5 \leq \log N$(H I) ≤ 16.0. There is no significant difference in the distributions between the low- and intermediate-mass ranges in this plot. If there is a critical mass above which cold gas becomes less common, it is significantly higher than the canonical value of $\log M_\star \approx 10.5$.

Figure 11. Halo mass dependence of the H I covering factor ($\log N$(H I) ≥ 16.0) as a function of normalized impact parameter in our combined sample of galaxies incorporating our results with those from P17 and C18. The vertical error bars show the 68% confidence interval in f_c. The horizontal error bars show the extent of each bin, while the location of the data points represents the mean normalized impact parameter. There is no statistically significant difference in the covering factors of galaxies with halo mass.

based on the likelihoods of the models in the grid to match the observed column densities. The error bars for these values are the Bayesian confidence intervals. The grid of photoionization models that we sample is made using Cloudy (version C13.02, see Ferland et al. 2013), assuming a uniform slab geometry in thermal and ionization equilibrium. The slab is illuminated with a Haardt–Madau extragalactic ultravoilet background (EUVB) radiation field from quasars and galaxies with no other local sources of ionization (we adopt HM05 as implemented in Cloudy, see Haardt & Madau 1996). The grid parameters are summarized in Table 8. We also undertook models using the HM12 EUVB and found the metallicities systematically increase by 0.1–0.5 dex, similar to the findings of Wotta et al. 2019. This is most likely due to the harder slope of the QSO spectrum in this model.

Most of the diagnostics available for the pLLSs and LLSs at $z \lesssim 1$ probe the α elements (O, Mg, Si) as well as carbon. The α elements are produced by similar nucleosynthesis processes and, since dust depletion is negligible for the densities of the pLLSs and LLSs, their relative abundances are expected to be approximately solar (Lehner et al. 2013, 2018). To describe the metallicity of the gas, we use the standard notation $[X/H] = \log(N(X)/N(H)) - \log(N(X)/N(H))_\odot$, where X here represents an α-process element (e.g., O, Mg, Si). For the pLLSs and LLSs, $[C/\alpha]$ is on average solar (Lehner et al. 2018; Wotta et al. 2019), but this ratio can depart from a solar value with $\langle [C/\alpha] \rangle = -0.05 \pm 0.35$ (Wotta et al. 2019). In our photoionization models, we therefore use a flat prior on $[C/\alpha]$ following Wotta et al. (2019). In certain cases, the metallicity and density of an absorber cannot be constrained from the observations without additional assumptions due to either not enough available metal ion measurements or the dominance of upper limits. Lehner et al. (2019, and see also Lehner et al. 2013; Wotta et al. 2016, 2019) showed that the ionization parameter ($U = n_\gamma/n_H$ = ionizing photon density/hydrogen number density) has a normal distribution in log-space for low-redshift $z \lesssim 1$ pLLSs and LLSs, which can be used as a prior for the absorbers that do not have sufficient constraints; this method provides what we describe as "low-resolution" metallicities (Wotta et al. 2016). These types of absorbers are associated with galaxies of a broad range of masses/luminosities, from sub-L* to super-L* galaxies (Lehner et al. 2013). Due to the large span in host galaxy mass, this method is viable for the absorbers associated with LRGs.

We run the MCMC analysis for the three strong H I absorbers associated with the LRGs SDSSJ111132.33+554712.8,

SDSSJ171651.46+302649.0, and SDSSJ141540.01+163336.4. We use the low-resolution method for the absorber associated with LRG SDSSJ171651.46+302649.0. Due to the range of allowed $\log N(\text{H I})$ for the LLS associated with LRG SDSSJ111508.24+023752.7, a satisfactory solution using the MCMC analysis could not be reached. Instead we estimate the metallicity using [O/H]. Metallicity estimates could not be determined for the weak H I absorbers ($\log N(\text{H I}) < 16.0$) because they have only upper limits for their metal column densities or metal ion detections that will not give reliable metallicities.

5.2. *Metallicities of LRG CGM Absorbers*

The metallicities for the four pLLSs/LLSs detected about RDR LRGs are summarized in Table 9. For each system the metallicity from our Cloudy/MCMC modeling is listed as the median value of the PDF with uncertainties reflecting the 68% confidence interval, along with the bounds of the 95% confidence interval. There are two high-metallicity absorbers with $[X/H] \geq -1$ among the four RDR systems, and one with unconstrained metallicity. The last system, associated with LRG SDSSJ171651.46+302649.0, is a low-metallicity absorber with $[X/H] = -1.87^{+0.24}_{-0.25}$ ("low-resolution" method applied, see also Wotta et al. 2016). "Corner" plots summarizing the constraints on the properties of the four pLLSs/LLSs associated with the RDR LRGs and the modeling details for each absorber are included in Appendix C.

We plot the metallicity of the RDR absorbers versus normalized impact parameter in Figure 12; we also show two absorbers from the C18 sample with metallicities from the CCC (one with new observations, see below) and the metallicity measurements for absorbers associated with the COS-Halos galaxies (P17). Out of 17 quiescent galaxies in the COS-Halos sample (defined by $\log \text{sSFR} \leq -11$), only nine have $\log N(\text{H I}) \geq 15.5$ and sufficient data to calculate an absorber metallicity. Out of 27 star-forming galaxies in the COS-Halos sample, only 16 have sufficient data and meet this $\log N(\text{H I})$ criterion. The COS-Halos metallicities in P17 were originally estimated using the HM12 EUVB.[9] To remove the systematic offset introduced when using different ionizing radiation fields to derive metallicities, all the metallicities for the COS-Halos absorbers have been recalcu-

---
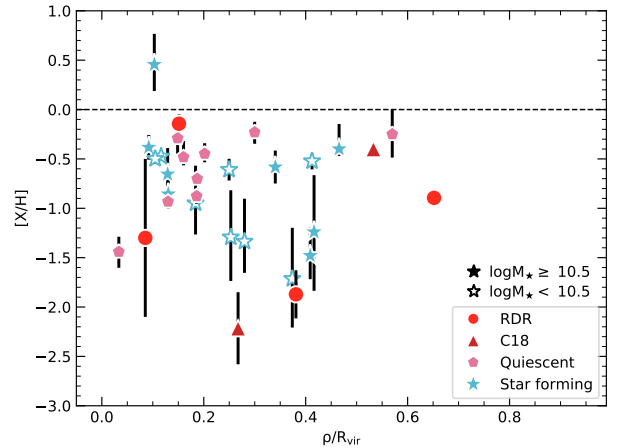
[9] The metallicity solution for J1241+5721_199_6 is not consistent with all of the observed column densities. For the SLLSs J0925+4004_196_22, J0928+6025_110_35, and J1435+3604_68_12 we use the column densities reported in Battisti et al. (2012) from their Voigt profile fits. We could not reach a satisfactory solution for J0925+4004_196_22 and instead adopt the reported [O/H] metallicity from Battisti et al. (2012) for this absorber.

lated with the HM05 EUVB and are reported in Wotta
et al. (2019) and Lehner et al. (2019).

Figure 12 shows both passive and star-forming galax-
ies have a similar broad range of metallicities. The COS-
Halos sample includes a low-metallicity absorber with
$[X/H] = -1.4 \pm 0.2$ in the CGM of a massive quiescent
galaxy. Like the $[X/H] \approx -1.8$ system associated with
our RDR LRG, this absorber is projected deep within its
halo. These systems suggest low-metallicity absorbers
might not be rare around quiescent galaxies. This re-
sult is also bolstered by a low-metallicity LLS ($[X/H] <$
-1.5) reported around an LRG in the C18 sample. We
have obtained Keck/HIRES observations that constrain
the metallicity to the range $[-2.58, -1.85]$. This ab-
sorber is not pristine, despite the lack of metal-line ab-
sorption in the COS spectrum analyzed by C18 (see Ap-
pendix D for our treatment of this absorber). The line
of sight velocities of these three absorbers are all within
$\pm 250 \, \mathrm{km \, s^{-1}}$ of their galaxy, signifying a high likelihood
of being associated.

Figure 13 shows the metallicity versus $\log N(\mathrm{H\,I})$ for
our sample of galaxy-selected clouds compared with H I
absorption-selected systems at $z < 1$. The blind H I
absorption-selected systems are shown in grey and are
from the CCC (Lehner et al. 2019; Wotta et al. 2019),
while the galaxy-selected absorbers (RDR LRGs, C18,
and COS-Halos) are shown in color. We also plot the
$\log N(\mathrm{H\,I})$ and metallicity histograms of the galaxy-
selected absorbers of star-forming galaxies (blue) and
passive galaxies (red, which includes the RDR LRGs,
C18, and COS-Halos quiescent galaxies) in the top and
right sub-panels respectively.

Overall, the LRG absorbers do not seem to be funda-
mentally different in metallicity from the other galaxy-
selected pLLSs/LLSs in spite of the different character-
istics of their host galaxies. There is also no appreciable
difference between the metallicity distributions of the
star-forming and passive samples; most of the metallic-
ity values lie between solar and a tenth solar, which can
be explained by enrichment from stellar outflows or tidal
material (Lehner et al. 2013), and both samples have
a similar fraction (∼30%) of low-metallicity absorbers
($[X/H] < -1$). There is also no appreciable differ-
ence between the distributions of star-forming galaxies
split by stellar mass. Using a two-sample Kolmogorov-
Smirnov test and K-sample Anderson-Darling test, we
cannot reject the null hypothesis that the star-forming
and passive metallicity distributions are drawn from the
same population at better than 0.5 significance. We can-
not reject the null hypothesis that the $\log N(\mathrm{H\,I})$ values
are drawn from the same distribution either. Thus, there
is no evidence the metallicity of the cool CGM—at least
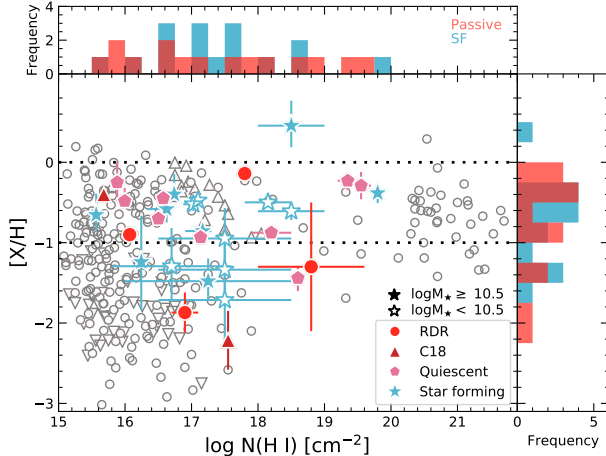

Figure 12. Metallicities of our combined sample of galaxy-
selected pLLSs/LLSs versus normalized impact parameter.
COS-Halos galaxies are split between star-forming and qui-
escent subsets at $\log \mathrm{sSFR} = -11$. Open symbols repre-
sent galaxies with $\log M_\star < 10.5$. We include only absorbers
with $\log N(\mathrm{H\,I}) \geq 15.5$ with sufficient constraints to robustly
calculate the metallicities. The metallicities for the COS-
Halos and one C18 absorber are drawn from the CCC (Lehner
et al. 2018; Wotta et al. 2019); thus, they are computed in a
manner consistent with the results presented here. See Ap-
pendix D for information on the low-metallicity absorber in
C18.

for absorbers in the range $15.5 \lesssim \log N(\mathrm{H\,I}) \lesssim 20$—is
correlated with the galaxies' star-forming properties (al-
though the samples are small). The LRG absorbers also
have metallicities and H I column densities consistent
with the distributions in pure H I absorption-selected
systems. We find no significant difference between the
absorption-selected and galaxy-selected absorbers.

5.3. *Relative Abundances of Fe II and Mg II*

For four of the LRG-associated absorbers, we have
measurements of $\log N(\mathrm{Fe\,II})$ and $\log N(\mathrm{Mg\,II})$ from
Keck/HIRES. We find a large spread in the val-
ues of $[\mathrm{Fe\,II/Mg\,II}] \equiv \log N(\mathrm{Fe\,II}) - \log N(\mathrm{Mg\,II}) -$
$\log(\mathrm{Fe/Mg})_\odot$ in these absorbers. This ratio does
not include ionization corrections; Zahedy et al.
(2017) have argued ionization corrections should be
small given the similarity of the ionization poten-
tials between Fe II and Mg II (although see Ap-
pendix D). Two of these absorbers exhibit super-
solar values: LRG SDSSJ111508.24+023752.7 and
LRG SDSSJ135726.27+043541.4 (a galaxy from C18;
cf., Appendix D) have $[\mathrm{Fe\,II/Mg\,II}] = +0.37 \pm$
0.03 and $[\mathrm{Fe\,II/Mg\,II}] = +0.50 \pm 0.08$, respectively.
The other two sightlines can only be given upper
limits: LRG SDSSJ111132.33+554712.8 and LRG

Figure 13. Metallicities versus $\log N(\text{H I})$ for absorption-selected systems from the CCC (grey symbols with downward- and upward-facing triangles being upper and lower limits, Lehner et al. 2019; Wotta et al. 2019) and our combined sample of galaxy-selected systems (colored, consisting of the RDR LRGs, C18, and COS-Halos samples). All absorbers are at $z \lesssim 1$. The dotted lines mark solar and 10% solar metallicity. The vertical error bars for the galaxy-selected absorbers represent 68% confidence intervals (except for the two absorbers previously noted to be confined to a range of values). The error bars for the absorption-selected systems are not plotted, but they are similar to those from the galaxy-selected systems. The metallicities for the COS-Halos and one of the C18 absorbers are drawn from the CCC (Lehner et al. 2019; Wotta et al. 2019). The top sub-panel shows a histogram of the $\log N(\text{H I})$ distributions for the galaxy-selected absorbers, and the right sub-panel shows a histogram of the metallicity distributions for the galaxy-selected absorbers (central values are used for the histograms). The red histograms are a combination of all three passive galaxy samples (RDR LRGs, C18, and the COS-Halos quiescent galaxies).

SDSSJ171651.46+302649.0 show [Fe II/Mg II] < -0.59 (saturated Mg II) and [Fe II/Mg II] $< +0.03$ (Fe II upper limit), respectively. The impact parameters for these absorbers are $\rho = 44$, 130, 81, and 207 kpc.

The observed [Fe II/Mg II] ratios are not correlated with metallicity. The low-metallicity absorber associated with LRG SDSSJ135726.27+043541.4 displays a highly super-solar [Fe II/Mg II] ratio, whereas LRG SDSSJ171651.46+302649.0 exhibits a near solar value of [Fe II/Mg II], despite having a metallicity that is 1.5% solar. The absorber associated with LRG SDSSJ111132.33+554712.8 has the highest metallicity ([X/H] ≈ -0.14), yet it has the lowest [Fe II/Mg II] of all four sightlines, a highly sub-solar value. (A broad range of metallicities are allowed for the absorber associated with LRG SDSSJ111508.24+023752.7.)

Zahedy et al. (2017) have discussed enhanced Fe II columns compared to α element columns around massive red galaxies, arguing that some enhancement can be explained due to the enhanced contribution from Type Ia supernova ejecta from these galaxies' evolved stellar populations. They found individual components with significant Fe enhancement, though their average value was [Fe II/Mg II] $\approx +0.02$ for sightlines within ~ 60 kpc of their galaxies. Our two detected absorbers are at significantly higher [Fe II/Mg II] than their mean, and only one sightline is located at a low impact parameter. The absorbers in our sample do not seem to follow a radial trend in enhancement.

Though we do not know the specifics of the satellite galaxies around the RDR LRGs, Chen et al. (2019) investigated the environment around LRG SDSSJ135726.27+043541.4. This LRG is housed within a group, but it is the only massive galaxy. Since this absorber exhibits the highest [Fe II/Mg II] ratio, it is unclear how such an enhancement occurred at such large distances from the central, massive galaxy. Future studies of LRGs and other massive galaxies will need to measure this ratio and the absorber metallicity in order to increase our understanding of the Fe enrichment of their CGM.

6. DISCUSSION

Using a sample of 21 LRGs with UV observations of background QSOs with $\rho \lesssim 500$ kpc, we have mapped the distribution of cool, neutral hydrogen absorption in the CGM of these massive galaxies. We have measured the covering factor and metallicity of gas with $\log N(\text{H I}) \geq 16.0$ in the CGM of LRGs. We find substantial covering factors, especially in the inner regions of the CGM. The covering factor within R_{vir} for our sample is $f_c(\rho \leq R_{\text{vir}}) = 0.27^{+0.11}_{-0.10}$. The metallicities of the absorbers are mixed, with both metal-rich systems at [X/H] $\gtrsim -1$ and metal poor with metallicities as low as [X/H] ≈ -1.8. The covering factors observed about the RDR LRGs are about 1/2 of those seen in lower-mass star-forming galaxies; the metallicity distributions of strong H I absorbers about LRGs are consistent with those observed about lower-mass galaxies.

6.1. Mass of Cool Gas in the LRG CGM

To assess the relative importance of this cool H I to the overall mass budget of the LRGs, we calculate the mass of cool gas associated with the measured H I as:

$$M_{\text{CGM}}^{\text{cool}}(\text{H I}) \simeq \int_{\rho_{min}}^{\rho_{max}} m_p N(\text{H I}) \, 2\pi\rho f_c(\rho) \, d\rho, \qquad (4)$$

where $N(\text{H I})$ is a function of the impact parameter ρ. We do not have good constraints on the func-

tional distribution of $N(\text{H I})$ or the covering factor for $\log N(\text{H I}) \geq 16.0$, so we instead break this integral up into two discrete bins $[\rho_{min}, \rho_{max}] = [0, 0.5\ R_{\text{vir}}]$ and $(0.5\ R_{\text{vir}}, R_{\text{vir}}]$, assuming constant $\langle N(\text{H I})\rangle$ and $f_c(\rho)$ in each bin. For this calculation and those that follow we use the median $\log N(\text{H I})$ value for the LLS associated with LRG SDSSJ111508.24+023752.7. The sum of these two bins gives the typical total H I mass per LRG, $M_{\text{CGM}}^{\text{cool}}(\text{H I}) \approx 1 \times 10^9\ \text{M}_\odot$. We estimate the total cool gas mass as $M_{\text{CGM}}^{\text{cool}} = \mu M_{\text{CGM}}^{\text{cool}}(\text{H I})/x(\text{H I})$, where the average ionization fraction of H I for the pLLSs/LLSs comes from the best-fit Cloudy models, and $\mu = 1.4$ to account for helium. The typical LRG has a total cool CGM mass of $M_{\text{CGM}}^{\text{cool}} \approx 1 \times 10^{11}\ \text{M}_\odot$ in its halo, assuming the average value $x(\text{H I}) = 0.01$ from our Cloudy calculations (our absorbers exhibit a range $0.002 \leq x(\text{H I}) \leq 0.02$ consistent with Lehner et al. 2019). This mass is 2.5 times larger than the estimate in Zahedy et al. (2019). Compared to the expected baryonic mass for these galaxies,$M_b = M_h(\Omega_b/\Omega_m) \approx 4 \times 10^{12}\ \text{M}_\odot$, only $\sim$3% of the baryons is in the cool CGM, while $\sim$6% is in stars. If the hot gas in the LRG halo dominates the remaining baryon mass, it could represent $> 10^{12}\ \text{M}_\odot$.

The total cool CGM mass has also been calculated around L^* galaxies. The COS-Halos sample, treated as one halo with many sightlines, has $M_{\text{CGM}}^{\text{cool}} \approx 9 \times 10^{10}\ \text{M}_\odot$ within $\rho = 160$ kpc (P17, but see Bregman et al. 2018). Keeney et al. (2017) supplemented the COS-Halos sample with measurements extending to R_{vir}; they adopted different assumptions for the structure and ionization of the gas to determine $M_{\text{CGM}}^{\text{cool}} \approx 3 \times 10^{10}\ \text{M}_\odot$. The cool CGM mass of M31 is estimated to be $M_{\text{CGM}}^{\text{cool}} \gtrsim 10^9$ $\text{M}_\odot$ within R_{vir} assuming a solar metallicity for the gas (Lehner et al. 2015).[10] However, while the cool CGM mass in LRGs is comparable to that for lower-mass galaxies, it is a much smaller fraction of the total baryons given their larger halo mass. For the RDR sample, the cool CGM is $\sim$40% of the stellar mass of the galaxy. M31 shows a 10% fraction, while the COS-Halos galaxies (and the extended Keeney et al. 2017 results) have almost twice as much mass in the cool CGM as the stellar disk. That said, the cool CGM gas in LRGs is not unimportant as we show below.

6.2. *Origins and Fate of Cool Gas in LRG Halos*

Cool gas is clearly found in the halos of LRGs and other massive, quiescent galaxies (e.g., Thom et al. 2012; P17; C18; this work). Several models predict cool gas can form through cooling instabilities in the hot corona

---

[10] The erratum for Lehner et al. (2015) lists this updated cool CGM mass estimate.

and fall onto the central galaxy in high-mass halos (e.g., Maller & Bullock 2004; Voit et al. 2017; Correa et al. 2018). Metal-rich gas can more efficiently cool and condense out of the hot halo due to the increased number of cooling channels. Coupled with the shorter cooling time associated with denser gas, we expect condensation is most prevalent at smaller radii (e.g., see the definitions of the cooling or precipitation radii in Voit et al. 2015; Correa et al. 2018). For metal-rich gas with $[\text{X/H}] \approx 0$, the ratio of the cooling to free-fall time is $t_{\text{cool}}/t_{\text{ff}} \lesssim 10$—a characteristic criterion for the formation of thermal instabilities in galaxy halos (Sharma et al. 2012)—at $r \lesssim 0.5\ R_{\text{vir}}$ (assuming a gas profile following Mathews & Prochaska 2017, cooling losses from Gnat & Sternberg 2007, and a Navarro et al. 1996 mass profile). For metallicities below $[\text{X/H}] \lesssim -1$, gas within $r \lesssim 0.25\ R_{\text{vir}}$ typically meets these criteria. Certainly the absorbers we find around LRGs have higher column densities on average at smaller impact parameters, and the highest metallicity gas is seen within $\rho \lesssim 0.25\ R_{\text{vir}}$ in Figure 12. Thus, the high metallicity absorbers could plausibly represent gas precipitated from the corona.

However, the lowest metallicity gas in our combined sample of massive galaxies is also seen in the inner CGM within ± 250 km s^{-1} of the galaxy. The $[\text{X/H}] \approx -1.8$ absorber reported here is found at $\rho \approx 0.4\ R_{\text{vir}}$, while the $[\text{X/H}] = [-2.58, -1.85]$ system drawn from the C18 sample is at an impact parameter $\rho \approx 0.3\ R_{\text{vir}}$. It is difficult to imagine such low-metallicity gas could have condensed out of the halo, as the typical corona about galaxies with masses similar to our RDR sample are expected to be significantly more metal rich (e.g., the ICM of clusters is often quite metal rich, Mernier et al. 2018, while the Milky Way corona is thought to have $[\text{X/H}] \gtrsim -0.7$, Miller & Bregman 2013). As such, this low-metallicity material could be material accreted from the IGM or stripped from an infalling satellite galaxy. As we discuss below, cold gas like this would be susceptible to relatively rapid evaporation if embedded within a diffuse, hot corona, which makes the direct accretion scenario problematic. On the other hand, extremely-metal-poor dwarf galaxies with $[\text{X/H}] \lesssim -1.5$ are rare enough (Izotov et al. 2018) that it is also difficult to explain the prevalence of very-metal-poor pLLSs/LLSs seen at low redshift through satellite stripping (Lehner et al. 2013; Wotta et al. 2019). Given these difficulties, the origins of the gas are not yet clear. While it is possible to explain the more metal-rich gas as material directly condensed from a hot corona (similar to hot-mode accretion or precipitation models) or through satellite stripping, this cannot universally explain the cold, dense gas we see in the CGM of LRGs.

Another potential source for the absorbers we observe is recycled winds. Stellar winds do not seem to be a likely source for this gas, as the LRGs have had no star formation for the past Gyr (Gauthier & Chen 2011b). We also do not see any signatures of stellar winds in the kinematics of the gas (e.g., extended velocity profiles) like those observed around starburst galaxies (Heckman et al. 2017). AGN winds are also unlikely since we do not see a strong population of AGN in LRGs, indicating the duty cycle is long. In addition, the timescale for recycling an AGN wind for the LRG mass scale is $10^8 - 10^9$ yr (Oppenheimer et al. 2010). The most recent AGN outburst would need to be ∼Gyr ago for us to be detecting the gas now. This AGN activity would be less cyclic and more sporadic (see also Afruni et al. 2019). Even though we can rule out recent winds as a potential source, it is possible the absorbers are material recycling from an ancient outflow that was blown out of the galaxy when the AGN was active or star formation was occurring. This could be the origin of the super-solar [Fe II/Mg II] abundances observed in two of the absorbers.

The ultimate fate of the cool gas we detect is clearly not surviving the fall into the center of the galaxy and fueling star formation. If all of the mass of the cool CGM were to collapse to the central galaxy within a free-fall time (see below) from $R_{\rm vir}$, $t_{\rm ff}(R_{\rm vir})$, then the galaxy would have sSFR $\sim 10^{-10}$ yr^{-1}, assuming maximum efficiency. We do not see sSFRs this high for the LRGs frequently (and the [O II] emission seen in these galaxies may not trace star formation). It appears that much of the cool CGM gas does not actually make it to the galaxy cold, or it is somehow kept from forming stars if it does reach the central galaxy.

It is not clear that we expect the gas to survive such a fall through the corona of the LRGs. Here we consider the evaporative destruction timescales for dense, cool gas in a hot LRG corona, comparing it with typical free-fall times. We calculate the expected evaporation timescale for a spherical cloud in the halo of an LRG following Maller & Bullock (2004) and the discussion in Gauthier & Chen (2011a). Specifically, we evaluate equation 35 from Maller & Bullock (2004) as

$$\tau_{\rm evap} \simeq (16\,{\rm Gyr}) \left(\frac{n_H m_p (4/3)\pi r_{\rm cl}^3}{10^6\,{\rm M}_\odot} \right)^{2/3}$$
$$\times \left(\frac{T}{10^6\,{\rm K}} \right)^{-3/2} \left(\Lambda_z \frac{t_f}{8\,{\rm Gyr}} \right)^{-1/3}. \quad (5)$$

We calculate the virial temperature of the median LRG halo (e.g., equation 1 of Oppenheimer et al. 2016) $T_{\rm vir} = 6 \times 10^6$ K. We adopt $\Lambda_z = 1.0$ for the metallicity scaling of the cooling function (Appendix A in Maller & Bullock

2004), which is appropriate for gas with 0.1 Z$_\odot$, close to the mean metallicity of the LRG absorbers in our study (0.11 Z$_\odot$). We assume t_f, the halo formation time, is the age of the universe at $z \sim 0.5$. We adopt the average density for the absorbers calculated from the best-fit Cloudy models, $n_H = 10^{-2.4}$ cm^{-3}; for the radius of the cloud we use half of the average length scale of the absorbers, $r_{\rm cl} = 0.5 \times l = 0.5 \times N_{\rm HI}/x({\rm H\,I})n_H \approx 0.8$ kpc. These values are comparable to the median values seen in the Lehner et al. (2019) sample of pLLSs/LLSs. These assumptions give an evaporation timescale of $\tau_{\rm evap} \sim$ 440 Myr.

For these clouds to survive to accrete into the center of the galaxy, the evaporation timescale should be greater than the free-fall timescale, $t_{\rm ff}$. We assess $t_{\rm ff}$ at $R_{\rm vir}$ and 0.5 $R_{\rm vir}$ for an LRG halo, evaluating the expression

$$t_{\rm ff} = \left(\frac{3\pi}{32G\bar{\rho}} \right)^{1/2}, \quad (6)$$

where the average density $\bar{\rho} = 3M_{\rm encl}/4\pi R^3$. For the calculation at $R = R_{\rm vir}$ we adopt the median $M_{\rm h}$ of our sample for $M_{\rm encl}$. This yields $t_{\rm ff}(R_{\rm vir}) \sim 1.3$ Gyr. For $R = 0.5\,R_{\rm vir}$ we integrate the Navarro-Frank-White density profile (Navarro et al. 1996, 1997) for a dark matter halo to determine the mass enclosed within a radius r. Using a concentration parameter, $c = R_{200}/R_s = 3.7$, from Shan et al. (2017, their Equation 8 and the Table 2 parameterizations for $0.4 \leq z \leq 0.6$) and our values for $R_{\rm vir} \equiv R_{200}$, we find $t_{\rm ff}(0.5\,R_{\rm vir}) \sim 600$ Myr.

These considerations suggest that if a cloud falls into the halo from the IGM it is unlikely to survive to the center of the LRG before evaporating. As discussed above, however, there is not another obvious way to produce cool gas with small velocity offsets and metallicities as low as we observe deep in the halos of quiescent, massive galaxies (but see Peeples et al. 2019). More metal-rich gas that condenses from the corona within $\rho \lesssim 0.5\,R_{\rm vir}$ may roughly remain intact to the centers of the LRGs. However, even if the cool gas from the inner CGM makes it to the center of the galaxy, it evidently does not fuel significant star formation.

AGN feedback could plausibly play a role in this. While LRGs do not house many active AGN (Sadler et al. 2007; Hodge et al. 2008, 2009), the duty cycle of such AGN is not well-known. Most LRG AGNs could be in a quiescent state awaiting the build-up of a cool gas reservoir to fuel its ignition, as in the precipitation model proposed by Voit et al. (2017). However, due to the short feedback cycle in this model, it seems unlikely AGN would be the cause of the quenched star formation we currently see. We note that these calculations have, of course, been done in the absence of magnetic fields,

which could significantly affect the conductive evaporation timescales (e.g., Lan & Mo 2019). However, even if the timescale is increased and the gas is able to survive into the halo core, we still do not see the gas being transformed into stars due to the low SFRs.

There may be evidence in the distribution of H I column densities in the most massive halos that evaporation or some other destructive mechanism is at work. The paucity of H I absorption systems below $\log N(\text{H I}) \lesssim 16$ about the most massive galaxies may be due to the destruction of the clouds that would lead to such absorption. There is no lack of such absorption in lower-mass galaxies (e.g., Keeney et al. 2017, P17). This difference can be seen in Figure 10, where the covering factor continues to rise towards lower column densities in the two lower bins of galaxy mass ($\log M_\star \lesssim 11.3$), while it is consistent with a flat profile for the highest-mass galaxies. If the lower column density gas is on average lower density, it may be more susceptible to evaporative destruction in the dense, hot coronae about the most massive galaxies. Radiative and other feedback effects, especially from AGN, could also play a role in suppressing the amount of low column density gas in the halos of massive galaxies, although this effect should also be present in lower-mass systems.

7. SUMMARY AND CONCLUDING REMARKS

This paper presents the first results from the RDR survey. We analyze the CGM of 21 LRGs at $z \sim 0.5$ using UV spectroscopy of background QSOs projected within $\rho \leq 500$ kpc. We measure the covering factor of H I about the RDR LRGs and determine the metallicity of the strong H I absorbers. Our main results are as follows.

1. We detect H I absorption in 11/21 sightlines in the CGM of LRGs. We detect four strong H I absorbers: two pLLSs and two LLSs. There is a dearth of absorption between $14.5 \leq \log N(\text{H I}) \leq 16.0$, and we show that any absorbers with $\log N(\text{H I}) \leq 14.5$ most likely arise in the IGM. The covering factor of strong H I absorption about the RDR LRGs at small impact parameters is $\sim 1/2$ that seen about lower-mass star-forming galaxies. The covering factor for $\log N(\text{H I}) \geq 16.0$ about LRGs is $f_c(\rho \leq R_{\text{vir}}) = 0.27^{+0.11}_{-0.10}$.

2. Combining our data with previous galaxy-selected samples (P17; C18), we estimate the covering factors of H I as a function of galaxy mass. The covering factor of gas with $\log N(\text{H I}) \gtrsim 16.0$ in the highest-mass galaxies ($\log M_\star \gtrsim 11.3$) is marginally smaller than that of lower-mass galaxies (differences at only the $\sim 1\sigma$ level). If there is a transition between hot- and cold-mode accretion with mass, it shows little signature in strong H I systems. Lower-mass galaxies have significantly higher covering factors for gas with $14.5 \leq \log N(\text{H I}) \leq 16.0$, which is generally not seen in the highest-mass galaxies.

3. We estimate the metallicity of the four strong H I absorbers about the RDR LRGs. Two of these are metal-rich with $[\text{X/H}] \geq -1$, one is unconstrained, and the fourth absorber is metal-poor at $[\text{X/H}] \approx -1.8$. Other identifications of metal-poor absorbers in the inner halos of massive galaxies have been reported in the literature. Although the sample is still small, these metal-poor absorbers do not appear to be rare in the CGM of LRGs. The frequency of low-metallicity systems is also similar between star-forming and quiescent galaxies. There is no statistically significant difference in the metallicity distributions of cool CGM gas as a function of stellar mass.

Our observations represent tests of our understanding of the gaseous environments of massive galaxies, including our prevailing theories of how galaxies accrete gas. We have found plentiful dense, cold gas surviving deep in the halos of very massive galaxies. The mass of this gas is similar to that found in lower-mass star-forming galaxies, although it represents a lower fraction of the total baryonic mass in the high-mass halos.

The metal-rich cool gas we observe could plausibly have condensed from the dense halos in these galaxies. If the coronae of these galaxies contain a majority of their halo's baryons, the inner regions may have conditions in which sustained formation of cool clouds via thermal instabilities is possible. The high column density (high density) gas we observe is concentrated toward the inner regions (at least in projection), as expected if the gas is condensing from the highest-density (and perhaps highest-metallicity) regions of the corona, where the cooling times are shortest. The relatively small velocity offsets between the cold gas and the central galaxies is also consistent with this origin, as has been noted previously for more massive, quiescent galaxies (e.g., Thom et al. 2012; Tumlinson et al. 2013).

At the same time, cooling from the corona cannot be the entire story. The metal-poor absorbers seen in our RDR sample and others (P17; C18), with metallicities below $[\text{X/H}] \lesssim -1.8$, cannot be explained in this way, as the coronae of these massive galaxies should have metallicities in excess of $[\text{X/H}] \gtrsim -1$, if not substantially higher (Miller & Bregman 2013; Mernier et al.

2018). While in principle such gas could arise as matter being stripped from very-low-mass dwarf satellites, we argue that this is unlikely given their frequency and the small impact parameters at which we see such gas (and it would require the galaxy to maintain its gas to small impact parameters against ram-pressure stripping and probably the dwarf to be on its first pass close to the central halo). Alternatively, the low-metallicity cold gas may have arisen in the IGM and remained cold through a putative accretion shock, surviving against evaporation as it fell. This is not entirely satisfying either, unless we have misunderstood the importance of these phenomena.

If there is a critical mass above which massive cold clouds are unable to exist for a significant amount of time, it is not clear from our measurements. We find similar covering factors with mass and find metal-poor absorbers in high-mass galaxies with roughly the same frequency as seen in lower-mass systems. The only clear distinction between clouds in the highest-mass halos and those about lower-mass galaxies is at column densities $\log N(\text{H I}) \lesssim 16.0$, which are essentially absent in the highest-mass galaxies ($\log M_\star \gtrsim 11.3$). The lack of O VI in these halos (see Paper II) also indicates there is little cool gas at very low densities, $\log n_{\text{H}} \lesssim -4$ (e.g., Stern et al. 2018; Roca-Fàbrega et al. 2019), which would give rise to photoionized O VI. This may imply gas below some critical density is readily evaporated, heated, and ionized to a point where it is not detected in our H I selection, while the higher density gas can survive. However, the survival of cold gas at small impact parameters may be telling us that the evaporation within a diffuse hot corona must consider other mitigating factors, such as magnetic fields.

Even though the LRGs have a supply of cool gas at low impact parameters, some process must be at work either keeping it from reaching the central galaxy or from cooling further and forming stars. The presence of these clouds coupled with the lack of significant star formation in the central regions implies there is a mechanism actively quenching the formation of stars from this material on the timescale of < 1 Gyr.

In the second paper in this series (Paper II), we focus on the high-ionization phase of the CGM traced by O VI for the RDR sample of LRGs (see also Zahedy et al. 2019). We are also conducting a survey to observe the CGM of 50 LRGs within ~ 0.3 R_{vir} with HST/COS. We will employ these data to further delineate the metallicity distribution function of CGM absorbers about LRGs.

gether with the Notre Dame Cooperative Computing Lab, through the HTCondor software.

Facilities: HST (COS, FOS), Keck:I (HIRES), Sloan

Software: astropy (Astropy Collaboration et al. 2013; The Astropy Collaboration et al. 2018), Cloudy (Ferland et al. 2013), Matplotlib (Hunter 2007)

REFERENCES

Abolfathi, B., Aguado, D. S., Aguilar, G., et al. 2018, ApJS, 235, 42

Afruni, A., Fraternali, F., & Pezzulli, G. 2019, A&A, 625, A11

Albareti, F. D., Allende Prieto, C., Almeida, A., et al. 2017, ApJS, 233, 25

Almeida, C., Baugh, C. M., Wake, D. A., et al. 2008, MNRAS, 386, 2145

Anderson, M. E., Bregman, J. N., & Dai, X. 2013, ApJ, 762, 106

Astropy Collaboration, Robitaille, T. P., Tollerud, E. J., et al. 2013, A&A, 558, A33

Banerji, M., Ferreras, I., Abdalla, F. B., Hewett, P., & Lahav, O. 2010, MNRAS, 402, 2264

Battisti, A. J., Meiring, J. D., Tripp, T. M., et al. 2012, ApJ, 744, 93

Behroozi, P. S., Conroy, C., & Wechsler, R. H. 2010, The Astrophysical Journal, 717, 379

Belfiore, F., Maiolino, R., Maraston, C., et al. 2016, MNRAS, 461, 3111

Birnboim, Y., & Dekel, A. 2003, MNRAS, 345, 349

Blanton, M. R., & Roweis, S. 2007, AJ, 133, 734

Blanton, M. R., Schlegel, D. J., Strauss, M. A., et al. 2005, AJ, 129, 2562

Bouché, N., Murphy, M. T., & Péroux, C. 2004, MNRAS, 354, L25

Bowen, D. V., & Chelouche, D. 2011, ApJ, 727, 47

Bregman, J. N., Anderson, M. E., Miller, M. J., et al. 2018, ApJ, 862, 3

Bruzual, G., & Charlot, S. 2003, MNRAS, 344, 1000

Burchett, J. N., Tripp, T. M., Wang, Q. D., et al. 2018, MNRAS, 475, 2067

Cameron, E. 2011, PASA, 28, 128

Cappellari, M. 2017, MNRAS, 466, 798

Cardelli, J. A., Clayton, G. C., & Mathis, J. S. 1989, ApJ, 345, 245

Cattaneo, A., Dekel, A., Devriendt, J., Guiderdoni, B., & Blaizot, J. 2006, MNRAS, 370, 1651

Chabrier, G. 2003, PASP, 115, 763

Chen, H.-W. 2017, in Astrophysics and Space Science Library, Vol. 430, Gas Accretion onto Galaxies, ed. A. Fox & R. Davé, 167

Chen, H.-W., Helsby, J. E., Gauthier, J.-R., et al. 2010a, ApJ, 714, 1521

Chen, H.-W., Wild, V., Tinker, J. L., et al. 2010b, ApJL, 724, L176

Chen, H.-W., Zahedy, F. S., Johnson, S. D., et al. 2018, MNRAS, 479, 2547

Chen, H.-W., Johnson, S. D., Straka, L. A., et al. 2019, MNRAS, 484, 431

Conroy, C. 2013, ARA&A, 51, 393

Correa, C. A., Schaye, J., van de Voort, F., Duffy, A. R., & Wyithe, J. S. B. 2018, MNRAS, 478, 255

Crain, R. A., McCarthy, I. G., Frenk, C. S., Theuns, T., & Schaye, J. 2010, MNRAS, 407, 1403

Danforth, C. W., Keeney, B. A., Stocke, J. T., Shull, J. M., & Yao, Y. 2010, ApJ, 720, 976

Danforth, C. W., Keeney, B. A., Tilton, E. M., et al. 2016, ApJ, 817, 111

Dawson, K. S., Schlegel, D. J., Ahn, C. P., et al. 2013, The Astronomical Journal, 145, 10

Dawson, K. S., Kneib, J.-P., Percival, W. J., et al. 2016, The Astronomical Journal, 151, 44

Dekel, A., & Birnboim, Y. 2006, MNRAS, 368, 2

Eisenstein, D. J., Annis, J., Gunn, J. E., et al. 2001, AJ, 122, 2267

Eisenstein, D. J., Zehavi, I., Hogg, D. W., et al. 2005, ApJ, 633, 560

Fakhouri, O., Ma, C.-P., & Boylan-Kolchin, M. 2010, MNRAS, 406, 2267

Ferland, G. J., Porter, R. L., van Hoof, P. A. M., et al. 2013, RMxAA, 49, 137

Ferland, G. J., Chatzikos, M., Guzmán, F., et al. 2017, RMxAA, 53, 385

Fitzpatrick, E. L., & Spitzer, Jr., L. 1997, ApJ, 475, 623

Fox, A., & Davé, R., eds. 2017, Astrophysics and Space Science Library, Vol. 430, Gas Accretion onto Galaxies

Fumagalli, M., O'Meara, J. M., & Prochaska, J. X. 2016, MNRAS, 455, 4100

Gauthier, J.-R., & Chen, H.-W. 2011a, MNRAS, 418, 2730

—. 2011b, MNRAS, 418, 2730

Gauthier, J.-R., Chen, H.-W., & Tinker, J. L. 2009, The Astrophysical Journal, 702, 50

Gnat, O., & Sternberg, A. 2007, The Astrophysical Journal Supplement Series, 168, 213

Gonzalez, A. H., Sivanandam, S., Zabludoff, A. I., & Zaritsky, D. 2013, ApJ, 778, 14

Gonzalez, A. H., Zaritsky, D., & Zabludoff, A. I. 2007, ApJ, 666, 147

Haardt, F., & Madau, P. 1996, ApJ, 461, 20

—. 2012, ApJ, 746, 125

Hausammann, L., Revaz, Y., & Jablonka, P. 2019, A&A, 624, A11

Heckman, T., Borthakur, S., Wild, V., Schiminovich, D., & Bordoloi, R. 2017, ApJ, 846, 151

Ho, L. C. 2008, ARA&A, 46, 475

Hodge, J. A., Becker, R. H., White, R. L., & de Vries, W. H. 2008, AJ, 136, 1097

Hodge, J. A., Zeimann, G. R., Becker, R. H., & White, R. L. 2009, AJ, 138, 900

Hoshino, H., Leauthaud, A., Lackner, C., et al. 2015, MNRAS, 452, 998

Howk, J. C., Wotta, C. B., Berg, M. A., et al. 2017, ApJ, 846, 141

Howk, J. C., Berg, M. A., Lehner, N., et al. 2019, in preparation

Huang, S., Leauthaud, A., Greene, J. E., et al. 2018, MNRAS, 475, 3348

Huang, Y.-H., Chen, H.-W., Johnson, S. D., & Weiner, B. J. 2016, MNRAS, 455, 1713

Hunter, J. D. 2007, Computing In Science & Engineering, 9, 90

Izotov, Y. I., Thuan, T. X., Guseva, N. G., & Liss, S. E. 2018, MNRAS, 473, 1956

Keeney, B. A., Stocke, J. T., Danforth, C. W., et al. 2017, ApJS, 230, 6

Kereš, D., Katz, N., Weinberg, D. H., & Davé, R. 2005, MNRAS, 363, 2

Lan, T.-W., & Mo, H. 2018, ApJ, 866, 36

—. 2019, MNRAS, 486, 608

Lehner, N., Howk, J. C., & Wakker, B. P. 2015, ApJ, 804, 79 (LHW15)

Lehner, N., O'Meara, J. M., Howk, J. C., Prochaska, J. X., & Fumagalli, M. 2016, ApJ, 833, 283

Lehner, N., Savage, B. D., Richter, P., et al. 2007, ApJ, 658, 680

Lehner, N., Wotta, C. B., Howk, J. C., et al. 2018, ApJ, 866, 33

—. 2019, arXiv e-prints, arXiv:1902.10147

Lehner, N., Howk, J. C., Tripp, T. M., et al. 2013, ApJ, 770, 138

Lundgren, B. F., Brunner, R. J., York, D. G., et al. 2009, ApJ, 698, 819

Maller, A. H., & Bullock, J. S. 2004, MNRAS, 355, 694

Maraston, C., Pforr, J., Henriques, B. M., et al. 2013, Monthly Notices of the Royal Astronomical Society, 435, 2764

Martin, D. C., Fanson, J., Schiminovich, D., et al. 2005, ApJL, 619, L1

Masters, K. L., Maraston, C., Nichol, R. C., et al. 2011, MNRAS, 418, 1055

Mathews, W. G., & Prochaska, J. X. 2017, ApJ, 846, L24

McCourt, M., Sharma, P., Quataert, E., & Parrish, I. J. 2012, MNRAS, 419, 3319

Mernier, F., Biffi, V., Yamaguchi, H., et al. 2018, SSRv, 214, 129

Miller, M. J., & Bregman, J. N. 2013, ApJ, 770, 118

Moustakas, J., Kennicutt, Jr., R. C., & Tremonti, C. A. 2006, ApJ, 642, 775

Muzahid, S., Charlton, J., Nagai, D., Schaye, J., & Srianand, R. 2017, ApJL, 846, L8

Navarro, J. F., Frenk, C. S., & White, S. D. M. 1996, ApJ, 462, 563

—. 1997, ApJ, 490, 493

Nelson, D., Genel, S., Vogelsberger, M., et al. 2015, MNRAS, 448, 59

Nelson, D., Pillepich, A., Springel, V., et al. 2018, MNRAS, 475, 624

Ocvirk, P., Pichon, C., & Teyssier, R. 2008, MNRAS, 390, 1326

Oppenheimer, B. D., Davé, R., Kereš, D., et al. 2010, MNRAS, 406, 2325

Oppenheimer, B. D., & Schaye, J. 2013, MNRAS, 434, 1043

Oppenheimer, B. D., Crain, R. A., Schaye, J., et al. 2016, MNRAS, 460, 2157

Oser, L., Ostriker, J. P., Naab, T., Johansson, P. H., & Burkert, A. 2010, ApJ, 725, 2312

O'Sullivan, E., Combes, F., Salomé, P., et al. 2018, A&A, 618, A126

Padmanabhan, T. 2002, Theoretical Astrophysics - Volume 3, Galaxies and Cosmology, 638, doi:10.2277/0521562422

Peeples, M., Tumlinson, J., Fox, A., et al. 2017, The Hubble Spectroscopic Legacy Archive, Tech. rep.

Peeples, M. S., Corlies, L., Tumlinson, J., et al. 2019, ApJ, 873, 129

Pérez-Ràfols, I., Miralda-Escudé, J., Lundgren, B., et al. 2015, MNRAS, 447, 2784

Planck Collaboration, Ade, P. A. R., Aghanim, N., et al. 2016, A&A, 594, A13

Prakash, A., Licquia, T. C., Newman, J. A., et al. 2016, The Astrophysical Journal Supplement Series, 224, 34

Prochaska, J. X., O'Meara, J. M., & Worseck, G. 2010, ApJ, 718, 392

Prochaska, J. X., Werk, J. K., Worseck, G., et al. 2017, ApJ, 837, 169

Rahmati, A., Schaye, J., Bower, R. G., et al. 2015, MNRAS, 452, 2034

Ribaudo, J., Lehner, N., & Howk, J. C. 2011, ApJ, 736, 42

Roca-Fàbrega, S., Dekel, A., Faerman, Y., et al. 2019, MNRAS, 484, 3625

Rodríguez-Puebla, A., Primack, J. R., Avila-Reese, V., & Faber, S. M. 2017, MNRAS, 470, 651

Rykoff, E. S., Rozo, E., Busha, M. T., et al. 2014, ApJ, 785, 104

Rykoff, E. S., Rozo, E., Hollowood, D., et al. 2016, ApJS, 224, 1

Sadler, E. M., Cannon, R. D., Mauch, T., et al. 2007, MNRAS, 381, 211

Savage, B. D., & Sembach, K. R. 1991, ApJ, 379, 245

Schlegel, D. J., Finkbeiner, D. P., & Davis, M. 1998, ApJ, 500, 525

Schneider, D. P., Richards, G. T., Hall, P. B., et al. 2010, AJ, 139, 2360

Serra, P., Oosterloo, T., Morganti, R., et al. 2012, MNRAS, 422, 1835

Shan, H., Kneib, J.-P., Li, R., et al. 2017, ApJ, 840, 104

Sharma, M., & Nath, B. B. 2013, ApJ, 763, 17

Sharma, P., McCourt, M., Quataert, E., & Parrish, I. J. 2012, MNRAS, 420, 3174

Shull, J. M., Danforth, C. W., Tilton, E. M., Moloney, J., & Stevans, M. L. 2017, ApJ, 849, 106

Singh, P., Majumdar, S., Nath, B. B., & Silk, J. 2018, MNRAS, 478, 2909

Slepian, Z., Eisenstein, D. J., Brownstein, J. R., et al. 2017, MNRAS, 469, 1738

Smailagić, M., Prochaska, J. X., Burchett, J., Zhu, G., & Ménard, B. 2018, The Astrophysical Journal, 867, 106

Spitzer, L. 1978, Physical processes in the interstellar medium, doi:10.1002/9783527617722

Stern, J., Faucher-Giguère, C.-A., Hennawi, J. F., et al. 2018, ApJ, 865, 91

Stewart, K. R., Kaufmann, T., Bullock, J. S., et al. 2011, ApJ, 738, 39

Stoehr, F., White, R., Smith, M., et al. 2008, in Astronomical Society of the Pacific Conference Series, Vol. 394, Astronomical Data Analysis Software and Systems XVII, ed. R. W. Argyle, P. S. Bunclark, & J. R. Lewis, 505

Telfer, R. C., Zheng, W., Kriss, G. A., & Davidsen, A. F. 2002, ApJ, 565, 773

The Astropy Collaboration, Price-Whelan, A. M., Sipőcz, B. M., et al. 2018, The Astronomical Journal, 156, 123

Thom, C., Tumlinson, J., Werk, J. K., et al. 2012, ApJL, 758, L41

Tinker, J. L., Brownstein, J. R., Guo, H., et al. 2017, ApJ, 839, 121

Tumlinson, J., Peeples, M. S., & Werk, J. K. 2017, ARA&A, 55, 389

Tumlinson, J., Thom, C., Werk, J. K., et al. 2011, Science, 334, 948

—. 2013, ApJ, 777, 59

Velander, M., van Uitert, E., Hoekstra, H., et al. 2014, MNRAS, 437, 2111

Voit, G. M., Bryan, G. L., O'Shea, B. W., & Donahue, M. 2015, ApJL, 808, L30

Voit, G. M., Meece, G., Li, Y., et al. 2017, ApJ, 845, 80

Wechsler, R. H., & Tinker, J. L. 2018, ARA&A, 56, 435

Werk, J. K., Prochaska, J. X., Thom, C., et al. 2012, ApJS, 198, 3

Wiersma, R. P. C., Schaye, J., & Smith, B. D. 2009, MNRAS, 393, 99

Wotta, C. B., Lehner, N., Howk, J. C., et al. 2019, ApJ, 872, 81

Wotta, C. B., Lehner, N., Howk, J. C., O'Meara, J. M., & Prochaska, J. X. 2016, ApJ, 831, 95

Xu, X., Cuesta, A. J., Padmanabhan, N., Eisenstein, D. J., & McBride, C. K. 2013, MNRAS, 431, 2834

Yan, R., & Blanton, M. R. 2012, ApJ, 747, 61

Yoon, J. H., & Putman, M. E. 2013, ApJL, 772, L29

—. 2017, ApJ, 839, 117

Yoon, J. H., Putman, M. E., Thom, C., Chen, H.-W., & Bryan, G. L. 2012, ApJ, 754, 84

Zahedy, F. S., Chen, H.-W., Gauthier, J.-R., & Rauch, M. 2017, MNRAS, 466, 1071

Zahedy, F. S., Chen, H.-W., Johnson, S. D., et al. 2019, MNRAS, 484, 2257

Zhu, G., Ménard, B., Bizyaev, D., et al. 2014, MNRAS, 439, 3139

Table 1. RDR Object Information

LRG Name	z_{LRG}	QSO Target	z_{em}	ρ (kpc)
SDSSJ111508.24+023752.7	0.27797	SDSSJ111507.65+023757.5	0.567	44
SDSSJ111132.33+554712.8	0.46286	SDSSJ111132.18+554726.1	0.766	81
SDSSJ112755.83+115438.3	0.42368	SDSSJ112756.76+115427.1	0.509	102
SDSSJ124307.36+353926.3	0.38966	SDSSJ124307.57+353907.1	0.547	105
SDSSJ095915.54+320418.0	0.53019	SDSSJ095914.84+320357.2	0.564	146
SDSSJ141307.39+091956.7	0.35837	SDSSJ141309.14+092011.2	0.460	154
SDSSJ125859.98+413128.2	0.27903	SDSSJ125901.67+413055.8	0.745	164
SDSSJ125222.93+291327.2	0.59874	SDSSJ125224.99+291321.1	0.823	190
SDSSJ171651.46+302649.0	0.40044	SDSSJ171654.20+302701.4	0.752	207
SDSSJ111436.59+403739.1	0.60975	SDSSJ111438.71+403720.3	0.736	212
SDSSJ110632.58+351012.8	0.47035	SDSSJ110631.05+351051.3	0.485	261
SDSSJ081524.08+273621.2	0.50433	SDSSJ081520.66+273616.9	0.907	288
SDSSJ125101.95+302501.7	0.51323	SDSSJ125100.31+302541.8	0.652	289
SDSSJ122516.86+121750.1	0.29801	SDSSJ122512.93+121835.6	0.411	336
SDSSJ141540.01+163336.4	0.48262	SDSSJ141542.90+163413.7	0.743	345
SDSSJ022612.22+001439.9	0.47304	SDSSJ022614.46+001529.7	0.615	367
SDSSJ075217.92+273835.6	0.58117	SDSSJ075222.91+273823.1	1.056	458
SDSSJ150522.44+294626.2	0.40313	SDSSJ150527.60+294718.3	0.526	473
SDSSJ132457.98+271742.6	0.44784	SDSSJ132503.79+271718.7	0.522	481
SDSSJ104918.08+021814.2	0.51524	SDSSJ104923.24+021806.0	0.749	497
SDSSJ110405.15+314244.1	0.36560	SDSSJ110406.94+314111.4	0.434	500

Table 2. LRG and Absorber Properties

LRG Name	z_{LRG}	ρ	M_r	$\log M_\star$	$\log M_{\mathrm{h}}$	R_{vir}	$\log \mathrm{sSFR}$	$\log N(\mathrm{H\ I})$
SDSSJ111508.24+023752.7	0.27797	44	-22.9	11.3	13.3	516	< -10.98	$[18.00, 19.60]$
SDSSJ111132.33+554712.8	0.46286	81	-23.2	11.4	13.4	535	-10.11 ± 0.13	17.80 ± 0.03
SDSSJ112755.83+115438.3	0.42368	102	-22.5	11.2	13.1	412	< -10.69	$15.87^{+0.05}_{-0.06}$
SDSSJ124307.36+353926.3	0.38966	105	-22.9	11.3	13.2	475	< -9.91	< 13.06
SDSSJ095915.54+320418.0	0.53019	146	-23.2	11.4	13.4	494	< -9.98	< 14.76
SDSSJ141307.39+091956.7	0.35837	154	-23.9	11.7	14.0	875	< -10.16	$13.67^{+0.05}_{-0.06}$
SDSSJ125859.98+413128.2	0.27903	164	-23.5	11.6	13.8	754	< -10.96	13.70 ± 0.05
SDSSJ125222.93+291327.2	0.59874	190	-23.4	11.5	13.5	550	< -10.67	> 15.20
SDSSJ171651.46+302649.0	0.40044	207	-23.2	11.4	13.4	544	< -9.77	16.90 ± 0.20
SDSSJ111436.59+403739.1	0.60975	212	-24.1	11.8	14.0	762	< -10.30	< 13.79
SDSSJ110632.58+351012.8	0.47035	261	-22.8	11.3	13.2	445	< -10.32	< 13.70
SDSSJ081524.08+273621.2	0.50433	288	-23.3	11.4	13.4	531	-9.69 ± 0.17	< 13.81
SDSSJ125101.95+302501.7	0.51323	289	-23.6	11.6	13.7	650	< -10.95	< 14.57
SDSSJ122516.86+121750.1	0.29801	336	-22.7	11.2	13.2	478	< -10.31	< 14.12
SDSSJ141540.01+163336.4	0.48262	345	-23.3	11.4	13.4	529	-10.24 ± 0.13	16.07 ± 0.02
SDSSJ022612.22+001439.9	0.47304	367	-23.3	11.5	13.5	562	-10.16 ± 0.10	$13.97^{+0.11}_{-0.15}$
SDSSJ075217.92+273835.6	0.58117	458	-23.0	11.4	13.3	473	< -10.23	< 14.41
SDSSJ150522.44+294626.2	0.40313	473	-22.4	11.2	13.0	386	-10.28 ± 0.17	< 13.85
SDSSJ132457.98+271742.6	0.44784	481	-22.8	11.3	13.2	448	< -9.92	< 14.26
SDSSJ104918.08+021814.2	0.51524	497	-22.4	11.1	12.9	359	< -10.13	$15.72^{+0.19}_{-0.35}$
SDSSJ110405.15+314244.1	0.36560	500	-22.7	11.2	13.2	449	< -9.87	$13.58^{+0.08}_{-0.10}$

Table 3. QSO UV Spectroscopy

QSO Target	Instrument/Grating
SDSSJ111507.65+023757.5	COS/G130M
SDSSJ111132.18+554726.1	COS/G130M,G160M
SDSSJ112756.76+115427.1	COS/G130M,G160M
SDSSJ124307.57+353907.1	COS/G130M,G160M
SDSSJ095914.84+320357.2	COS/G130M
SDSSJ141309.14+092011.2	COS/G130M,G160M
SDSSJ125901.67+413055.8	COS/G130M,G160M
SDSSJ125224.99+291321.1	COS/G130M;FOS/G190H
SDSSJ171654.20+302701.4	COS/G140L
SDSSJ111438.71+403720.3	FOS/G190H
SDSSJ110631.05+351051.3	COS/G160M
SDSSJ081520.66+273616.9	COS/G140L
SDSSJ125100.31+302541.8	COS/G130M
SDSSJ122512.93+121835.6	COS/G130M
SDSSJ141542.90+163413.7	COS/G130M
SDSSJ022614.46+001529.7	COS/G130M,G160M
SDSSJ075222.91+273823.1	COS/G140L
SDSSJ150527.60+294718.3	COS/G130M
SDSSJ132503.79+271718.7	COS/G130M
SDSSJ104923.24+021806.0	COS/G130M,G160M
SDSSJ110406.94+314111.4	COS/G130M,G160M

NOTE—The grating resolutions are as follows: G130M/G160M: $R = 18,000$; G190H: $R = 1,300$; G140L: $R = 2,300$.

Table 4. H I Covering Factors for RDR LRGs

ρ (kpc)	$\langle\rho\rangle$ (kpc)	f_c[a]	95% C.I.	Sightlines[b]	Detections[c]
		$\log N(\mathrm{H\,I}) \geq 15.0$			
$[0, 250]$	140	$0.41^{+0.15}_{-0.14}$	$[0.17, 0.69]$	10	4
$(250, 500]$	390	$0.22^{+0.13}_{-0.10}$	$[0.06, 0.48]$	11	2
		$\log N(\mathrm{H\,I}) \geq 16.0$			
$[0, 250]$	135	$0.35^{+0.15}_{-0.13}$	$[0.12, 0.65]$	9	3
$(250, 500]$	390	$0.14^{+0.11}_{-0.08}$	$[0.02, 0.39]$	11	1
		$\log N(\mathrm{H\,I}) \geq 17.2$			
$[0, 250]$	135	$0.26^{+0.15}_{-0.12}$	$[0.07, 0.56]$	9	2
$(250, 500]$	390	$0.06^{+0.09}_{-0.04}$	$[0.00, 0.27]$	11	0

[a] The error bars on the covering factor represent the 68% confidence interval.

[b] Number of sightlines considered in covering factor calculation.

[c] Number of absorbers detected above the limiting H I value.

Table 5. H I Covering Factors by Sample

$\rho/R_{\rm vir}$	$\langle\rho/R_{\rm vir}\rangle$	f_c[a]	95% C.I.	Sightlines[b]	Detections[c]
		RDR			
$[0.0, 0.5]$	0.25	$0.32^{+0.14}_{-0.12}$	$[0.11, 0.61]$	10	3
$(0.5, 1.0]$	0.68	$0.23^{+0.17}_{-0.12}$	$[0.04, 0.58]$	6	1
$(1.0, 1.5]$	1.20	$0.13^{+0.18}_{-0.10}$	$[0.01, 0.52]$	4	0
		Star-Forming Galaxies			
$[0.0, 0.5]$	0.30	$0.70^{+0.09}_{-0.10}$	$[0.50, 0.86]$	21	15
$(0.5, 1.0]$	0.63	$0.13^{+0.18}_{-0.10}$	$[0.01, 0.52]$	4	0
		Quiescent Galaxies			
$[0.0, 0.5]$	0.21	0.53 ± 0.12	$[0.30, 0.75]$	15	8
$(0.5, 1.0]$	0.57	$0.29^{+0.31}_{-0.21}$	$[0.01, 0.84]$	1	0

NOTE—The limiting H I value for the covering factor calculation is $\log N(\mathrm{H\,I})$ ≥ 16 [cm^{-2}]. The star-forming and quiescent galaxy samples are from the P17 sample.

[a] The error bars on the covering factor represent the 68% confidence interval.

[b] Number of sightlines considered in covering factor calculation.

[c] Number of absorbers detected above the limiting H I value.

Table 6. H I Covering Factors by Stellar Mass

$\rho/R_{\rm vir}$	$\langle\rho/R_{\rm vir}\rangle$	$f_c{}^{\rm a}$	95% C.I.	Sightlines[b]	Detections[c]
		$9.0 \leq \log M_\star < 10.5$			
[0.0, 0.5]	0.30	0.63 ± 0.12	[0.38, 0.84]	14	9
(0.5, 1.0]	0.63	$0.13^{+0.18}_{-0.10}$	[0.01, 0.52]	4	0
		$10.5 \leq \log M_\star < 11.3$			
[0.0, 0.5]	0.24	$0.67^{+0.09}_{-0.10}$	[0.47, 0.84]	22	15
(0.5, 1.0]	0.60	$0.16^{+0.21}_{-0.12}$	[0.01, 0.60]	3	0
(1.0, 1.5]	1.24	$0.16^{+0.21}_{-0.12}$	[0.01, 0.60]	3	0
		$11.3 \leq \log M_\star \leq 12.0$			
[0.0, 0.5]	0.23	$0.41^{+0.12}_{-0.11}$	[0.20, 0.65]	15	6
(0.5, 1.0]	0.68	$0.26^{+0.19}_{-0.14}$	[0.04, 0.64]	5	1
(1.0, 1.5]	1.07	$0.29^{+0.31}_{-0.21}$	[0.01, 0.84]	1	0

NOTE—The limiting H I value for the covering factor calculation is $\log N(\text{H I})$ ≥ 16 [cm^{-2}]. A combination of the RDR LRGs, the galaxies in the P17 sample, and the galaxies in the C18 sample are used for this covering factor calculation. We do not include sightlines in common between the C18 sample and the RDR LRGs or the P17 sample.

[a] The error bars on the covering factor represent the 68% confidence interval.

[b] Number of sightlines considered in covering factor calculation.

[c] Number of absorbers detected above the limiting H I value.

Table 7. H I Covering Factors by Halo Mass

$\rho/R_{\rm vir}$	$\langle\rho/R_{\rm vir}\rangle$	f_c[a]	95% C.I.	Sightlines[b]	Detections[c]
		$11.0 \leq \log M_{\rm h} < 12.0$			
[0.0, 0.5]	0.32	$0.70^{+0.12}_{-0.14}$	[0.43, 0.90]	11	8
(0.5, 1.0]	0.68	$0.16^{+0.21}_{-0.12}$	[0.01, 0.60]	3	0
		$12.0 \leq \log M_{\rm h} < 13.0$			
[0.0, 0.5]	0.25	$0.59^{+0.10}_{-0.11}$	[0.38, 0.78]	20	12
(0.5, 1.0]	0.54	$0.16^{+0.21}_{-0.12}$	[0.01, 0.60]	3	0
(1.0, 1.5]	1.30	$0.21^{+0.25}_{-0.15}$	[0.01, 0.71]	2	0
		$13.0 \leq \log M_{\rm h} \leq 14.0$			
[0.0, 0.5]	0.21	0.50 ± 0.11	[0.30, 0.70]	20	10
(0.5, 1.0]	0.68	$0.23^{+0.17}_{-0.12}$	[0.04, 0.58]	6	1
(1.0, 1.5]	1.09	$0.21^{+0.25}_{-0.15}$	[0.01, 0.71]	2	0

NOTE—The limiting H I value for the covering factor calculation is $\log N(\mathrm{H\,I})$ ≥ 16 [cm^{-2}]. A combination of the RDR LRGs, the galaxies in the P17 sample, and the galaxies in the C18 sample are used for this covering factor calculation. We do not include sightlines in common between the C18 sample and the RDR LRGs or the P17 sample.

[a] The error bars on the covering factor represent the 68% confidence interval.

[b] Number of sightlines considered in covering factor calculation.

[c] Number of absorbers detected above the limiting H I value.

Table 8. Cloudy Grid Parameters

Parameter	Minimum	Maximum	Step Size[a]
$\log N(\text{H I})$ [cm^{-2}]	12.0	20.0	0.25
z	0.0	5.0	0.25
[X/H]	-5.0	$+2.5$	0.25
$\log n_{\text{H}}$ [cm^{-3}]	-4.5	0.0	0.25
[C/α]	-1.0	1.0	0.20

[a]Even though the grid is run using these step sizes, the MCMC sampler interpolates between the grid points.

Table 9. Metallicity Constraints on High H I Column Absorbers

LRG Name	z_{LRG}	ρ	$\log N(\mathrm{H\ I})$	Metallicity[a]	95% C.I.	Metallicity[a]	95% C.I.
		(kpc)		(HM05)	(HM05)	(HM12)	(HM12)
SDSSJ111508.24+023752.7	0.27797	44	$[18.00, 19.60]$	$[-2.10, -0.50]$[b]	$\cdots$	$\cdots$	$\cdots$
SDSSJ111132.33+554712.8	0.46286	81	17.80 ± 0.03	$-0.14^{+0.09}_{-0.10}$	$[-0.32, +0.05]$	-0.06 ± 0.09	$[-0.23, +0.12]$
SDSSJ171651.46+302649.0	0.40044	207	16.90 ± 0.20	$-1.87^{+0.24}_{-0.25}$	$[-2.34, -1.40]$	$-1.36^{+0.33}_{-0.28}$	$[-1.90, -0.44]$
SDSSJ141540.01+163336.4	0.48262	345	16.07 ± 0.02	$-0.89^{+0.08}_{-0.09}$	$[-1.07, -0.72]$	-0.59 ± 0.07	$[-0.72, -0.45]$

[a] The error bars on the median metallicity represent the 68% confidence interval.
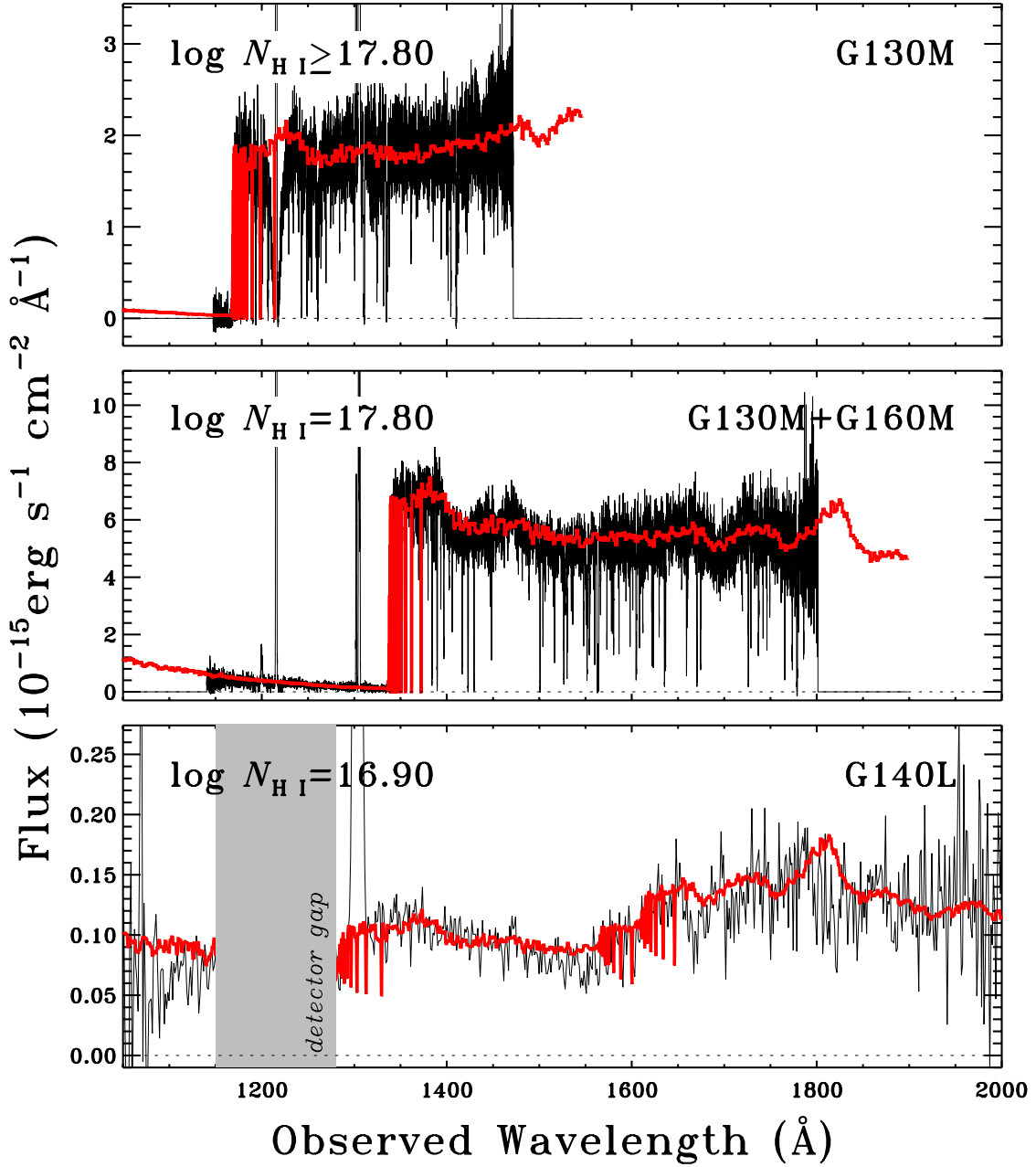
[b] The metallicity for this absorber is determined from [O/H] using $\log N(\mathrm{O\ I})$ from the strongest component and the range of allowed $\log N(\mathrm{H\ I})$ values.

APPENDIX
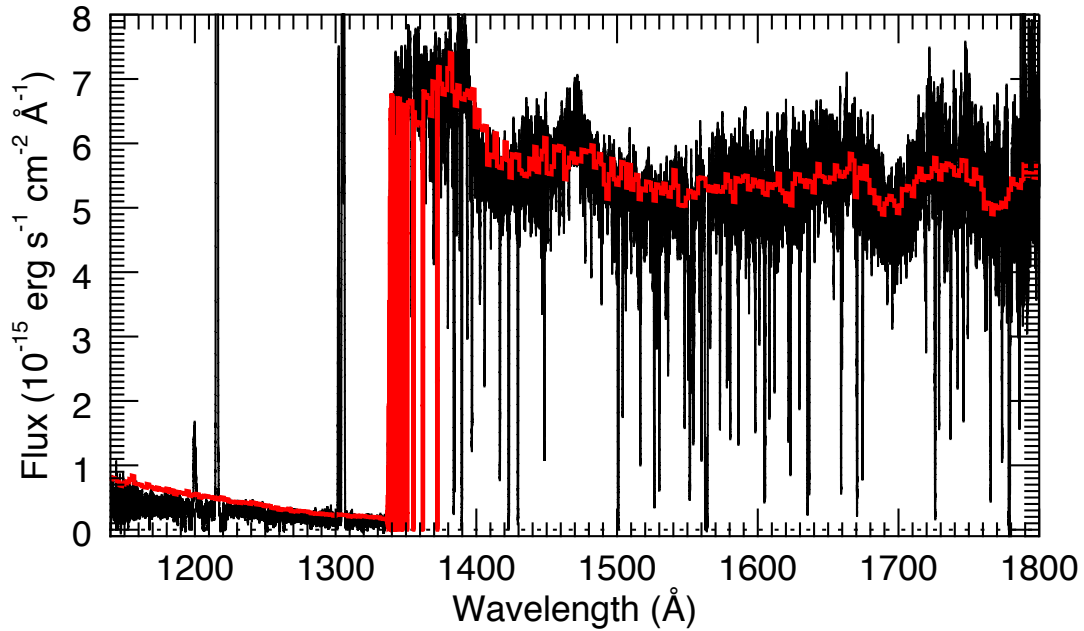
In these appendices, we provide ion information for each sightline and the ion profiles from the QSO spectra, the results of covering factor calculations at the optically-thick absorption limit (log N(H I) $\geq$ 17.2), detailed metallicity results for each absorber , and our metallicity estimate for the low-metallicity absorber reported in C18.

A. SIGHTLINE INFORMATION
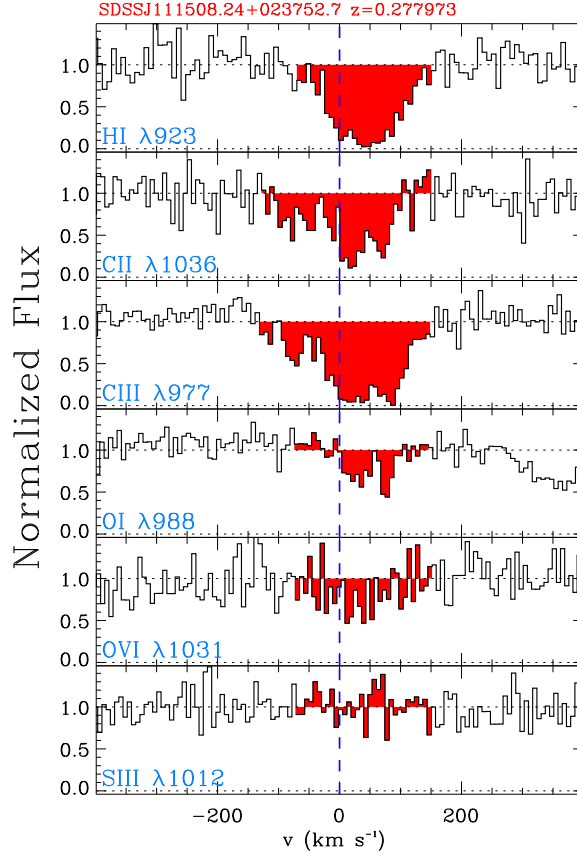
Here we provide the ion information for each sightline. The three spectra for which we fit a break in the QSO spectrum at the Lyman limit to determine log N(H I) are presented in Figure A1, and an example fit of how we determine the error for log N(H I) is presented in Figure A2. The ion profiles for each sightline follow in Figures A3-A23. Table A1 details the integration limits, average velocity, and column density for the ions measured for each sightline.
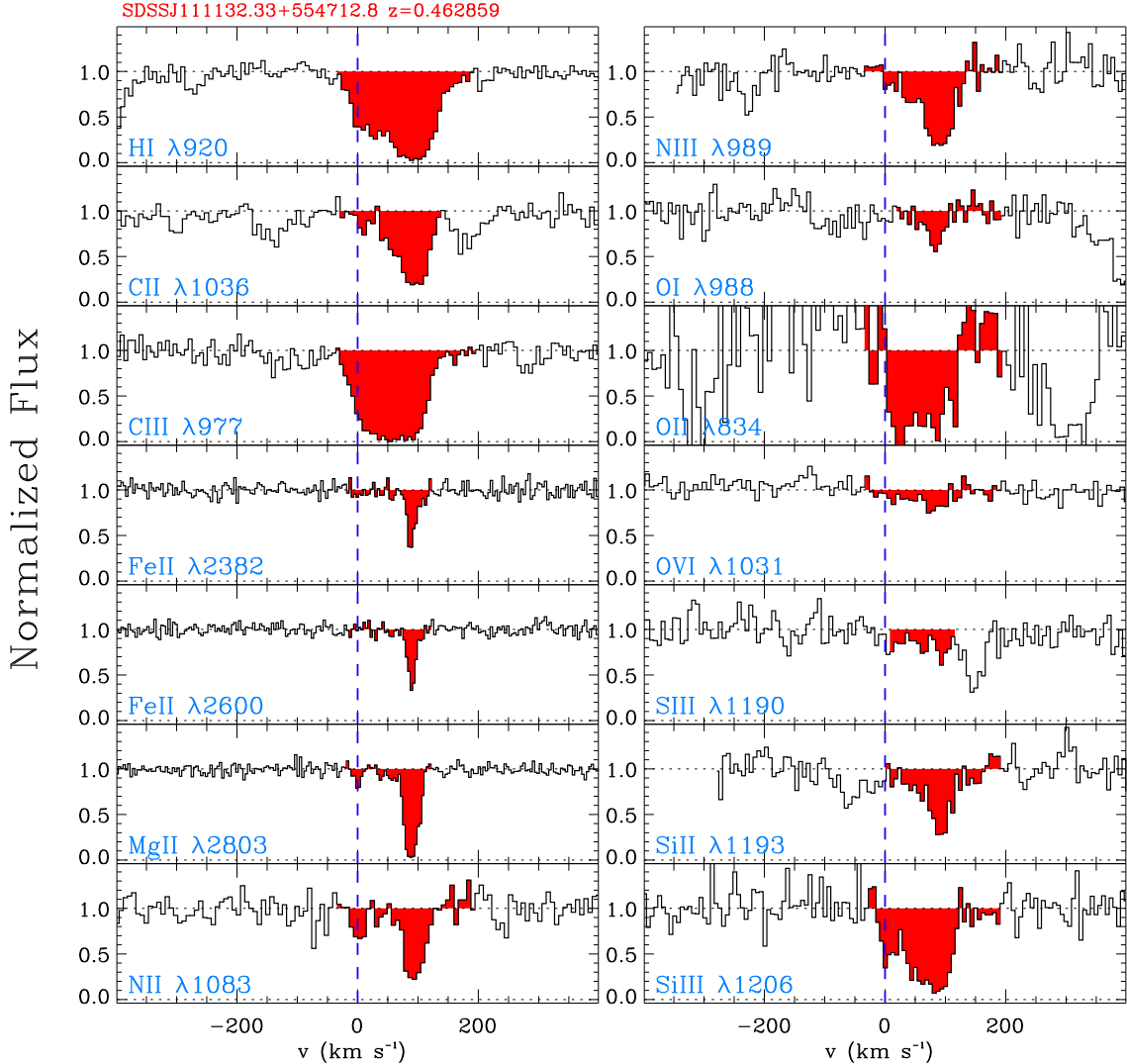
Figure A1. Spectrum of SDSSJ111507.65+023757.5 (top), SDSSJ111132.18+554726.1 (middle), and SDSSJ171654.20+302701.4 (bottom) with Telfer et al. (2002) model overlaid. We calculate a lower limit on the hydrogen column density for the absorber along the SDSSJ111507.65+023757.5 sightline from this method because there is not enough flux recovery blueward of the Lyman limit to get a more accurate measurement. For the SDSSJ171654.20+302701.4 sightline, we show the composite model from three pLLSs in this spectrum as reported in Wotta et al. (2016). The break in the QSO spectrum at the Lyman limit for the absorber associated with an RDR LRG is located at $\lambda \sim 1300$ Å.
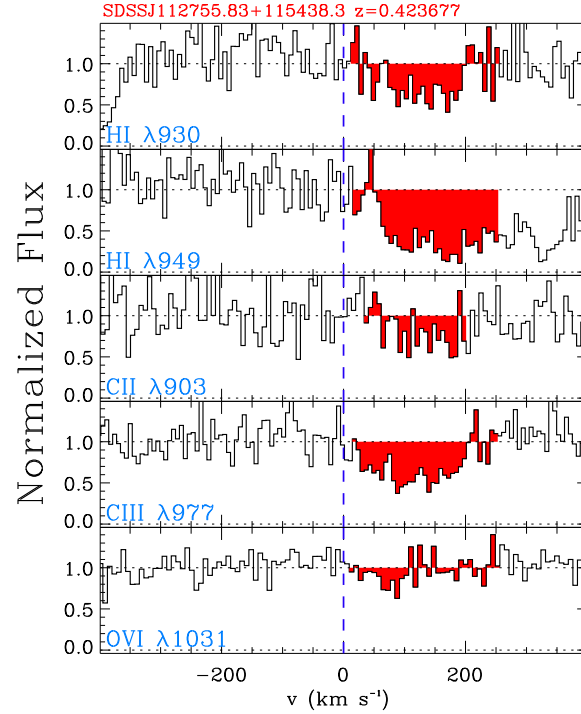
Figure A2. Spectrum of SDSSJ111132.18+554726.1 with Telfer et al. (2002) model overlaid. In the flux recovery section of the QSO spectrum, we have decreased the value of $\log N(\mathrm{H\,I})$ for the absorber to the point where the model now rests on top of the spectrum. This $\log N(\mathrm{H\,I})$ value is taken to be the 2σ value.

BERG ET AL.
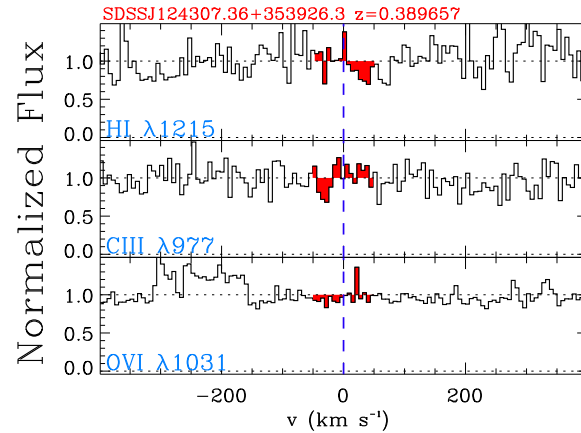
Figure A3. Ion profiles for absorption associated with LRG SDSSJ111508.24+023752.7 at an impact parameter of $\rho = 44$ kpc. The profiles are shown in the reference frame of the LRG, and the red shading shows the section of the spectrum integrated to determine the ion column density.

Figure A4. Same as Figure A3, but for absorption associated with LRG SDSSJ111132.33+554712.8 at an impact parameter of $\rho = 81$ kpc. The weak H I component of this absorber is integrated from -31 to 28 km s^{-1}.

Figure A5. Same as Figure A3, but for absorption associated with LRG SDSSJ112755.83+115438.3 at an impact parameter of $\rho = 102$ kpc.

Figure A6. Same as Figure A3, but for absorption associated with LRG SDSSJ124307.36+353926.3 at an impact parameter of $\rho = 105$ kpc.

Figure A7. Same as Figure A3, but for absorption associated with LRG SDSSJ095915.54+320418.0 at an impact parameter of $\rho = 146$ kpc.

Figure A8. Same as Figure A3, but for absorption associated with LRG SDSSJ141307.39+091956.7 at an impact parameter of $\rho = 154$ kpc.

Figure A9. Same as Figure A3, but for absorption associated with LRG SDSSJ125859.98+413128.2 at an impact parameter of $\rho = 164$ kpc. We report the sum of the two H I components in this paper.
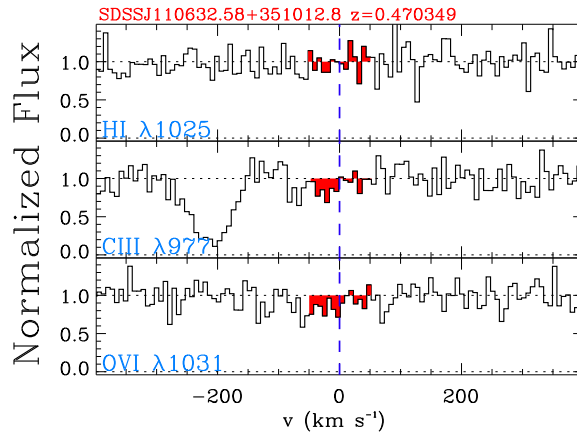
Figure A10. Same as Figure A3, but for absorption associated with LRG SDSSJ125222.93+291327.2 at an impact parameter of $\rho = 190$ kpc.
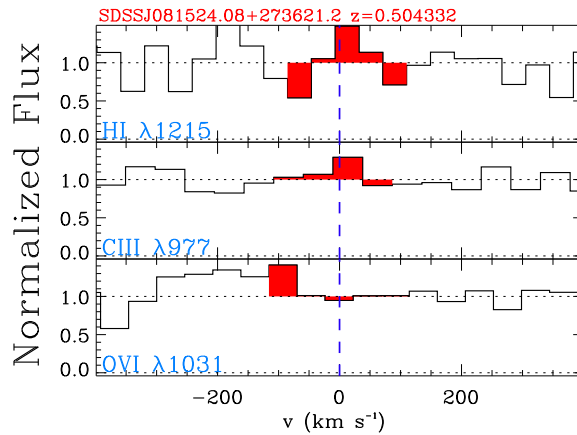
Figure A11. Same as Figure A3, but for absorption associated with LRG SDSSJ171651.46+302649.0 at an impact parameter of $\rho = 207$ kpc.
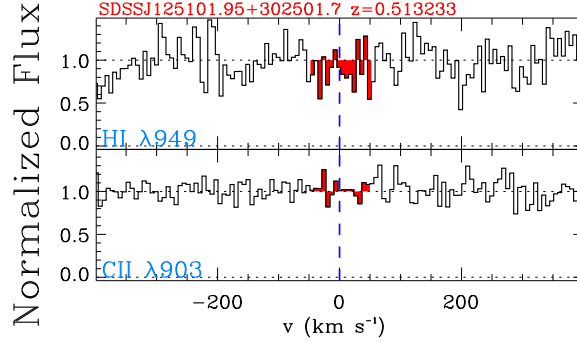
Figure A12. Same as Figure A3, but for absorption associated with LRG SDSSJ111436.59+403739.1 at an impact parameter of $\rho = 212$ kpc.
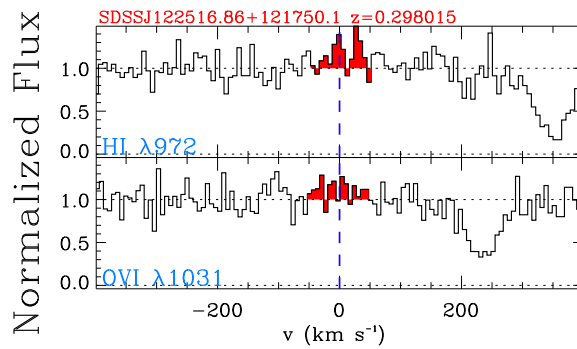
Figure A13. Same as Figure A3, but for absorption associated with LRG SDSSJ110632.58+351012.8 at an impact parameter of $\rho = 261$ kpc.
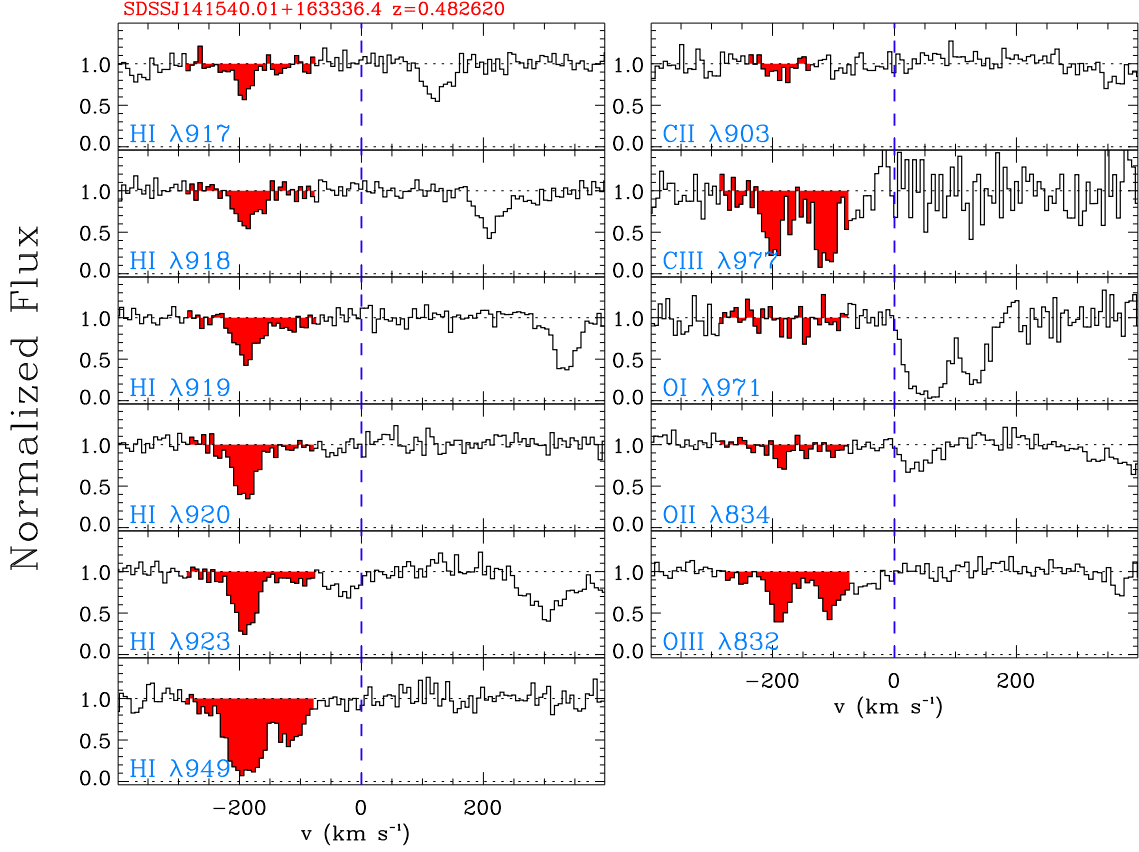
Figure A14. Same as Figure A3, but for absorption associated with LRG SDSSJ081524.08+273621.2 at an impact parameter of $\rho = 288$ kpc.

SDSSJ125101.95+302501.7 z=0.513233

Normalized Flux

1.0

0.5

0.0

HI λ949

1.0

0.5

0.0

CII λ903

−200   0   200

v (km s⁻¹)
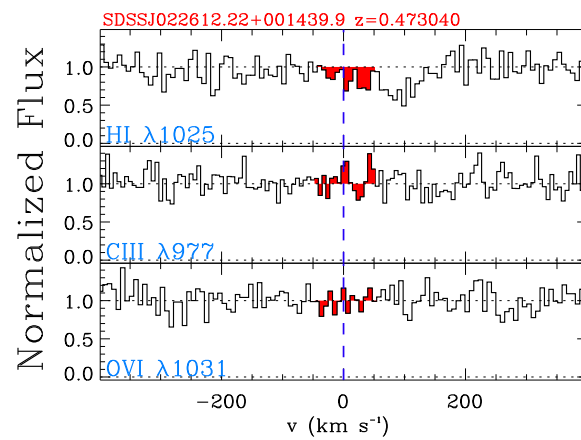
Figure A15. Same as Figure A3, but for absorption associated with LRG SDSSJ125101.95+302501.7 at an impact parameter of $\rho = 289$ kpc.

SDSSJ122516.86+121750.1 z=0.298015

Normalized Flux

1.0

0.5

0.0

HI λ972

1.0

0.5

0.0

OVI λ1031

−200   0   200

v (km s⁻¹)
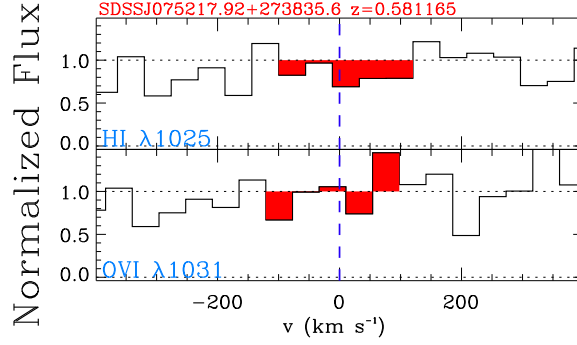
Figure A16. Same as Figure A3, but for absorption associated with LRG SDSSJ122516.86+121750.1 at an impact parameter of $\rho = 336$ kpc.
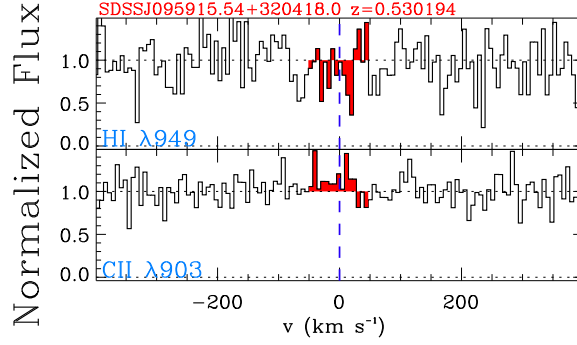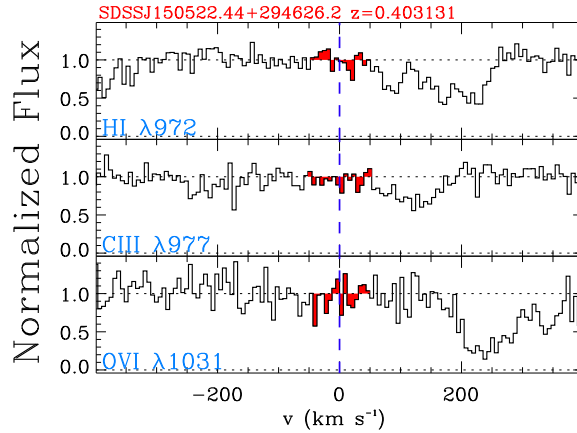
Figure A17. Same as Figure A3, but for absorption associated with LRG SDSSJ141540.01+163336.4 at an impact parameter of $\rho = 345$ kpc. The weak H I component is integrated from -146 to -75 $\mathrm{km\,s^{-1}}$.
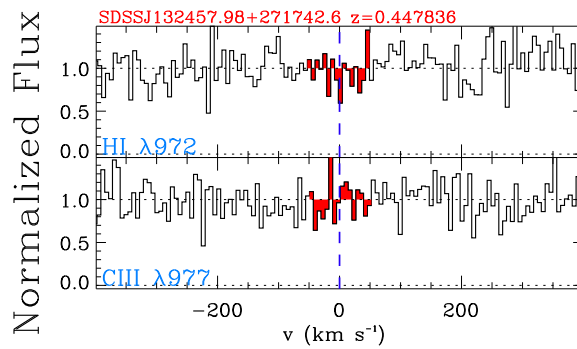
Figure A18. Same as Figure A3, but for absorption associated with LRG SDSSJ022612.22+001439.9 at an impact parameter of $\rho = 367$ kpc.
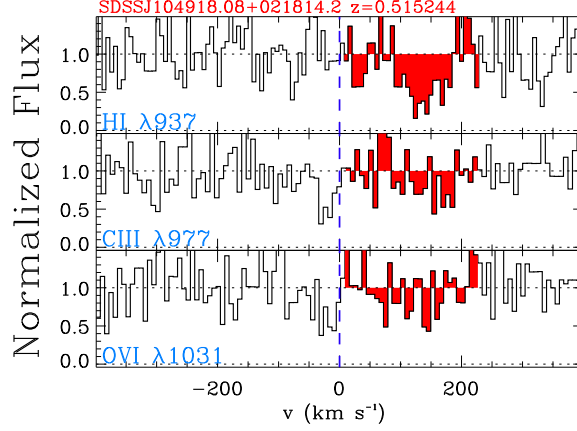
Figure A19. Same as Figure A3, but for absorption associated with LRG SDSSJ075217.92+273835.6 at an impact parameter of $\rho = 458$ kpc.
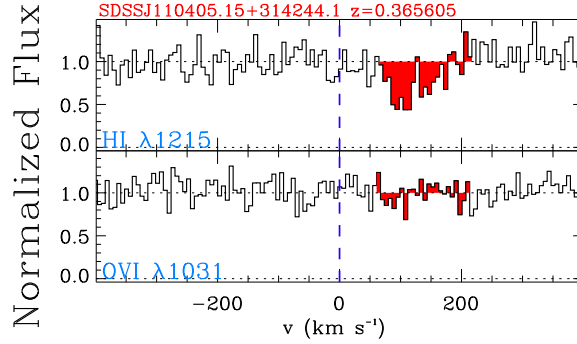
Figure A20. Same as Figure A3, but for absorption associated with LRG SDSSJ150522.44+294626.2 at an impact parameter of $\rho = 473$ kpc.
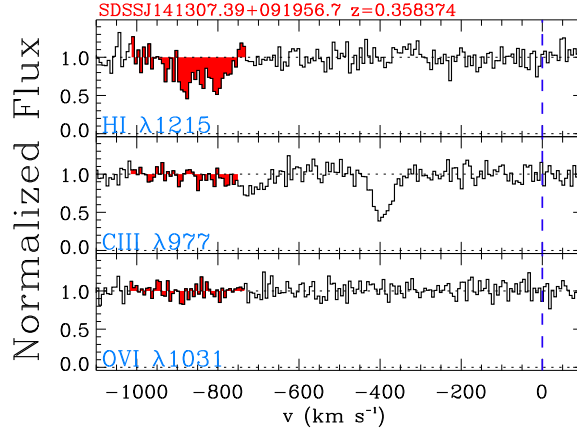

Figure A21. Same as Figure A3, but for absorption associated with LRG SDSSJ132457.98+271742.6 at an impact parameter of $\rho = 481$ kpc.

Figure A22. Same as Figure A3, but for absorption associated with LRG SDSSJ104918.08+021814.2 at an impact parameter of $\rho = 497$ kpc.
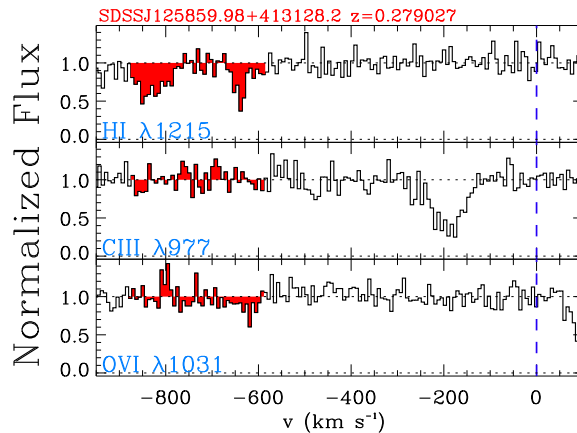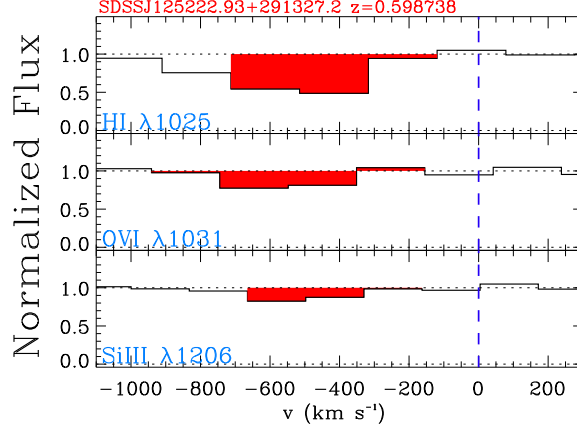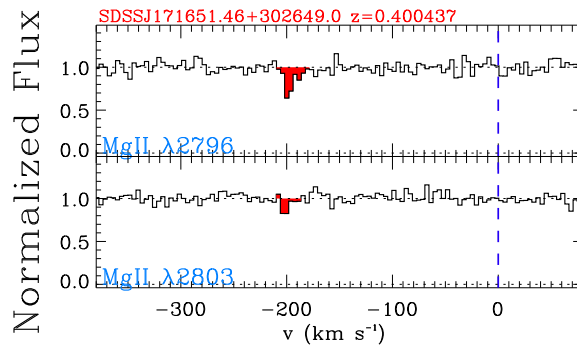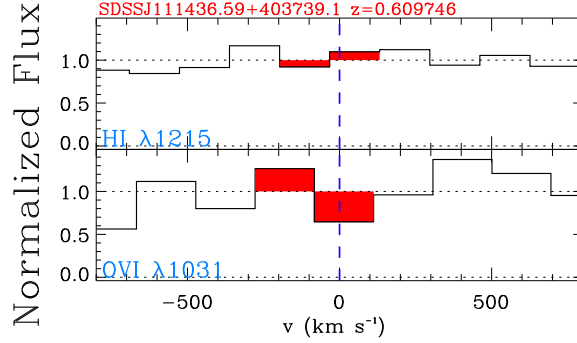

Figure A23. Same as Figure A3, but for absorption associated with LRG SDSSJ110405.15+314244.1 at an impact parameter of $\rho = 500$ kpc.

Table A1. Average velocities and column densities of the hydrogen and metal ions in the absorbers associated with the RDR LRGs

Species	$[v_1, v_2]$	$\langle v \rangle$	$\log N$
	$(\mathrm{km\,s^{-1}})$	$(\mathrm{km\,s^{-1}})$	$[\mathrm{cm^{-2}}]$
SDSSJ111508.24+023752.7, $z = 0.277973$			
C II $\lambda1036$	$[-131, 148]$	12.8 ± 34.1	> 14.75
C III $\lambda977$	$[-131, 148]$	33.7 ± 34.1	> 14.27
Fe II $\lambda1144$	$[-71, 148]$	$\cdots$	< 13.97
Fe III $\lambda1122$	$[-71, 148]$	$\cdots$	< 13.97
H I Break+Voigt	$\cdots$	$\cdots$	$[18.00, 19.60]$
N II $\lambda1083$	$[-71, 148]$	35.6 ± 34.0	14.24 ± 0.08
N III $\lambda989$	$[-71, 148]$	50.3 ± 33.8	14.24 ± 0.06
O I $\lambda971$	$[-71, 118]$	$\cdots$	< 14.60
O I $\lambda988$	$[-71, 148]$	59.5 ± 35.4	14.45 ± 0.11

Table A1 continued

Berg et al.

Table A1 *(continued)*

Species	$[v_1, v_2]$	$\langle v \rangle$	$\log N$
	$(\mathrm{km\,s^{-1}})$	$(\mathrm{km\,s^{-1}})$	$[\mathrm{cm^{-2}}]$
O I		59.5 ± 35.4	14.45 ± 0.11
O VI $\lambda 1037$	$[-71, 148]$	$\cdots$	< 14.07
O VI $\lambda 1031$	$[-71, 148]$	29.3 ± 35.8	14.21 ± 0.15
O VI		29.3 ± 35.8	14.21 ± 0.15
S III $\lambda 1012$	$[-71, 148]$	$\cdots$	< 14.20
S IV $\lambda 1062$	$[-71, 148]$	$\cdots$	< 13.99
SDSSJ111132.33+554712.8, $z = 0.462859$			
C II $\lambda 1036$	$[-31, 138]$	83.4 ± 29.6	> 14.48
C III $\lambda 977$	$[-34, 193]$	57.4 ± 27.7	> 14.27
Fe II $\lambda 2382$	$[-16, 123]$	83.0 ± 27.9	12.98 ± 0.04
Fe II $\lambda 2586$	$[-16, 123]$	91.7 ± 30.0	13.06 ± 0.11
Fe II $\lambda 2600$	$[-16, 123]$	87.2 ± 27.8	13.00 ± 0.03
Fe II		87.1 ± 16.5	13.00 ± 0.02
H I Break	$\cdots$	$\cdots$	17.80 ± 0.03
Mg II $\lambda 2796$	$[-16, 123]$	84.3 ± 27.6	13.34 ± 0.05
Mg II $\lambda 2803$	$[-16, 123]$	84.5 ± 27.6	13.52 ± 0.04
Mg II		84.5 ± 27.6	> 13.67
N I $\lambda 1199$	$[-31, 193]$	$\cdots$	< 13.47
N II $\lambda 1083$	$[-31, 193]$	73.2 ± 28.6	> 14.31
N III $\lambda 989$	$[-31, 193]$	80.3 ± 28.0	> 14.48
O I $\lambda 971$	$[-31, 173]$	$\cdots$	< 14.31
O I $\lambda 988$	$[18, 193]$	79.5 ± 30.6	14.23 ± 0.13
O I		79.5 ± 30.6	14.23 ± 0.13
O II $\lambda 834$	$[-31, 193]$	52.2 ± 37.7	> 14.61
O IV $\lambda 787$	$[-31, 193]$	$\cdots$	< 14.52
O VI $\lambda 1031$	$[-31, 193]$	67.6 ± 30.4	13.70 ± 0.10
O VI $\lambda 1037$	$[-31, 193]$	69.2 ± 36.0	13.74 ± 0.20
O VI		68.2 ± 23.2	13.71 ± 0.09
S III $\lambda 1012$	$[-31, 193]$	85.5 ± 28.8	14.34 ± 0.06
S IV $\lambda 809$	$[-31, 193]$	$\cdots$	< 14.28
S VI $\lambda 933$	$[-31, 193]$	$\cdots$	< 12.70
S III $\lambda 1190$	$[11, 113]$	67.4 ± 28.2	14.48 ± 0.09
Si II $\lambda 1193$	$[3, 193]$	83.1 ± 28.1	> 13.51
Si III $\lambda 1206$	$[-31, 193]$	70.1 ± 27.9	> 13.54
SDSSJ112755.83+115438.3, $z = 0.423677$			
C II $\lambda 903$	$[32, 202]$	141.6 ± 31.7	14.11 ± 0.15

Table A1 continued

Table A1 *(continued)*

Species	$[v_1, v_2]$	$\langle v \rangle$	$\log N$
	$(\mathrm{km\,s^{-1}})$	$(\mathrm{km\,s^{-1}})$	$[\mathrm{cm^{-2}}]$
C III $\lambda 977$	$[12, 252]$	115.0 ± 29.6	13.73 ± 0.05
Fe II $\lambda 1144$	$[12, 252]$	$\cdots$	< 13.94
Fe III $\lambda 1122$	$[12, 252]$	$\cdots$	< 14.18
H I $\lambda 930$	$[12, 252]$	130.8 ± 31.7	15.88 ± 0.11
H I $\lambda 949$	$[12, 252]$	156.3 ± 29.9	15.87 ± 0.08
H I		144.3 ± 21.7	15.87 ± 0.06
N II $\lambda 1083$	$[12, 252]$	$\cdots$	< 13.58
O I $\lambda 1039$	$[12, 252]$	$\cdots$	< 14.67
O II $\lambda 834$	$[12, 252]$	$\cdots$	< 14.08
O VI $\lambda 1031$	$[12, 252]$	$\cdots$	< 13.49
S III $\lambda 1012$	$[12, 252]$	$\cdots$	< 13.94
S IV $\lambda 1062$	$[12, 252]$	$\cdots$	< 13.97
S VI $\lambda 944$	$[12, 252]$	$\cdots$	< 13.59
S III $\lambda 1190$	$[12, 252]$	$\cdots$	< 14.60
Si II $\lambda 1193$	$[12, 252]$	$\cdots$	< 13.24
Si III $\lambda 1206$	$[12, 252]$	$\cdots$	< 12.78
SDSSJ124307.36+353926.3, $z = 0.389657$			
C II $\lambda 903$	$[-50, 50]$	$\cdots$	< 12.94
C III $\lambda 977$	$[-50, 50]$	$\cdots$	< 12.65
Fe II $\lambda 1144$	$[-50, 50]$	$\cdots$	< 13.45
Fe III $\lambda 1122$	$[-50, 50]$	$\cdots$	< 13.92
H I $\lambda 1215$	$[-50, 50]$	$\cdots$	< 13.06
Mg II $\lambda 1239$	$[-50, 50]$	$\cdots$	< 15.91
N II $\lambda 1083$	$[-50, 50]$	$\cdots$	< 13.41
N III $\lambda 989$	$[-50, 50]$	$\cdots$	< 13.72
N V $\lambda 1238$	$[-50, 50]$	$\cdots$	< 13.56
O I $\lambda 988$	$[-50, 50]$	$\cdots$	< 13.86
O II $\lambda 834$	$[-50, 50]$	$\cdots$	< 13.73
O VI $\lambda 1031$	$[-50, 50]$	$\cdots$	< 13.24
S II $\lambda 1259$	$[-50, 50]$	$\cdots$	< 14.69
S III $\lambda 1012$	$[-50, 50]$	$\cdots$	< 13.61
S IV $\lambda 1062$	$[-50, 50]$	$\cdots$	< 13.79
S VI $\lambda 933$	$[-50, 50]$	$\cdots$	< 12.85
S III $\lambda 1190$	$[-50, 50]$	$\cdots$	< 14.23
Si II $\lambda 1260$	$[-50, 50]$	$\cdots$	< 12.88
Si III $\lambda 1206$	$[-50, 50]$	$\cdots$	< 12.47

Table A1 continued

Table A1 *(continued)*

Species	$[v_1, v_2]$	$\langle v \rangle$	$\log N$
	$(\mathrm{km\,s^{-1}})$	$(\mathrm{km\,s^{-1}})$	$[\mathrm{cm^{-2}}]$
SDSSJ095915.54+320418.0, $z = 0.530194$			
C II $\lambda903$	$[-50, 50]$	$\cdots$	< 13.19
H I $\lambda949$	$[-50, 50]$	$\cdots$	< 14.76
N III $\lambda763$	$[-50, 50]$	$\cdots$	< 14.11
N IV $\lambda765$	$[-50, 50]$	$\cdots$	< 13.21
Ne VIII $\lambda770$	$[-50, 50]$	$\cdots$	< 13.78
O I $\lambda948$	$[-50, 50]$	$\cdots$	< 15.11
O II $\lambda834$	$[-50, 50]$	$\cdots$	< 13.53
O III $\lambda832$	$[-50, 50]$	$\cdots$	< 13.61
O IV $\lambda787$	$[-50, 50]$	$\cdots$	< 13.66
S IV $\lambda809$	$[-50, 50]$	$\cdots$	< 13.63
S V $\lambda786$	$[-50, 50]$	$\cdots$	< 12.55
S VI $\lambda933$	$[-50, 50]$	$\cdots$	< 13.09
SDSSJ141307.39+091956.7, $z = 0.358374$			
C II $\lambda903$	$[-893, -733]$	$\cdots$	< 12.87
C III $\lambda977$	$[-1013, -753]$	$\cdots$	< 12.61
Fe II $\lambda1133$	$[-1013, -733]$	$\cdots$	< 14.77
H I $\lambda1025$	$[-1013, -733]$	$\cdots$	< 13.61
H I $\lambda1215$	$[-1013, -733]$	-847.1 ± 21.5	13.67 ± 0.06
H I		-847.1 ± 21.5	13.67 ± 0.06
N I $\lambda1199$	$[-933, -773]$	$\cdots$	< 13.31
N V $\lambda1238$	$[-1013, -733]$	$\cdots$	< 13.47
O I $\lambda988$	$[-1013, -733]$	$\cdots$	< 13.83
O VI $\lambda1031$	$[-1013, -733]$	$\cdots$	< 13.41
S II $\lambda1259$	$[-943, -733]$	$\cdots$	< 14.35
S III $\lambda1012$	$[-1013, -733]$	$\cdots$	< 13.84
S VI $\lambda933$	$[-1013, -733]$	$\cdots$	< 12.88
S III $\lambda1190$	$[-1013, -733]$	$\cdots$	< 14.21
Si II $\lambda1260$	$[-1013, -733]$	$\cdots$	< 12.57
Si III $\lambda1206$	$[-1013, -733]$	$\cdots$	< 12.35
SDSSJ125859.98+413128.2, $z = 0.279027$			
C II $\lambda1036$	$[-878, -587]$	$\cdots$	< 13.59
C III $\lambda977$	$[-878, -587]$	$\cdots$	< 12.83
H I $\lambda1025$	$[-878, -587]$	$\cdots$	< 13.80
H I $\lambda1215$	$[-878, -587]$	-751.8 ± 9.7	13.70 ± 0.05
H I		-751.8 ± 9.7	13.70 ± 0.05

Table A1 continued

Table A1 *(continued)*

Species	$[v_1, v_2]$	$\langle v \rangle$	$\log N$
	$(\mathrm{km\,s^{-1}})$	$(\mathrm{km\,s^{-1}})$	$[\mathrm{cm^{-2}}]$
N II $\lambda 1083$	$[-878, -587]$	$\cdots$	< 13.62
N III $\lambda 989$	$[-878, -587]$	$\cdots$	< 13.62
N V $\lambda 1238$	$[-878, -587]$	$\cdots$	< 13.69
O I $\lambda 1302$	$[-878, -587]$	$\cdots$	< 14.03
O VI $\lambda 1031$	$[-878, -587]$	$\cdots$	< 13.53
S II $\lambda 1250$	$[-878, -587]$	$\cdots$	< 15.13
S VI $\lambda 944$	$[-878, -587]$	$\cdots$	< 13.47
S III $\lambda 1190$	$[-878, -587]$	$\cdots$	< 14.13
Si II $\lambda 1193$	$[-878, -587]$	$\cdots$	< 12.75
SDSSJ125222.93+291327.2, $z = 0.598738$			
C II $\lambda 903$	$[-569, -469]$	$\cdots$	< 13.38
Fe II $\lambda 1144$	$[-739, -189]$	$\cdots$	< 13.96
Fe III $\lambda 1122$	$[-739, -189]$	$\cdots$	< 14.09
H I $\lambda 1025$	$[-739, -189]$	-498.4 ± 50.2	> 15.20
N II $\lambda 1083$	$[-739, -189]$	$\cdots$	< 13.92
N V $\lambda 1242$	$[-739, -189]$	$\cdots$	< 13.87
O I $\lambda 1355$	$[-739, -189]$	$\cdots$	< 18.49
O II $\lambda 834$	$[-569, -469]$	$\cdots$	< 13.62
O III $\lambda 832$	$[-569, -469]$	$\cdots$	< 13.73
O VI $\lambda 1037$	$[-919, -189]$	$\cdots$	< 14.63
O VI $\lambda 1031$	$[-919, -189]$	-569.9 ± 87.3	$14.41^{+0.16}_{-0.25}$
O VI		-569.9 ± 87.3	$14.41^{+0.16}_{-0.25}$
S II $\lambda 1259$	$[-739, -189]$	$\cdots$	< 14.55
S III $\lambda 1012$	$[-739, -189]$	$\cdots$	< 15.08
S IV $\lambda 1062$	$[-739, -189]$	$\cdots$	< 14.29
Si II $\lambda 1260$	$[-739, -189]$	$\cdots$	< 12.67
Si III $\lambda 1206$	$[-739, -189]$	-515.3 ± 53.1	$(>)13.09 :$
Si IV $\lambda 1393$	$[-739, -189]$	$\cdots$	< 13.11
SDSSJ171651.46+302649.0, $z = 0.400437$			
Fe II $\lambda 2382$	$[-210, -177]$	$\cdots$	< 11.91
H I Break	$\cdots$	$\cdots$	16.90 ± 0.20
Mg II $\lambda 2796$	$[-210, -177]$	-196.1 ± 18.7	12.01 ± 0.08
Mg II $\lambda 2803$	$[-209, -185]$	-200.3 ± 18.9	11.85 ± 0.19
Mg II		-198.2 ± 13.3	11.94 ± 0.09
SDSSJ111436.59+403739.1, $z = 0.609746$			
C II $\lambda 1036$	$[-200, 200]$	$\cdots$	< 14.61

Table A1 continued

Table A1 *(continued)*

Species	$[v_1, v_2]$	$\langle v \rangle$	$\log N$
	$(\mathrm{km\,s^{-1}})$	$(\mathrm{km\,s^{-1}})$	$[\mathrm{cm^{-2}}]$
Fe II $\lambda 1608$	$[-200, 200]$	$\cdots$	< 14.12
Fe III $\lambda 1122$	$[-200, 200]$	$\cdots$	< 14.58
H I $\lambda 1215$	$[-200, 200]$	$\cdots$	< 13.79
N II $\lambda 1083$	$[-200, 200]$	$\cdots$	< 14.36
N V $\lambda 1242$	$[-200, 200]$	$\cdots$	< 14.32
O I $\lambda 1302$	$[-200, 200]$	$\cdots$	< 14.19
O VI $\lambda 1031$	$[-200, 200]$	$\cdots$	< 14.63
S II $\lambda 1259$	$[-200, 200]$	$\cdots$	< 14.99
S III $\lambda 1012$	$[-200, 200]$	$\cdots$	< 15.51
S IV $\lambda 1062$	$[-200, 200]$	$\cdots$	< 14.81
S III $\lambda 1190$	$[-200, 200]$	$\cdots$	< 14.94
Si II $\lambda 1260$	$[-200, 200]$	$\cdots$	< 13.09
Si III $\lambda 1206$	$[-200, 200]$	$\cdots$	< 13.07
Si IV $\lambda 1393$	$[-200, 200]$	$\cdots$	< 13.44
SDSSJ110632.58+351012.8, $z = 0.470349$			
C II $\lambda 1036$	$[-50, 50]$	$\cdots$	< 13.46
C III $\lambda 977$	$[-50, 50]$	$\cdots$	< 12.72
Fe II $\lambda 1144$	$[-50, 50]$	$\cdots$	< 13.97
Fe III $\lambda 1122$	$[-50, 50]$	$\cdots$	< 14.13
H I $\lambda 1025$	$[-50, 50]$	$\cdots$	< 13.70
N I $\lambda 1134$	$[-20, 20]$	$\cdots$	< 14.01
N II $\lambda 1083$	$[-50, 50]$	$\cdots$	< 13.68
O I $\lambda 971$	$[-50, 50]$	$\cdots$	< 14.54
O VI $\lambda 1031$	$[-50, 50]$	$\cdots$	< 13.65
S III $\lambda 1012$	$[-50, 50]$	$\cdots$	< 13.97
S VI $\lambda 944$	$[-50, 50]$	$\cdots$	< 13.44
S III $\lambda 1190$	$[-50, 50]$	$\cdots$	< 14.73
Si II $\lambda 1190$	$[-50, 50]$	$\cdots$	< 13.73
SDSSJ081524.08+273621.2, $z = 0.504332$			
C II $\lambda 903$	$[-50, 50]$	$\cdots$	< 13.37
C III $\lambda 977$	$[-100, 100]$	$\cdots$	< 13.25
C IV $\lambda 1548$	$[-100, 100]$	$\cdots$	< 14.56
Fe II $\lambda 1144$	$[-100, 100]$	$\cdots$	< 14.42
Fe III $\lambda 1122$	$[-100, 100]$	$\cdots$	< 14.58
H I $\lambda 1215$	$[-100, 100]$	$\cdots$	< 13.81
N I $\lambda 1199$	$[-60, 60]$	$\cdots$	< 14.16

Table A1 continued

Table A1 *(continued)*

Species	$[v_1, v_2]$	$\langle v \rangle$	$\log N$
	$(\mathrm{km\,s^{-1}})$	$(\mathrm{km\,s^{-1}})$	$[\mathrm{cm^{-2}}]$
N II $\lambda1083$	$[-100, 100]$	$\cdots$	< 14.26
N III $\lambda989$	$[-100, 100]$	$\cdots$	< 14.01
N V $\lambda1238$	$[-100, 100]$	$\cdots$	< 14.25
O I $\lambda988$	$[-100, 100]$	$\cdots$	< 14.43
O III $\lambda702$	$[-100, 100]$	$\cdots$	< 15.12
O VI $\lambda1031$	$[-100, 100]$	$\cdots$	< 14.08
S II $\lambda1259$	$[-100, 100]$	$\cdots$	< 15.26
S III $\lambda677$	$[-100, 100]$	$\cdots$	< 14.12
S IV $\lambda744$	$[-100, 100]$	$\cdots$	< 14.04
S VI $\lambda933$	$[-100, 100]$	$\cdots$	< 13.46
S III $\lambda1190$	$[-100, 100]$	$\cdots$	< 14.97
Si II $\lambda1260$	$[-100, 100]$	$\cdots$	< 13.40
Si III $\lambda1206$	$[-100, 100]$	$\cdots$	< 13.22
Si IV $\lambda1393$	$[-100, 100]$	$\cdots$	< 14.90
SDSSJ125101.95+302501.7, $z = 0.513233$			
C II $\lambda903$	$[-50, 50]$	$\cdots$	< 12.98
H I $\lambda949$	$[-50, 50]$	$\cdots$	< 14.57
N IV $\lambda765$	$[-50, 50]$	$\cdots$	< 12.83
O I $\lambda936$	$[-50, 50]$	$\cdots$	< 14.98
O II $\lambda834$	$[-50, 50]$	$\cdots$	< 13.28
O IV $\lambda787$	$[-50, 50]$	$\cdots$	< 13.53
SDSSJ122516.86+121750.1, $z = 0.298015$			
C II $\lambda903$	$[-50, 50]$	$\cdots$	< 13.20
H I $\lambda972$	$[-50, 50]$	$\cdots$	< 14.12
N II $\lambda1083$	$[-50, 50]$	$\cdots$	< 13.50
O I $\lambda988$	$[-50, 50]$	$\cdots$	< 14.05
O VI $\lambda1031$	$[-50, 50]$	$\cdots$	< 13.46
S III $\lambda1012$	$[-50, 50]$	$\cdots$	< 13.93
S VI $\lambda933$	$[-50, 50]$	$\cdots$	< 13.18
Si II $\lambda1020$	$[-50, 50]$	$\cdots$	< 14.34
SDSSJ141540.01+163336.4, $z = 0.482620$			
C II $\lambda903$	$[-235, -135]$	$\cdots$	< 13.03
C II $\lambda903$	$[-235, -135]$	-183.0 ± 26.2	$12.89^{+0.13}_{-0.19}$
C II		-183.0 ± 26.2	$12.89^{+0.13}_{-0.19}$
C III $\lambda977$	$[-285, -75]$	-149.3 ± 25.4	> 13.85
H I $\lambda917$	$[-285, -75]$	-182.8 ± 26.0	16.06 ± 0.08

Table A1 continued

Table A1 *(continued)*

Species	$[v_1, v_2]$	$\langle v \rangle$	$\log N$
	$(\mathrm{km\,s^{-1}})$	$(\mathrm{km\,s^{-1}})$	$[\mathrm{cm^{-2}}]$
H I λ918	$[-285, -75]$	-181.9 ± 25.3	16.06 ± 0.06
H I λ919	$[-285, -75]$	-173.8 ± 24.7	16.13 ± 0.04
H I λ920	$[-285, -75]$	-183.0 ± 24.6	16.05 ± 0.04
H I λ923	$[-285, -75]$	-182.6 ± 24.4	16.05 ± 0.03
H I		-180.8 ± 11.2	16.07 ± 0.02
O I λ971	$[-285, -75]$	$\cdots$	< 14.56
O II λ834	$[-285, -75]$	-159.4 ± 28.7	13.68 ± 0.13
O III λ832	$[-285, -75]$	-156.7 ± 24.5	14.44 ± 0.03
S V λ786	$[-285, -75]$	$\cdots$	< 12.44
S VI λ933	$[-285, -75]$	$\cdots$	< 12.80
SDSSJ022612.22+001439.9, $z = 0.473040$			
C II λ903	$[-45, 54]$	$\cdots$	< 12.97
C III λ977	$[-45, 54]$	$\cdots$	< 12.67
H I λ972	$[-45, 54]$	$\cdots$	< 14.08
H I λ1025	$[-45, 54]$	9.8 ± 17.8	13.97 ± 0.15
H I		9.8 ± 17.8	13.97 ± 0.15
N II λ1083	$[-45, 54]$	$\cdots$	< 13.75
N III λ989	$[-45, 54]$	$\cdots$	< 13.44
O I λ988	$[-45, 54]$	$\cdots$	< 13.86
O II λ834	$[-45, 54]$	$\cdots$	< 13.33
O IV λ787	$[-45, 54]$	$\cdots$	< 13.88
O VI λ1031	$[-45, 54]$	$\cdots$	< 13.42
S III λ1012	$[-45, 54]$	$\cdots$	< 13.94
S IV λ809	$[-45, 54]$	$\cdots$	< 13.58
S V λ786	$[-45, 54]$	$\cdots$	< 12.79
S VI λ933	$[-45, 54]$	$\cdots$	< 12.86
Si II λ1193	$[-45, 54]$	$\cdots$	< 13.04
Si III λ1206	$[-45, 54]$	$\cdots$	< 12.82
SDSSJ075217.92+273835.6, $z = 0.581165$			
C II λ903	$[-50, 50]$	$\cdots$	< 13.46
H I λ1025	$[-100, 100]$	$\cdots$	< 14.41
N II λ1083	$[-100, 100]$	$\cdots$	< 14.42
N III λ989	$[-100, 100]$	$\cdots$	< 14.26
O I λ988	$[-100, 100]$	$\cdots$	< 14.64
O II λ834	$[-100, 100]$	$\cdots$	< 14.09
O III λ832	$[-100, 100]$	$\cdots$	< 14.16

Table A1 continued

Table A1 *(continued)*

Species	$[v_1, v_2]$	$\langle v \rangle$	$\log N$
	$(\mathrm{km\,s^{-1}})$	$(\mathrm{km\,s^{-1}})$	$[\mathrm{cm^{-2}}]$
O VI $\lambda 1031$	$[-100, 100]$	$\cdots$	< 14.26
S III $\lambda 724$	$[-100, 100]$	$\cdots$	< 13.85
S IV $\lambda 1062$	$[-100, 100]$	$\cdots$	< 14.73
S VI $\lambda 933$	$[-100, 100]$	$\cdots$	< 13.65
Si II $\lambda 1020$	$[-100, 100]$	$\cdots$	< 15.10
SDSSJ150522.44+294626.2, $z = 0.403131$			
C II $\lambda 903$	$[-50, 50]$	$\cdots$	< 12.69
C III $\lambda 977$	$[-50, 50]$	$\cdots$	< 12.58
H I $\lambda 972$	$[-50, 50]$	$\cdots$	< 13.85
N III $\lambda 989$	$[-50, 50]$	$\cdots$	< 13.24
O I $\lambda 988$	$[-50, 50]$	$\cdots$	< 13.65
O II $\lambda 834$	$[-50, 50]$	$\cdots$	< 13.30
O III $\lambda 832$	$[-50, 50]$	$\cdots$	< 13.41
O VI $\lambda 1031$	$[-50, 50]$	$\cdots$	< 13.38
S VI $\lambda 933$	$[-50, 50]$	$\cdots$	< 12.74
Si II $\lambda 1020$	$[-50, 50]$	$\cdots$	< 14.13
SDSSJ132457.98+271742.6, $z = 0.447836$			
C III $\lambda 977$	$[-50, 50]$	$\cdots$	< 12.83
H I $\lambda 972$	$[-50, 50]$	$\cdots$	< 14.26
N III $\lambda 989$	$[-50, 50]$	$\cdots$	< 13.73
O I $\lambda 988$	$[-50, 50]$	$\cdots$	< 14.09
O II $\lambda 834$	$[-50, 50]$	$\cdots$	< 13.84
O IV $\lambda 787$	$[-50, 50]$	$\cdots$	< 14.47
S III $\lambda 1012$	$[-50, 50]$	$\cdots$	< 14.30
S IV $\lambda 809$	$[-50, 50]$	$\cdots$	< 14.13
S V $\lambda 786$	$[-50, 50]$	$\cdots$	< 13.31
S VI $\lambda 933$	$[-50, 50]$	$\cdots$	< 13.09
SDSSJ104918.08+021814.2, $z = 0.515244$			
C II $\lambda 903$	$[79, 179]$	$\cdots$	< 13.46
C III $\lambda 977$	$[9, 229]$	$\cdots$	< 13.26
H I $\lambda 926$	$[9, 229]$	$\cdots$	< 15.73
H I $\lambda 937$	$[9, 229]$	120.8 ± 51.6	$15.72^{+0.19}_{-0.35}$
H I		120.8 ± 51.6	$15.72^{+0.19}_{-0.35}$
N II $\lambda 1083$	$[9, 229]$	$\cdots$	< 14.24
N III $\lambda 989$	$[9, 229]$	$\cdots$	< 14.11
N IV $\lambda 765$	$[9, 229]$	$\cdots$	< 13.62

Table A1 continued

BERG ET AL.

Table A1 *(continued)*

Species	$[v_1, v_2]$	$\langle v \rangle$	$\log N$
	$(\mathrm{km\,s^{-1}})$	$(\mathrm{km\,s^{-1}})$	$[\mathrm{cm^{-2}}]$
O I λ971	[9, 229]	⋯	< 15.09
O II λ834	[9, 229]	⋯	< 14.11
O III λ832	[9, 229]	⋯	< 14.22
O VI λ1031	[9, 229]	⋯	< 14.08
S III λ1012	[9, 229]	⋯	< 14.51
S IV λ809	[9, 229]	⋯	< 14.21
S V λ786	[9, 229]	⋯	< 13.26
S VI λ933	[9, 229]	⋯	< 13.58
Si II λ1020	[9, 229]	⋯	< 14.97
SDSSJ110405.15+314244.1, $z = 0.365605$			
C II λ903	[63, 173]	⋯	< 13.31
H I λ1025	[63, 213]	⋯	< 13.65
H I λ1215	[63, 213]	114.1 ± 21.3	13.58 ± 0.10
H I		114.1 ± 21.3	13.58 ± 0.10
N I λ1199	[63, 183]	⋯	< 13.48
N III λ989	[63, 213]	⋯	< 13.47
N V λ1238	[63, 213]	⋯	< 13.45
O I λ988	[63, 213]	⋯	< 13.88
O VI λ1031	[63, 213]	⋯	< 13.45
S II λ1259	[63, 213]	⋯	< 14.33
S III λ1012	[63, 213]	⋯	< 13.94
S IV λ1062	[63, 213]	⋯	< 13.66
S III λ1190	[63, 213]	⋯	< 14.27
Si II λ1193	[63, 213]	⋯	< 12.87

NOTE—$\langle v \rangle$ is the average velocity of the absorption line calculated as the first moment with respect to optical depth. Upper limits (<) are non-detections quoted at the 2σ level. Column densities preceded by > are lower limits owing to saturation in the absorption. If a column density is followed by a : this value is uncertain. For a given atom or ion with more than one transition, we list in the row with no wavelength information the adopted weighted average column densities and velocities. All ions are measured using the AODM unless otherwise labelled. Mg II is not detected in the SDSS spectra for the absorbers with no other ground-based observations.

B. COVERING FACTORS FOR OPTICALLY-THICK ABSORPTION

In this appendix we present the results of the covering factor calculations from § 4 at the optically-thick absorption limit: $\log N(\mathrm{H\,I}) \geq 17.2$. Figures A24-A26 display the covering factors by sample, stellar mass, and halo mass. Tables A2-A4 detail the information about the calculations.

Table A2. H I Covering Factors by Sample at LLS Limit

$\rho/R_{\rm vir}$	$\langle \rho/R_{\rm vir} \rangle$	$f_c{}^{\rm a}$	95% C.I.	Sightlines[b]	Detections[c]
		RDR			
$[0.0, 0.5]$	0.25	$0.24^{+0.14}_{-0.11}$	$[0.06, 0.52]$	10	2
$(0.5, 1.0]$	0.68	$0.09^{+0.14}_{-0.07}$	$[0.00, 0.41]$	6	0
$(1.0, 1.5]$	1.20	$0.13^{+0.18}_{-0.10}$	$[0.01, 0.52]$	4	0
		Star-Forming Galaxies			
$[0.0, 0.5]$	0.30	$0.37^{+0.10}_{-0.09}$	$[0.20, 0.57]$	22	8
$(0.5, 1.0]$	0.64	$0.11^{+0.15}_{-0.08}$	$[0.00, 0.46]$	5	0
		Quiescent Galaxies			
$[0.0, 0.5]$	0.20	$0.27^{+0.11}_{-0.10}$	$[0.10, 0.50]$	16	4
$(0.5, 1.0]$	0.57	$0.29^{+0.31}_{-0.21}$	$[0.01, 0.84]$	1	0

NOTE—The limiting H I value for the covering factor calculation is $\log N(\text{H I}) \geq 17.2\ [\text{cm}^{-2}]$. The star-forming and quiescent galaxy samples are from the P17 sample.

[a] The error bars on the covering factor represent the 68% confidence interval.

[b] Number of sightlines considered in covering factor calculation.

[c] Number of absorbers detected above the limiting H I value.

Table A3. H I Covering Factors by Stellar Mass at LLS Limit

$\rho/R_{\rm vir}$	$\langle\rho/R_{\rm vir}\rangle$	f_c[a]	95% C.I.	Sightlines[b]	Detections[c]
$9.0 \leq \log M_\star < 10.5$					
$[0.0, 0.5]$	0.30	0.37 ± 0.12	$[0.16, 0.62]$	14	5
$(0.5, 1.0]$	0.64	$0.11^{+0.15}_{-0.08}$	$[0.00, 0.46]$	5	0
$10.5 \leq \log M_\star < 11.3$					
$[0.0, 0.5]$	0.24	$0.42^{+0.10}_{-0.09}$	$[0.24, 0.61]$	24	10
$(0.5, 1.0]$	0.60	$0.16^{+0.21}_{-0.12}$	$[0.01, 0.60]$	3	0
$(1.0, 1.5]$	1.24	$0.16^{+0.21}_{-0.12}$	$[0.01, 0.60]$	3	0
$11.3 \leq \log M_\star \leq 12.0$					
$[0.0, 0.5]$	0.23	$0.23^{+0.11}_{-0.09}$	$[0.07, 0.46]$	15	3
$(0.5, 1.0]$	0.68	$0.11^{+0.15}_{-0.08}$	$[0.00, 0.46]$	5	0
$(1.0, 1.5]$	1.07	$0.29^{+0.31}_{-0.21}$	$[0.01, 0.84]$	1	0

NOTE—The limiting H I value for the covering factor calculation is $\log N(\mathrm{H\,I})$ ≥ 17.2 [cm^{-2}]. A combination of the RDR LRGs, the galaxies in the P17 sample, and the galaxies in the C18 sample are used for this covering factor calculation. We do not include sightlines in common between the C18 sample and the RDR LRGs or the P17 sample.

[a] The error bars on the covering factor represent the 68% confidence interval.

[b] Number of sightlines considered in covering factor calculation.

[c] Number of absorbers detected above the limiting H I value.

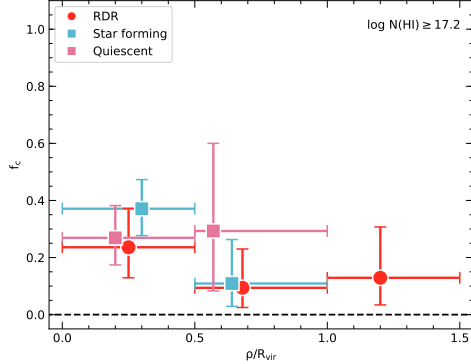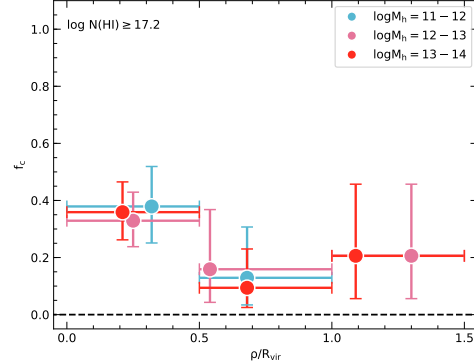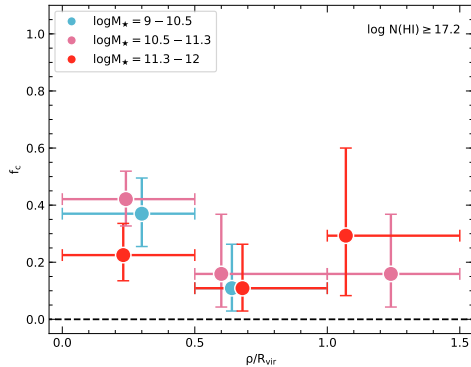**Table A4.** H I Covering Factors by Halo Mass at LLS Limit

$\rho/R_{\rm vir}$	$\langle\rho/R_{\rm vir}\rangle$	f_c[a]	95% C.I.	Sightlines[b]	Detections[c]
		$11.0 \leq \log M_{\rm h} < 12.0$			
[0.0, 0.5]	0.32	$0.38^{+0.14}_{-0.13}$	[0.15, 0.65]	11	4
(0.5, 1.0]	0.68	$0.13^{+0.18}_{-0.10}$	[0.01, 0.52]	4	0
		$12.0 \leq \log M_{\rm h} < 13.0$			
[0.0, 0.5]	0.25	$0.33^{+0.10}_{-0.09}$	[0.16, 0.53]	22	7
(0.5, 1.0]	0.54	$0.16^{+0.21}_{-0.12}$	[0.01, 0.60]	3	0
(1.0, 1.5]	1.30	$0.21^{+0.25}_{-0.15}$	[0.01, 0.71]	2	0
		$13.0 \leq \log M_{\rm h} \leq 14.0$			
[0.0, 0.5]	0.21	$0.36^{+0.11}_{-0.10}$	[0.18, 0.57]	20	7
(0.5, 1.0]	0.68	$0.09^{+0.14}_{-0.07}$	[0.00, 0.41]	6	0
(1.0, 1.5]	1.09	$0.21^{+0.25}_{-0.15}$	[0.01, 0.71]	2	0

NOTE—The limiting H I value for the covering factor calculation is $\log N(\text{H I}) \geq 17.2$ [cm^{-2}]. A combination of the RDR LRGs, the galaxies in the P17 sample, and the galaxies in the C18 sample are used for this covering factor calculation. We do not include sightlines in common between the C18 sample and the RDR LRGs or the P17 sample.

[a] The error bars on the covering factor represent the 68% confidence interval.

[b] Number of sightlines considered in covering factor calculation.

[c] Number of absorbers detected above the limiting H I value.

Berg et al.

Figure A24. H I covering factor distributed by sample for gas with $\log N(\text{H I}) \geq 17.2$ as a function of normalized impact parameter. The vertical error bars show the 68% confidence interval for the covering factor. The horizontal error bars show the extent of each bin, while the location of the data points represents the mean normalized impact parameter. Galaxies from the COS-Halos sample make up the star-forming and quiescent samples (P17). We adopt their characterization of galaxies with $\log \text{sSFR} > -11$ as "star forming."

Figure A26. Halo mass dependence of the H I covering factor ($\log N(\text{H I}) \geq 17.2$) as a function of normalized impact parameter in our combined sample of galaxies incorporating our results with those from P17 and C18. The vertical error bars show the 68% confidence interval in f_c. The horizontal error bars show the extent of each bin, while the location of the data points represents the mean normalized impact parameter. We find no statistically significant difference in the covering factors of galaxies between bins of halo mass.

Figure A25. Stellar mass dependence of the H I covering factor ($\log N(\text{H I}) \geq 17.2$) as a function of normalized impact parameter in our combined sample of galaxies incorporating our results with those from P17 and C18. The vertical error bars show the 68% confidence interval in f_c. The horizontal error bars show the extent of each bin, while the location of the data points represents the mean normalized impact parameter. We find no statistically significant difference in covering factors between mass bins for these column densities.
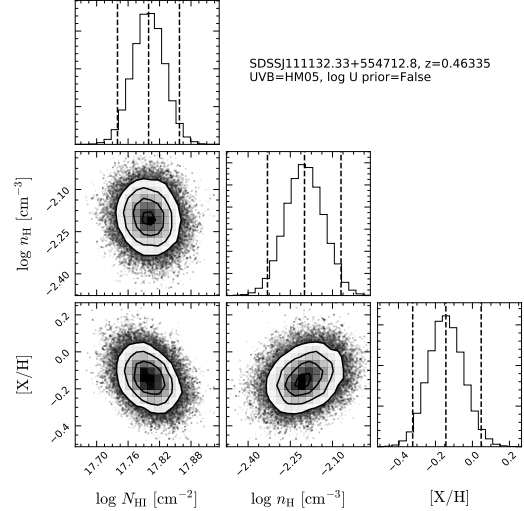
C. METALLICITY RESULTS FOR INDIVIDUAL ABSORBERS

We present the details of our metallicity analysis for each of the four strong H I absorbers along with the corner plots of the Cloudy model grid parameters from our MCMC analysis.

LRG SDSSJ111508.24+023752.7 For this absorber, we estimate $\log N(\text{O I}) = 14.22^{+0.09}_{-0.12}$ in the strongest component that dominates the H I absorption. O I is the best metal proxy for H I since its ionization potential and charge exchange reactions with hydrogen ensure the ionization of H I and O I are strongly coupled. With $\log N(\text{H I}) = [18.00, 19.60]$, this yields a metallicity range for this absorber of $[\text{X/H}] = [-2.10, -0.50]$. It is poorly constrained owing to the poorly constrained $N(\text{H I})$, but it is unlikely to be solar. We note that we also ran an MCMC analysis with a flat prior on the H I column density and used C II, C III, O I, and S III to constrain the metallicity (see Figure A3). The analysis systematically converged to the low metallicity value, i.e., favored a high value of $N(\text{H I})$. We feel that in this case the use of O I to derive the metallicity provides a more conservative range of metallicity.

LRG SDSSJ111132.33+554712.8 The LLS associated with this galaxy exhibits two absorbing components (see Figure A4). We calculate the metallicity of each of the components separately as well as the metallicity implied by the combined components. For the weak H I component, we constrain the metallicity using the ions C II, N II, N III, O I, Si III, and S III. We allow the $[\text{C}/\alpha]$ ratio to vary. There is enough information on this component that applying our Gaussian prior on the $\log U$ distribution is unnecessary. The weak H I component of the LLS has a metallicity $[\text{X/H}] = -0.15^{+0.14}_{-0.21}$. For the strong H I component, we use the ions C II, C III, N I, N II, N III, O I, O II, Si II, Si III, and S III. We do not allow the $[\text{C}/\alpha]$ ratio to vary for this component because this variable is unconstrained when the carbon input ions are lower limits. A Gaussian prior on the $\log U$ distribution of this component is unnecessary. The strong H I component has a metallicity $[\text{X/H}] = -0.20 \pm 0.08$. The similarity in metallicity suggests these components may have a common origin. For the full absorber, we constrain the metallicity using the ions C II, C III, Mg II, N II, N III, O I, O II, Si II, Si III, and S III. We do not allow the $[\text{C}/\alpha]$ ratio to vary for this absorber, nor is a Gaussian prior on the $\log U$ distribution necessary. The corner plot of the MCMC PDFs for this absorber is presented in Figure A27. The implied metallicity of the combined components is $[\text{X/H}] = -0.14^{+0.09}_{-0.10}$.
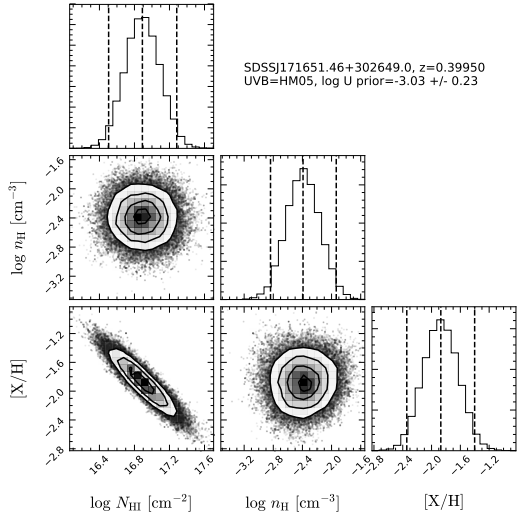
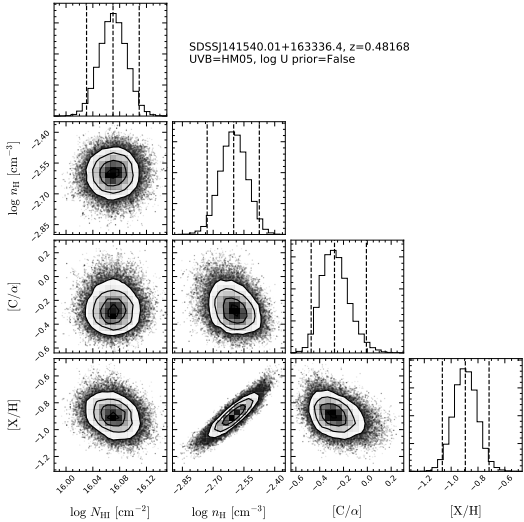*LRG SDSSJ171651.46+302649.0* The pLLS associated with this galaxy has only H I and Mg II column

Figure A27. Corner plot of the MCMC PDFs for the LLS associated with LRG SDSSJ111132.33+554712.8. The PDFs for each variable are plotted along the diagonal, and the other panels are the 2D distributions of the final MCMC walkers chains. The vertical dashed lines show the median value of the distribution and the bounds of the 95% confidence interval.

density measurements (see Figure A11). A Gaussian prior on the $\log U$ distribution of this absorber is necessary to constrain the metallicity (i.e., we use the low-resolution method of Wotta et al. 2016, 2019). The corner plot of the MCMC PDFs for this absorber is presented in Figure A28. The metallicity of this absorber is $[\text{X/H}] = -1.87^{+0.24}_{-0.25}$.

LRG SDSSJ141540.01+163336.4 The pLLS associated with this galaxy exhibits two absorbing components (see Figure A17). We calculate the metallicity of each of the components separately as well as the implied metallicity of the total absorber. For the weak H I component, we constrain the metallicity using the ions C II, C III, O I, O II, and O III. We allow the $[\text{C}/\alpha]$ ratio to vary; a Gaussian prior on the $\log U$ distribution of this component is unnecessary. We find a metallicity of $[\text{X/H}] = -0.50^{+0.26}_{-0.24}$ for the weak H I component. For the strong H I component, we use the ions C II, C III, O I, O II, and O III. We allow the $[\text{C}/\alpha]$ ratio to vary; a Gaussian prior on the $\log U$ distribution of this component is unnecessary. The strong H I component has a metallicity $[\text{X/H}] = -1.02^{+0.11}_{-0.10}$. The weak H I component contributes more to the total C III column density of this absorber than the strong H I component, causing the marginal difference in metallicity. The velocity offset between the two components is modest (~ 75 km s^{-1}). It is not clear if these components should be considered independently or if they are tracing a common struc-

Figure A28. Same as in Fig. A27, but for the pLLS associated with LRG SDSSJ171651.46+302649.0. As this absorber only has an H I and Mg II measurement, we apply a Gaussian $\log U$ constraint.

Figure A29. Same as in Fig. A27, but for the pLLS associated with LRG SDSSJ141540.01+163336.4. We allow the $[\mathrm{C}/\alpha]$ ratio to vary for this absorber.

ture within the CGM. For the full absorber (combining the components), we constrain the metallicity using the ions C II, C III, Mg II, O I, O II, and O III. We allow the $[\mathrm{C}/\alpha]$ ratio to vary; a Gaussian prior on the $\log U$ distribution of this absorber is unnecessary. The corner plot of the MCMC PDFs for this absorber is presented in Figure A29. The implied metallicity of the combined components is $[\mathrm{X/H}] = -0.89^{+0.08}_{-0.09}$.
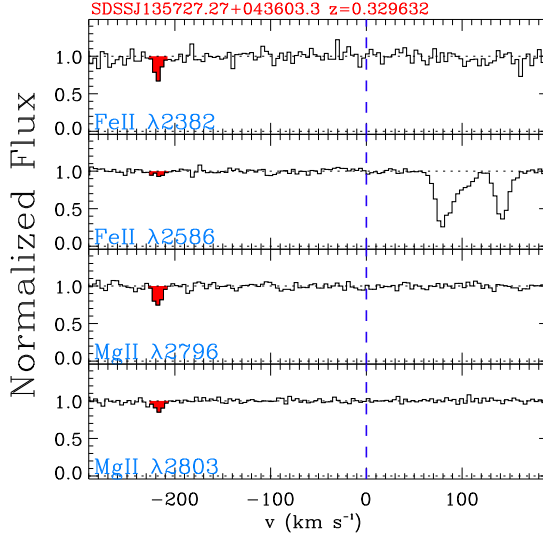
The absorber associated with LRG SDSSJ135726.27+043541.4 has been discussed at length in C18 and is in the CCC sample of Wotta et al. (2019). Both works identify this absorber as a low-metallicity system, and it shows no metal absorption in the available COS data (C18; Lehner et al. 2018). However, it shows absorption in Mg II and Fe II in the Keck/HIRES observations (Lehner et al. 2018).

The Magellan/MIKE observations reported by Chen et al. (2019) were inconclusive regarding the detection of Mg II or Fe II. In order to improve the Mg II and especially Fe II reported in Lehner et al. (2018), we obtained new Keck/HIRES observations of QSO SDSSJ135726.27+043541.4. Figure A30 displays the ion profiles from our new HIRES observations for this LLS, showing unambiguous detections of aligned Mg II and Fe II in both the weak and strong transitions of each ion. Thus this absorber is not "pristine," even though there are no metal-line detection in the COS spectrum. We measure the column densities using the AODM for each transition (see § 3.4), giving a consistent result between the weak and strong transitions. Averaging out the results, we find $\log N(\mathrm{Mg\,II}) = 11.84 \pm 0.04$ and $\log N(\mathrm{Fe\,II}) = 12.26 \pm 0.07$.
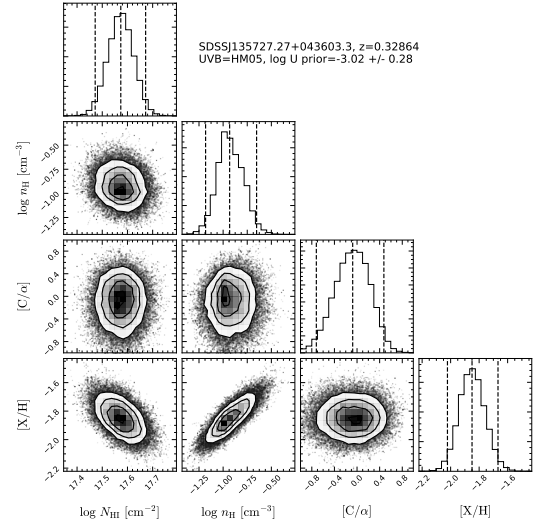
We have reanalyzed the metallicity of this system using the new information from our HIRES observations with the CCC results (upper limits on metal-ion column densities and a measurement of $\log N(\mathrm{H\,I})$, Wotta et al. 2019). With only Mg II, Fe II, and hydrogen detected, we need to apply a Gaussian prior on the $\log U$ distribution. We allow, however, the $[\mathrm{C}/\alpha]$ ratio to vary. We first consider the modeling with Fe II. The corner plot is shown in Figure A31, and the comparison between the observed and modeled detected metal column densities is shown in the left panel of Figure A32. The model results show the range of column densities encompassed by models representing the 16% and 84% confidence values in $\log U$. Fe II is underproduced, which is not surprising since without any ionization modeling, the column densities of Fe II and Mg II imply a super-solar value $[\mathrm{Fe\,II/Mg\,II}] = +0.50 \pm 0.08$. In this case the median metallicity value is $[\mathrm{X/H}] = -1.85$. We also ran a model without Fe II, and in this case the median metallicity value is $[\mathrm{X/H}] = -2.58$ (see Figure A33). In the right panel of Figure A32, we show the predicted value of Fe II from this model, and the discrepancy is even larger.

Given the large Fe enhancement relative to α elements in this system, it is unclear how to treat the metallicity of this absorber. Our clear detection of iron makes it unlikely this absorber has a metallicity $< 1\%$ of the
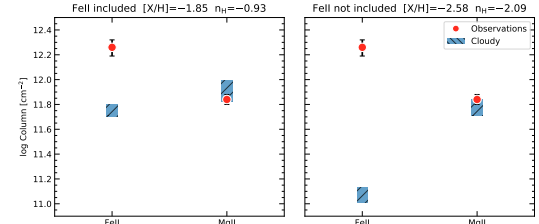
Figure A30. Ion profiles for absorption associated with LRG SDSSJ135727.27+043603.3 from the C18 sample at an impact parameter of $\rho = 130$ kpc. The profiles are shown in the reference frame of the LRG, and the red shading shows the section of the spectrum integrated to determine the ion column density.

Figure A31. Corner plot of the MCMC PDFs for the LLS associated with LRG SDSSJ135727.27+043603.3. The PDFs for each variable are plotted along the diagonal, and the other panels are the 2D distributions of the final MCMC walkers chains. The vertical dashed lines show the median value of the distribution and the bounds of the 95% confidence interval. Fe II is included in this run.
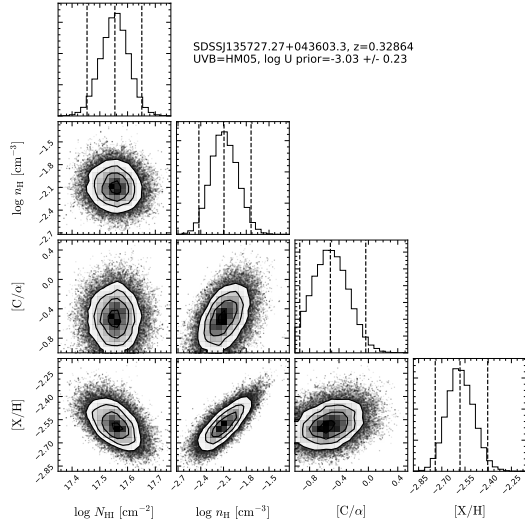
solar metallicity. However, we are wary about assuming the ionization balance of Fe is well-described: given the extensive network of energy levels for Fe^+ and Fe^{+2} below their ionization energies, the unaccounted-for autoionizing levels may play an important role in its behavior (Ferland et al. 2017). Because no other metal ions are detected, the models using Mg II or Mg II+Fe II are the best constraints. They give different results, and neither reproduces the observed Fe II column densities. Thus, we report the metallicity of this system using only the range bracketed by these two results, $[X/H] = [-2.58, -1.85]$. This absorber has a low metallicity (i.e., $[X/H] < -1$). However, given the detection of Mg II and Fe II, it is not "pristine."

Figure A32. Plot of observed Fe II and Mg II column densities compared to the column density ranges expected from Cloudy models. The median metallicity and 68% confidence interval of the log U distribution from the MCMC runs were used to create these models.

Figure A33. Same as in Fig. A31, but Fe II is not included in this run.